Reflections on switchable mirror devices

Bespiegelingen op geïntegreerde schakelbare spiegels

Annemarie van Geest-Lokhorst

Cover: The reflection of the bird in the water symbolizes the blurred observation, obtained during measurements, from which the original system has to be reconstructed.

Omslag: De weerspiegeling van de vogel in het water symboliseert de vervormde waarneming, die verkregen wordt tijdens metingen en waarvan het oorspronkelijke systeem gereconstrueerd dient te worden.

This work is part of the research programme of the 'Stichting voor Fundamenteel Onderzoek der Materie (FOM)', which is financially supported by the 'Nederlandse Organisatie voor Wetenschappelijk Onderzoek (NWO)'. The work was carried out at:

Vrije Universiteit
Faculty of Sciences
Condensed Matter Physics
De Boelelaan 1081
1081 HV Amsterdam
The Netherlands

ISBN-10: 90-9020701-5
ISBN-13: 978-90-9020701-8

VRIJE UNIVERSITEIT

Reflections on Switchable Mirror Devices

ACADEMISCH PROEFSCHRIFT

ter verkrijging van de graad Doctor aan
de Vrije Universiteit Amsterdam,
op gezag van de rector magnificus
prof.dr. T. Sminia,
in het openbaar te verdedigen
ten overstaan van de promotiecommissie
van de faculteit der Exacte Wetenschappen
op woensdag 14 juni 2006 om 13.45 uur
in het auditorium van de universiteit,
De Boelelaan 1105

door

Annemarie Christine van Geest-Lokhorst

geboren te Amersfoort

promotor: prof.dr. R.P. Griessen
copromotor: dr. B. Dam

Contents

1 Introduction **1**
1.1 Introduction . . . 2
1.2 Chromogenic devices . . . 4
1.3 Switchable mirrors as chromogenic devices . . . 6
1.4 Optical requirements of switchable devices . . . 8
1.5 Non-optical requirements of switchable devices . . . 11
1.6 This thesis . . . 12

2 RE-hydrides prepared by Pulsed Laser Deposition **19**
2.1 Introduction . . . 20
2.2 Experimental . . . 21
2.3 Results and discussion . . . 22
2.3.1 The deposition process . . . 22
2.3.2 Diffusion assisted preferential hydrogen ablation . . . 26
2.3.3 Morphological and structural properties . . . 27
2.3.4 Optical switching properties . . . 29
2.3.5 Oxygen-free films . . . 31
2.4 Conclusions . . . 35

3 Mg-TM-hydrides **39**
3.1 Introduction . . . 40
3.2 Experimental . . . 43
3.2.1 Preparation and characterization . . . 43
3.2.2 Modelling . . . 44
3.3 Present status of Mg_yNiH_x . . . 45
3.4 Results . . . 50
3.4.1 Optical properties of as-prepared films . . . 51
3.4.2 Optical properties of hydrogenated films . . . 54
3.4.3 Optical properties as a function of hydrogen concentration . . . 58
3.4.4 Structure . . . 68
3.5 Discussion . . . 71
3.6 Conclusions . . . 74

4 Thermochromic devices **81**
4.1 Introduction 82
4.2 Thermodynamic model 86
4.2.1 Gas cell device 86
4.2.2 All-solid-state device 91
4.3 Results 100
4.3.1 Mg-Ni gas cell device 100
4.3.2 Mg_2Ni/Pd all-solid-state device 104
4.3.3 Other devices 107
4.4 Discussion 108
4.4.1 The accuracy of the model and thermodynamic data 108
4.4.2 Hysteresis 110
4.4.3 Cycling stability 110
4.4.4 Kinetics 112
4.5 Conclusions 114

Summary **119**

Samenvatting **125**

List of publications **131**

Curriculum Vitae **133**

Dankwoord **135**

Chapter 1

Introduction

Metal-hydride switchable mirrors are able to change their optical appearance reversibly and thus belong to the class of chromogenic materials. The change in transmission, reflection and absorption can be induced in many different ways. This opens up the possibility of implementation of these switchable thin films in devices usable for a wide range of applications, including smart windows and variable emittance surfaces for temperature stabilization. In this thesis we discuss both the optical as well as the structural properties of various types of switchable mirrors in relation to their implementation in a device. The emphasis is on a gas cell and a novel all-solid-state thermochromic device.

1.1 Introduction

In 1995, Huiberts *et al.* [1, 2] discovered that yttrium and lanthanum hydride show spectacular reversible optical changes when loaded from the dihydride to the trihydride phase. These optical changes had so far been overlooked, since the hydrogen absorption by bulk samples causes disintegration into powder and thin film samples are extremely reactive with oxygen. However, Huiberts *et al.* prepared thin films of yttrium by evaporation under UHV conditions. Before exposure to air they are covered by a thin layer of Pd to prevent the yttrium from oxidation and at the same time to catalyze the hydrogen absorption.

As-deposited yttrium films have an hcp structure and a reflecting appearance (see Figure 1.1a). Upon hydrogen absorption the film transforms into the metallic fcc YH_2 phase, which has a weak transmission window in the red ($1.6 < \hbar\omega < 1.8$ eV). Due to the large negative heat of formation ($\Delta H = -114$ kJ/mol H [3]), this reaction is not reversible at room temperature. Further hydrogenation results in the yellow-transparent hcp YH_3 phase (absorption edge 2.6 eV). The latter transition is reversible at room temperature ($\Delta H = -41.8$ kJ/mol H [4]), which opens up the possibility for many applications, especially if it is prepared in the form of an all-solid-state device.

The rare-earth (RE) based, first generation switchable mirrors were followed by Mg-alloyed rare-earth hydrides [5] (see Figure 1.1b). Mg was chosen as the alloying metal, since the Mg hydride has a comparable heat of formation (-33 kJ/mol H [6]) and its band gap is large enough to be fully transparent in the visible range. These films appeared to be indeed color neutral. Moreover, these second generation switchable mirrors exhibit an absorbing, black state at intermediate hydrogen concentrations, due to the coexistence of nanocrystalline reflecting and transparent phases [7].

Richardson *et al.* [8] discovered that also Mg-Ni alloys display a change in optical appearance upon hydrogen absorption (see Figure 1.1c). These switchable mirrors are more resistant against oxidation than the former generations containing the highly reactive rare-earth metals. Again a black state is observed at intermediate hydrogen concentrations, albeit due to a completely different mechanism. The absorbing nature of the Mg_yNiH_x is essentially the result of an interference effect due to a self-organized double-layering [9, 10].

In this introduction chapter we first describe chromogenic devices, the different types and their applications. Subsequently, we briefly discuss the metal hydrides as chromogenic materials and the possibilities to implement them into switchable mirror device configurations. Then, we shortly review the optical as well as the structural requirements for the proper functioning of such devices. Finally, we give an outline of this thesis.

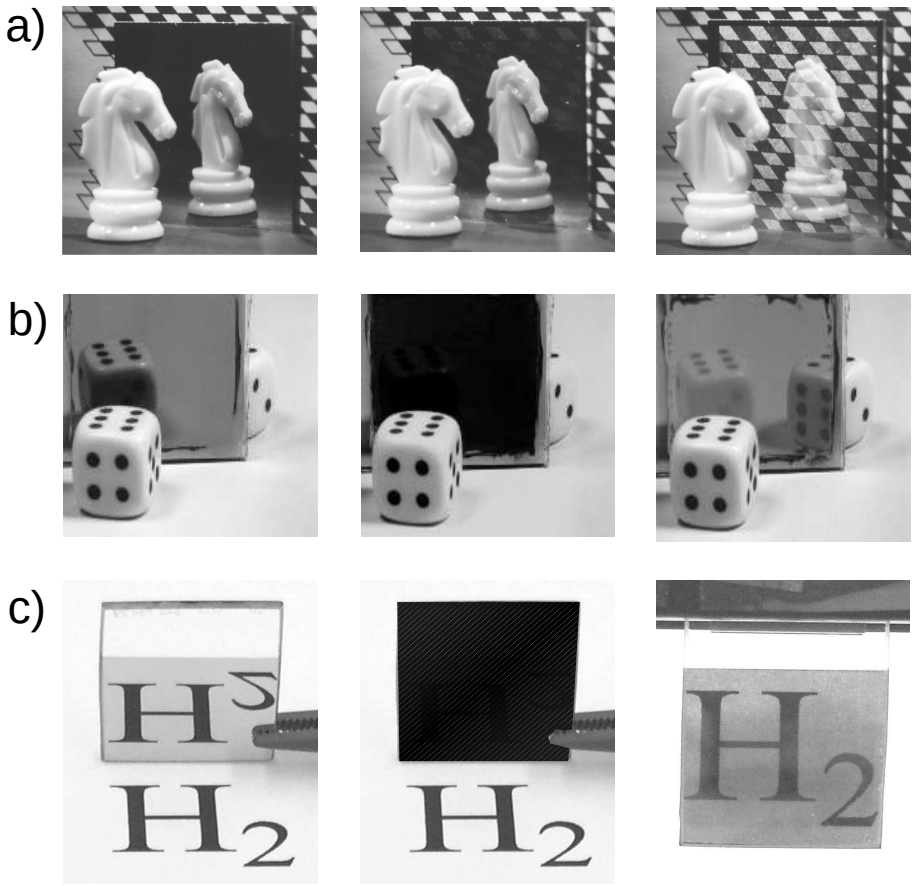

Figure 1.1: a) The left picture represents the as-deposited reflecting yttrium film (first generation) [2]. Upon hydrogen absorption, the film is transformed into the metallic fcc YH_2 phase, which has a weak transmission window in the red as shown in the middle picture. Further hydrogenation results in the yellow-transparent hcp YH_3 phase at the right side. The latter transition is reversible at room temperature. b) The metallic (left), absorbing (middle) and transparent state (right) of RE-Mg hydride films (second generation). These films are color neutral. c) RE-free Mg-transition metal-hydride films in the reflecting (left) and transparent (right) state (third generation) [11]. A schematic presentation of the absorbing state is added in the middle.

1.2 Chromogenic devices

Chromogenic materials exhibit actively controllable optical properties. Different ways of establishing a reversible change in the optical appearance have been found [12]. Applying a voltage across an electrochromic material is the most common way to impose an optical change, which can be implemented in an externally controllable switching device [13, 14]. Photochromism, in which a change in absorption is produced by exposure to light of an appropriate wavelength, is often found in living organisms. Examples are visual systems, photosynthesis and phototropism in plants, i.e. a light induced growth response directed towards or away from the light [15, 16]. Synthetic photochromics are often organic compounds, however some alkali metal halides and metal oxides display photochromic behavior as well. Gasochromic devices change optically when exposed to a certain gas. Upon removal or introduction of a different gas, this change is reversed [17–19]. Other chromogenic materials display temperature dependent optical properties, the so-called thermochromic materials. Gradual variation of the optical appearance upon changing temperature is observed especially at the coexistence of two forms of a molecule or due to changes in the absorption band width, while abrupt changes at a certain temperature are most often due to a phase transition [20, 21]. Chemically induced optical changes are referred to as chemochromism [22, 23], while piezochromism describes color changes resulting from an applied pressure [24].

Chromogenic materials have attracted attention for numerous years because of the variety of applicational possibilities. Already in 1815, for example, a color change in tungsten trioxide due to hydrogen introduction was reported [25, 26]. Application driven research is mainly based on the following device implementations [13, 27–29]:

a) Smart windows: One of the important applications of chromogenic devices is the smart window [30–32], the term being introduced in 1984 by Svensson *et al.* [33, 34] to reflect the use of chromogenic devices as window coatings. Smart windows provide for the need to obtain a comfortable indoor climate in an energy efficient way. Optimization of the climate within offices and homes is a hot topic in times of energy consumption awareness. In the US about 30% of the primary energy consumption is used for temperature control and illumination of residential and office buildings [35]. Reducing the energy demands is important in view of a coming decrease in the amount of easy-to-mine oil, i.e. the rising fossil fuel prices, because of environmental issues, and large regional bound fuel supplies. Ideally, smart windows are capable of regulating the solar input and controlling the heat release, while the outward visibility is maintained [36]. Electrochromic windows are already implemented in the sunroofs of some Ferrari cars. The driver can change the luminosity and filtering level of exterior heat of these windows.

b) Variable emittance surfaces: Another application of chromogenic devices is that of variable emittance surfaces for temperature stabilization. These can be integrated in for example spacecraft and solar collectors. The temperature of low earth orbit satellites increases due to direct radiation of the sun, solar radiation reflected by the earth and thermal radiation from the earth [37]. Conventionally, this heat

input is balanced by the cooling of the satellite through venetian blind radiators, which consists of reflecting vanes covering an emissive base plate. Vanes actuated by bimetallic springs open and close automatically upon a temperature change [37–39]. Already in 1959 [40] it has been suggested to coat space satellites with paint whose color is temperature dependent. Chromogenic coatings could indeed reduce the weight, lower the costs and prevent the use of moving parts. Such variable emittance surfaces for temperature control can be integrated in solar collectors as well. Heat management is required both in solar thermal collectors as well as hybrid solar collectors, which consist of a photovoltaic cell for the generation of electricity combined with a solar thermal collector to obtain hot water. A variable emittance surface can protect the photovoltaic cell against degradation by preventing them from overheating during a pump breakdown and it allows for the use of cheap materials, such as plastic, in the solar collectors assembly. In the case of the hybrid solar collector, the variable emittance coating should be added on top of the photovoltaic cell instead of underneath, to prevent absorption by the photovoltaic cell at high temperatures of both direct radiation and radiation reflected by the variable emittance coating [41].

c) Information displays: Since the discovery of electrochromic materials information displays have been considered as a possible application. However, liquid crystal based displays were more successful [28, 42]. The chromogenic displays consist of an electrochromic film in front of a diffusely scattering pigmented surface [13]. They exhibit a high contrast with no visual dependence on the viewing angle [14] and can be used for large area information displays in for example airport and railway stations or traffic direction boards [29]. Combining different colored chromogenics (e.g. cyan, magenta and yellow) on top of each other and arranging them in a matrix configuration allows for the possibility of multicolor displays. Electrochromic paper, on which an image can be created by touching it with a stylus electrode, has been prepared by incorporating electrochromes in paper [42, 43]. Printing of chromogenics on plastics results into flat, flexible displays [44–46], which can for example be used for dynamic pricing in stores.

d) Rear-view mirrors: Rear-view mirrors in cars and trucks based on chromogenics with variable reflectance do not longer belong to the possible applications, but are now being widely commercially available by both Gentex Corporation Corporation [47]. The reflectance is automatically regulated by the incident light level to prevent dazzling of the driver during night times. The commercially available mirrors are based on a stack of inorganic $H_yWO_x/Ta_2O_5/NiO_x$ [31].

e) Other applications: Other applications one could think of is the labeling of frozen food, which indicate whether an item has been exposed to conditions that cause deterioration [14]. The coloration of the label is dependent on both the time passed and the exposed temperature, thereby indicating the freshness of the food. Additionally, television screens can be turned into mirrors, when not in use. Furthermore, visors of helmets can be colored at day times and bleached during the night or when entering tunnels [48] or even medical contact lenses could be covered with chromogenic material to take over the natural iris function in the case of damage.

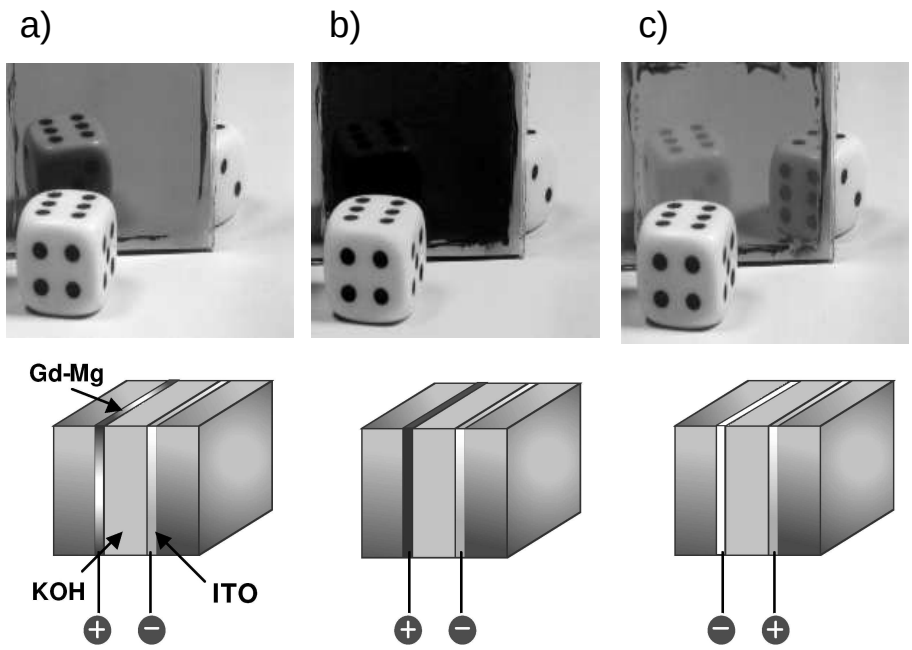

Figure 1.2: Schematic presentation of the lay-out of an electrochromic device together with its three optical states. The device consists of a liquid electrolyte, 1 M KOH solution in water, sandwiched between a Gd-Mg switchable layer and an ITO electrode. a) Metallic at positive voltage (2 V) b) Absorbing at 1 V and c) Transparent at negative voltage (-2 V) [49].

Moreover, electrochromic paper has been suggested for entry-ticket security [29, 42].

1.3 Switchable mirrors as chromogenic devices

This thesis deals with the use of Pd-covered metal hydrides, known as switchable mirrors (see Section 1.1), in chromogenic devices. These switchable mirrors change their optical properties upon the absorption of hydrogen [2] and thus belong to the gasochromic materials. Soon after their discovery, electrochemically switching was proven to be possible for both rare-earth [50] and rare-earth free switchable mirrors [51]. Chemochromic switching of lanthanide hydride to the transparent state can be accomplished by putting the thin film in a $NaBH_4$ solution and reversal is possible with an aqueous H_2O_2 solution [23]. Piezochromism has been observed for YH_3; the sample shifts from yellowish transparent to the red and finally disappears completely from the visible spectrum upon increasing the applied hydrogen pressure from 6 to 25 GPa [52]. Hoekstra *et al.* [53] demonstrated photochromism of rare earth hydride

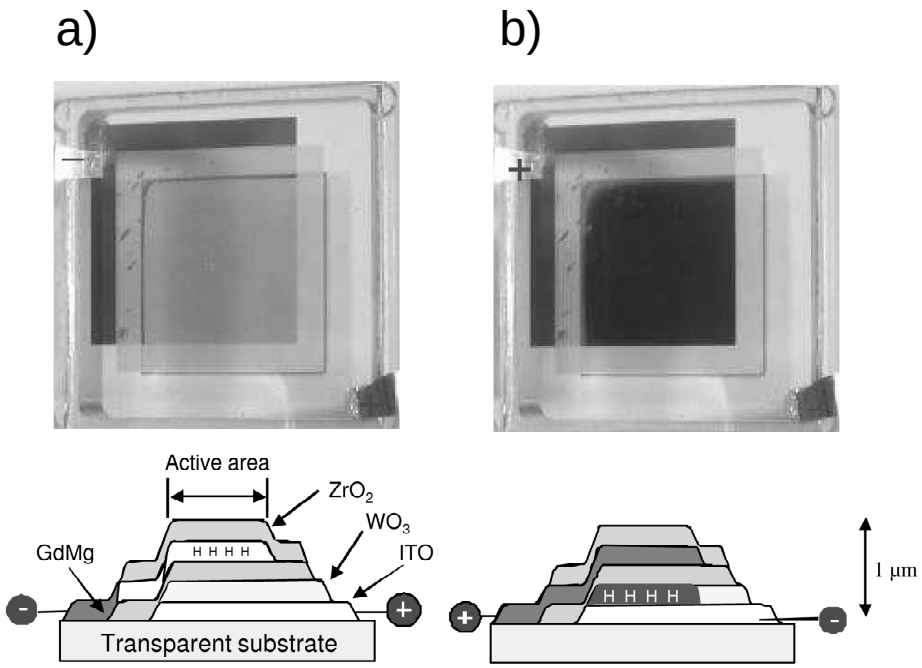

Figure 1.3: Schematic cross-sections of the lay-out of an all-solid-state device together with two optical states. The device consists of a solid-state hydrated zirconium oxide electrolyte. a) Both the Gd-Mg switchable layers and the WO_3 reservoir layer are in the transparent state and b) The Gd-Mg is in its metallic and the WO_3 in its dark blue state [55].

films. Additionally, thermochromic behavior was proven in Mg-Y switchable mirrors [54]. The optical switching upon a temperature change was established by exposing the sample to a hydrogen atmosphere. Increasing the temperature changes the equilibrium hydrogen concentration in the sample which thereby changes the optical appearance.

These different ways of optical changes open up many possibilities for device implementations. Gasochromic devices can be envisaged consisting of a Pd-capped metal-hydride layer deposited on a transparent substrate which is placed in a gaseous ambient. The switchable mirror becomes transparent or reflecting upon exposure to hydrogen or humid air, respectively.

Thermochromic devices [54] are basically switchable mirrors which are in equilibrium with a fixed amount of hydrogen. Increasing the temperature, results in a decrease of the hydrogen concentration in the switchable-mirror layer. Consequently, the optical properties change. Both $YH_{3-\delta}$ and $Mg_{0.1}Y_{0.9}H_{2.9-\delta}$ layers have been used in such an open gas cell device.

Electrochromic devices are more complicated. An electrolyte is sandwiched be-

tween the metal hydride and a counter electrode. The lay-out is depicted in Figure 1.2 in which the hydrogen is transported from the electrolyte to the metal hydride by using it as a negative electrode. Solutions of 1 or 2 M KOH [49, 56–58] in water have been used as electrolytes and the applied voltage is typically a few volts. Delamination and the formation of an oxide layer at the metal-hydride electrolyte interface reduced the cycling durability [56]. Furthermore, liquid electrolytes are inconvenient and might leak; therefore, all-solid-state devices have been investigated. The first all-solid-state switchable mirror device [59] had a bottom-electrode made of Gd-Mg hydride and a top-electrode of tungsten oxide. Using an inverted device [55] with a lay-out shown in Figure 1.3 the switching time could be reduced from 16 hours to 5 minutes. In both cases, hydrated zirconium oxide was used as the solid-state electrolyte.

1.4 Optical requirements of switchable devices

The type of application determines the wavelength region in which the optical change has to take place. Within this region, the optical contrast between metallic and hydride state or the intermediate black state, should be optimized. This can be done by choosing the right switchable-mirror layer material, a suitable composition (see Chapter 3) and the optimal thickness [60]. The optical properties of the other layers of the device are equally important, but will not be discussed in this thesis. We focus on the demands of the active switching layer for applications discussed in section 1.2.

Let us first discuss the smart window. Ideally, they are capable of regulating the solar input and controlling the heat dissipation, while the outward visibility is maintained [36]. To this end, the smart window should have a variable reflection in the solar spectrum range (from 0.4 to 5 eV or from 3 to 0.25 μm). The reflection should be high in summer and low in winter (see Figure 1.4). Furthermore, the emissivity for thermal radiation ($\hbar\omega < 0.6$ eV or $\lambda > 2$ μm) should be high during hot and low during cold weather. Both effects would reduce the demand for air conditioning and central heating, respectively. A high transparency in the visible region is desirable to preserve the visual contact to the surroundings, i.e. $T > 0.8$ between approximately 1.8 and 3.1 eV or 0.7 to 0.4 μm (see Figure 1.5). An example of a static window with low thermal losses is doped SnO_2 on glass with a transmittance in the solar region of around 80% and a reflectance in the thermal region of ≈90% [36, 61]. Metal-hydride switchable mirrors can be used as smart windows in cars, to reduce the thermal load while parked [62], since they reflect the entire solar when in the metallic state. Mg-based switchable mirrors are best suited, since they are color neutral in the transparent state.

The optical properties of a switching layer for variable emittance surfaces should be temperature dependent. This could either be done actively by using a thermochromic layer or by using an electrochromic layer in combination with a temperature sensor. For example the thermochromic device used for a solar thermal

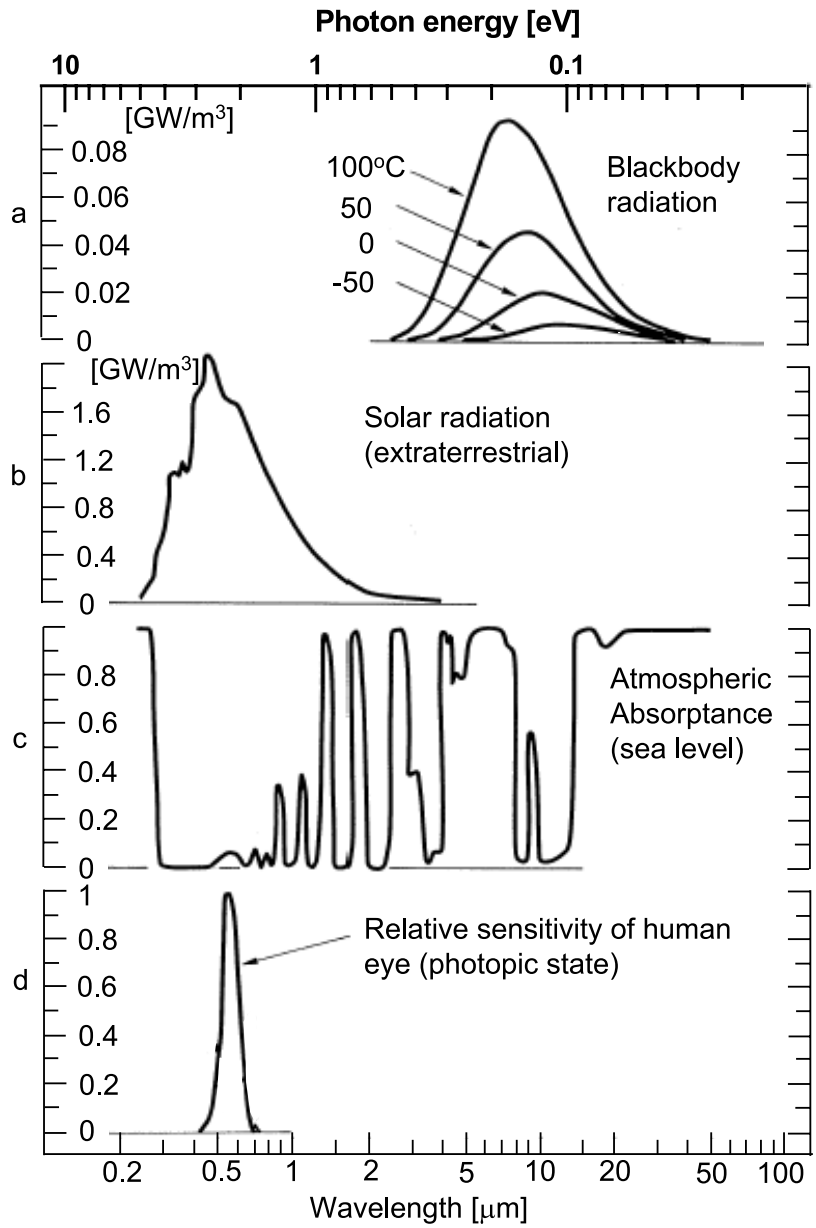

Figure 1.4: Spectra which indicate the wavelength of interest for: (a) blackbody radiation at four temperatures; (b) solar radiation outside the earths atmosphere; (c) typical absorptance vertically across the full atmospheric envelope; (d) relative sensitivity of the human eye. From Granqvist [36].

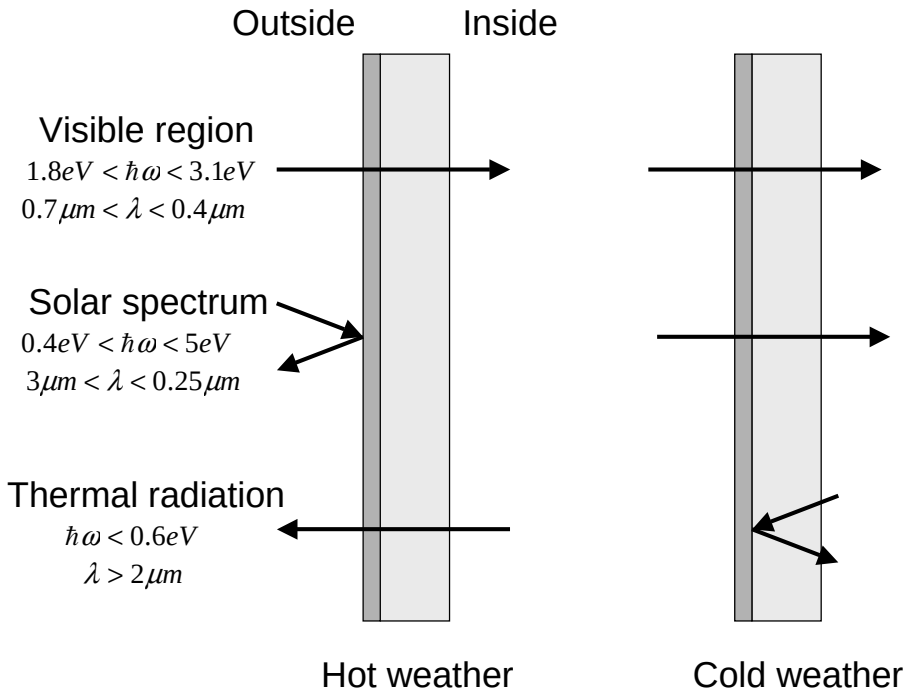

Figure 1.5: Desirable optical properties at various wavelength during hot and cold weather. To maintain outward visibility, the smart window has to be transparent in the visible region at all times. Solar radiation should be reflected during hot weather and let through during cold days. For thermal radiation it is the other way around.

collector will need in the solar spectrum range (0.4 to 5 eV or 3 to 0.25 μm) a low reflection at low temperature in order to absorb the solar radiation to heat the water. At high temperatures a high reflection in the solar region is necessary to prevent overheating of the collector (see Figure 1.6). Furthermore, it will need low emissivity of thermal radiation ($\hbar\omega < 0.6$ eV or $\lambda > 2$ μm) at low temperatures to prevent cooling down the water and high emissivity at high temperatures to prevent overheating. Metal-hydride switchable mirrors suit nicely for this application. For example, Mg-Ni reflects 60% of the solar spectrum in its metallic state, while it absorbs 84% after only a small amount of hydrogen absorption. The film emits only 16% of the 100°C black-body radiation [60].

Chromogenic materials for information displays, should switch between a high and low transparent state in the visible wavelength region. By placing these materials in front of a diffusively scattering pigmented surface, a high contrast can be established. The optical appearance should not depend on the viewing angle. Furthermore, they should be readable in all weather conditions including direct sunlight.

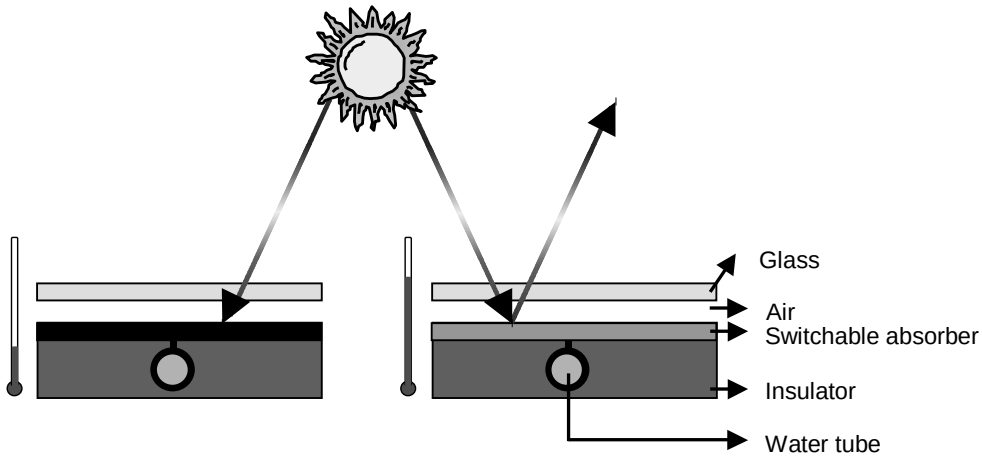

Figure 1.6: Schematic presentation of a solar thermal collector. At low water temperatures (left side), the solar radiation is absorbed to heat the cold water. When the water becomes hot (right side), the switchable absorber now becomes reflecting for the solar radiation and prevents further heating [41].

Epitaxial rare-earth switchable mirrors form a micrometer-sized triangular network during initial hydrogen loading. These individual domains can switch independently, which make them suitable for the use in all-solid-state displays [63].

1.5 Non-optical requirements of switchable devices

In order to obtain a good active switching layer for an all-solid-state switchable device several non-optical properties of this layer need to be addressed. These include fast switching times, a high coloration efficiency, no history dependent optical properties and a good cycling stability. Specific applications need particular demands, like durability against radiation and solar wind in space for space applications [40], but these peculiarities will not be dealt with here.

Devices should have fast kinetics for short switching times. For the applications described above, the reaction time should be in the order of minutes. This means that the active switchable layer requires a maximum switching time of several minutes to be applicable in such devices. Hydrogen diffusion in metals is fast. Indeed the switching time of a metal-hydride switchable layer in a gasochromic set-up can be reduced to 40 ms for Gadolinium-Magnesium films [49]. However, implemented into a device, the switching time increases to several minutes [55], which is still appropriate.

Essential is also the amount of charge needed for switching, which is expressed

by the coloration efficiency ($CE(\lambda)$):

$$CE(\lambda) = \frac{\Delta OD(\lambda)}{q} \tag{1.1}$$

in which $\Delta OD(\lambda)$ is the optical density at a certain wavelength λ and q represents the transferred charge per unit area. For $Sm_{0.3}Mg_{0.7}H_x$ the coloration efficiency was found to be $CE = -37$ cm^{2}C^{-1} for the visible part of the optical spectrum [57]. Theoretically, the charge needed to increase the transmission of Mg_2NiH_x by four orders of magnitude is ≈ 40 mC/cm^2, giving a coloration efficiency of $CE = 100$ cm^{2}C^{-1}, which is much larger than the value of $CE(631\ nm) = 50-55$ cm^{2}C^{-1} found for tungsten oxide [13].

Furthermore, a property that will be needed for all kinds of all-solid-state devices is the absence history dependent optical properties. This allows for a sensitive reaction of the device to the applied changing environment and implies that the active switching layer does not show hysteresis. In $La_{1-z}Y_zH_x$ switchable films, hysteresis is absent for $z \leq 0.67$ [64].

Finally, the cycling stability of the device is important. Both the optical contrast as well as the reaction time should not decay with increasing switching cycle. For example, for smart window devices it is essential to have a lifetime of at least 10 years, which implies several tenth of thousand switching cycles. Large expansion of the active layer, induces stress to adjacent layers, which reduces the lifetime and need therefore to be minimized. Degradation can also be induced by interaction between adjoining layers, such as interface mixing. For RE-metal-hydride switchable films, the intermixing between Pd and RE can be avoided by using a thin oxide buffer layer [65].

1.6 This thesis

As discussed in the preceding part, a variety of exciting applications exist for chromogenic materials. Metal-hydride switchable mirrors have unique properties and are therefore promising for specific applications, e.g. as switchable absorbers for thermal solar collectors or as smart windows. Although elaborate research on switchable mirrors has been performed, only few are dedicated to the implementation of such layers into devices. This thesis investigates those properties necessary for the incorporation into such devices. Since the applications of switchable absorbers require a transition in optical properties upon a temperature change, we focus our investigations on the implementation into two types of thermochromic devices, i.e. an open gas cell and an all-solid-state device. For that purpose a number of switchable mirror layers need to be fabricated and tested on the required properties. The following steps are selected to create these samples.

First, we use pulsed laser deposition (PLD) for creating rare-earth (RE) switchable mirrors (Chapter 2). These RE-metal hydrides are the archetypal switchable mirrors. They exhibit a high optical contrast. We use PLD as the deposition technique is a versatile method. The optical change is between the reflecting dihydride

and the transparent trihydride phase. In depositing the dihydride in-situ, we avoid the large expansion which accompanies the phase transition from metallic to the dihydride state, thereby increasing the cycling stability. X-ray diffraction is used to monitor the hydrogenation process. The optical properties are compared with molecular beam epitaxy (MBE)-grown films. Useful devices can only be created when sufficient knowledge about the surface flatness has been obtained. Therefore the surface morphology is analyzed with AFM.

Furthermore, sputtered third generation magnesium-transition metal (Mg-TM with TM=Co,Fe) films are investigated both optically and structurally to test their suitability for incorporation in a thermochromic device (Chapter 3). These switchable mirrors are superior in that they are color neutral, which is essential for many applications. Just as important is the fact that they are more resistant against oxidation than metal hydrides containing the highly reactive rare-earth hydrides and therefore considered to have an improved cycling stability. Mg-TM with TM=Ni films are known to exhibit a third, absorbing state at intermediate hydrogen concentration, which enables switching between reflection and absorption. That opens up the opportunities for temperature control. We investigate the other Mg-TM (TM=Co, Fe) at different Mg-TM ratios to see whether any of these exhibit an absorbing state as well. The experiments need to be accompanied by a theoretical explanation, which relates the structural properties and the optical behavior to find the optimal conditions of these layers for the implementation into devices.

The research cannot be complete without a discussion of the thermodynamics of a gas cell and all-solid-state thermochromic device (Chapter 4). The gas cell device consists of a switchable mirror layer in contact with a hydrogen atmosphere. The all-solid-state device consists of a switchable mirror and a reservoir layer, which absorbs or desorbs the hydrogen from the optically active layer. From the thermodynamical theory we derive a simple model with which we can estimate the initial hydrogen pressure and the properties of the reservoir layer in the all-solid-state device. The outcome is the basis for creating such devices.

Bibliography

[1] J. N. Huiberts. *On the road to dirty metallic atomic hydrogen.* PhD thesis, Vrije Universiteit, Amsterdam, 1995.

[2] J.N. Huiberts, R. Griessen, J.H. Rector, R.J. Wijngaarden, J.P. Dekker, D.G. de Groot, and N.J. Koeman. Yttrium and lanthanum hydride films with switchable optical properties. *Nature*, 380:231–234, 1996.

[3] Howard E. Flotow, Darrell W. Osborne, Klaus Otto, and Bernard M. Abraham. YH_3 and YD_3: Heat capacities and thermodynamic functions from 15° to 350°K and infrared absorption spectra. *J. Chem. Phys.*, 38:2620–2626, 1963.

[4] L.N. Yannopoulos, R.K. Edwards, and P.G. Wahlbeck. The thermodynamics of the yttrium-hydrogen system. *J. Phys. Chem.*, 69(8):2510–2515, August 1965.

[5] P. van der Sluis, M. Ouwerkerk, and P.A. Duine. Optical switches based on magnesium lanthanide alloy hydrides. *Appl. Phys. Lett.*, 70(25):3356–3358, 1997.

[6] F. H. Ellinger, C. E. Holley, B. B. McInteer, D. Pavone, R. M. Potter, E. Staritzky, and W. H. Zachariasen. The preparation and some properties of magnesium hydride. *J. Amer. Chem. Soc.*, 77:2647–2648, 1955.

[7] I.A.M.E. Giebels, J. Isidorsson, and R. Griessen. Highly absorbing black Mg and rare-earth-Mg switchable mirrors. *Phys. Rev. B*, 69:205111, 2004.

[8] T.J. Richardson, J.L. Slack, R.D. Armitage, R. Kostecki, B. Farangis, and M.D. Rubin. Switchable mirrors based on nickel-magnesium films. *Appl. Phys. Lett.*, 78(20):3047–3049, 2001.

[9] W. Lohstroh, R.J. Westerwaal, J.L.M. van Mechelen, C. Chacon, E. Johansson, B. Dam, and R. Griessen. The structural and optical properties of $Mg_{2\pm y}NiH_x$ switchable mirrors upon hydrogen loading. *Phys. Rev. B*, 70:165411, 2004.

[10] W. Lohstroh, R.J. Westerwaal, B. Noheda, S. Enache, I.A.M.E. Giebels, B. Dam, and R. Griessen. Self-organized layered hydrogenation in black Mg_2NiH_x switchable mirrors. *Phys. Rev. Lett.*, 93(19):197404, November 2004.

[11] T.J. Richardson, R.D. Armitage, J.L. Slack, and M.D. Rubin. Alternative materials for electrochromic mirror devices. poster presentation at the Fourth International Meeting on Electrochromism (IME-4), August 2000.

[12] Charles B. Greenberg. Optically switchable thin films: a review. *Thin Solid Films*, 251:81–93, 1994.

[13] C.G. Granqvist. *Handbook of inorganic electrochromic materials.* Elsevier, Amsterdam, 1995.

[14] Prakash R. Somani and S. Radhakrishnan. Electrochromic materials and devices: present and future. *Mater. Chem. Phys.*, 77:117–133, 2003.

[15] Henri Bouas-Laurent and Heinz Dürr. Organic photochromism. *Pure Appl. Chem.*, 73(4):639–665, 2001.

[16] G.H. Brown. *Photochromism*, volume 3 of *Techniques of chemistry.* Wiley-Interscience, New York, 1971.

[17] Andreas Georg, Wolfgang Graf, Dietmar Schwieger, Volker Wittwer, Peter Nitz, and Helen Rose Wilson. Switchable glazing with a large dynamic range in total solar energy transmittance (TSET). *Sol. Energy*, 62:215–228, 1998.

[18] V. Wittwer, M. Datz, J. Ell, A. Georg, W. Graf, and G. Walze. Gasochromic windows. *Sol. Energy Mater. Sol. Cells*, 84:305–314, 2004.

[19] Christian Salinga, Hansjörg Weis, and Matthias Wuttig. Gasochromic switching of tungsten oxide films: a correlation between film properties and coloration kinetics. *Thin Solid Films*, 414:275–282, 2002.

[20] K. Bange. Colouration of tungsten oxide films: A model for optically active coatings. *Sol. Energy Mater. Sol. Cells*, 58:1–131, 1999.

[21] Jesse H. Day. Thermochromism. *Chem. Rev.*, 63(1):65–80, 1963.

[22] B. Dischler and A. Räuber. Oxygen vacancy model for chemochromic effects in $LiNbO_3$ doped with Mn, Fe or Cu. *Solid State Commun.*, 17:953–956, 1975.

[23] P. van der Sluis. Chemochromic optical switches based on metal hydrides. *Electrochim. Acta*, 44:3063–3066, 1999.

[24] J.L. Kirk, K. Vedam, V. Narayanamurti, A. Jayaraman, and E. Bucher. Direct optical observation of the semiconductor-to-metal transition in SmS under pressure. *Phys. Rev. B*, 6(8):3023–3026, 1972.

[25] J.J. Berzelius. *Afhandlingar i Fysik, Kemi och Mineralogi*, 4:293–307, 1815.

[26] J.J. Berzelius. *J. Chem. Phys.*, 16:476, 1816.

[27] C.M. Lampert. Large-area smart glass and integrated photovoltaics. *Sol. Energy Mater. Sol. Cells*, 76:489–499, 2003.

[28] R. David Rauh. Electrochromic windows: an overview. *Electrochim. Acta*, 44:3165–3176, 1999.

[29] David R. Rosseinsky and Roger J. Mortimer. Electrochromic systems and the prospects for devices. *Adv. Mater.*, 13(11):783–793, 2001.

[30] Brian A. Gregg. Photoelectrochromic cells and their applications. *Endeavour*, 21(2):52–55, 1997.

[31] Carl M. Lampert. Chromogenic switchable glazing: Towards the development of the smart window. In *Proceedings of Window Innovations Conference*, page 348, Toronto, Canada, June 1995.

[32] C.G. Granqvist, A. Azens, A. Hjelm, L. Kullman, G.A. Niklasson, D. Rönnow, M. Strømme Mattsson, M. Veszelei, and G. Vaivars. Recent advances in electrochromics for smart windows applications. *Sol. Energy*, 63(4):199–216, 1998.

[33] Svensson and Granqvist. Electrochromic coatings for 'smart windows'. In *Proceedings of the society of photo optical instrumentation engineers*, volume 502, pages 30–37, 1984.

[34] J.S.E.M. Svensson and C.G. Granqvist. Electrochromic coatings for 'smart windows'. *Sol. Energy Mater.*, 12:391–402, 1985.

[35] R. Griessen, I.A.M.E. Giebels, and B. Dam. *Hydrogen the energy carrier of the future*, chapter Optical properties of metal-hydrides: switchable mirrors. Wiley-VCH, 2006.

[36] Claes G. Granqvist and Volker Wittwer. Materials for solar energy conversion: An overview. *Sol. Energy Mater. Sol. Cells*, 54:39–48, 1998.

[37] David G. Gilmore and Mel Bello. *Satellite thermal control handbook*. Aerospace Corporation Press, El Segundo, 1994.

[38] Jeffrey S. Hale, Michael DeVries, Brad Dworak, and John A. Woollam. Visible and infrared optical constants of electrochromic materials for emissivity modulation applicationss. *Thin Solid Films*, 313-314:205–209, 1998.

[39] Jeffrey S. Hale and John A. Woollam. Prospects for IR emissivity control using electrochromic structures. *Thin Solid Films*, 339:174–180, 1999.

[40] Prasanna Chandrasekhar, Brian J. Zay, Gaj C. Birur, Suraj Rawal, Edward A. Pierson, Lonny Kauder, and Theodore Swanson. Large, switchable electrochromism in the visible through far-infrared in conducting polymer devices. *Adv. Funct. Mater.*, 12(2):95–103, 2002.

[41] Theodoros G. Atmakidis. Applicibility of the VAREM on PVT and thermal solar collectors. Technical report, Technical University of Eindhoven, 2005.

[42] Paul M.S. Monk, Claire Turner, and Safina P. Akhtar. Electrochemical behaviour of methyl viologen in a matrix of paper. *Electrochim. Acta*, 44:4817–4826, 1999.

[43] Paul M.S. Monk, Frédéric Delage, and Sara Maria Costa Vieira. Electrochromic paper: utility of electrochromes incorporated in paper. *Electrochim. Acta*, 46:2195–2202, 2001.

[44] James P. Coleman, Anne T. Lynch, Puttanachetty Madhukar, and John H. Wagenknecht. Antimony-doped tin oxide powders: Electrochromic materials for printed displays. *Sol. Energy Mater. Sol. Cells*, 56:375–394, 1999.

[45] James P. Coleman, Anne T. Lynch, Puttanachetty Madhukar, and John H. Wagenknecht. Printed, flexible electrochromic displays using interdigitated electrodes. *Sol. Energy Mater. Sol. Cells*, 56:395–418, 1999.

[46] Jingyue Liu and James P. Coleman. Nanostructured metal oxides for printed electrochromic displays. *Mater. Sci. Eng., A*, 286:144–148, 2000.

[47] David Mecerreyes, Rebeca Marcilla, Estibalitz Ochoteco, Hans Grande, Jose A. Pomposoa, Ricardo Vergaz, and Jose M. Sánchez Pena. A simplified all-polymer flexible electrochromic device. *Electrochim. Acta*, 49:3555–3559, 2004.

[48] Claes G Granqvist. Smart windows and intelligent glass façades. *Smart Materials Bulletin*, October:9, 2002.

[49] Ronald Griessen and Paul van der Sluis. Schaltbare Spiegel, Elektronenkorrelationen in der Anwendung. *Physik in unserer Zeit*, 32(2):76–83, 2001.

[50] P.H.L. Notten, M. Kremers, and R. Griessen. Optical switching of Y-hydride thin film electrodes. *J. Electrochem. Soc.*, 143(10):3348–3353, October 1996.

[51] J. Isidorsson, I.A.M.E. Giebels, M. Di Vece, and R. Griessen. Electrochromism of Mg-Ni hydride switchable mirrors. In *Proc. SPIE*, volume 4458, pages 128–137, 2001.

[52] Rinke J. Wijngaarden, J.N. Huiberts, D. Nagengast, J.H. Rector, R. Griessen, M. Hanfland, and F. Zontone. Towards a metallic YH_3 phase at high pressure. *J. Alloys Compd.*, 308:44–48, 2000.

[53] A.F.Th. Hoekstra, A.S. Roy, T.F. Rosenbaum, R. Griessen, R.J. Wijngaarden, and N.J. Koeman. Light induced metal–insulator transition in a switchable mirror. *Phys. Rev. Lett.*, 86(23):5349–5352, 2001.

[54] I.A.M.E. Giebels, S.J. van der Molen, R. Griessen, and M. Di Vece. Thermochromic effect in $YH_{3-\delta}$ and $Mg_{0.1}Y_{0.9}H_{2.9-\delta}$. *Appl. Phys. Lett.*, 80(8):1343–1345, 2002.

[55] P. van der Sluis and V.M.M. Mercier. Solid state Gd-Mg electrochromic devices with ZrO_2H_x electrolyte. *Electrochim. Acta*, 46:2167–2171, 2001.

[56] Anna-Maria Janner, Paul van der Sluis, and Virginie Mercier. Cycling durability of switchable mirrors. *Electrochim. Acta*, 46:2173–2178, 2001.

[57] M. Ouwerkerk. Electrochemically induced optical switching of $Sm_{0.3}Mg_{0.7}H_x$ thin layers. *Solid State Ionics*, 113-115:431–437, 1998.

[58] P. Velásquez, R. Castañer, M. A. de la Casa-Lillo, M. M. Sánchez-López, R. Mallavia, I. Moreno, A. Gutiérrez, and F. Mateos. Surface and optical characterization of yttrium hydride films deposited on regular glass to be used as switchable mirrors. *Surf. Interface Anal.*, 34:311–315, 2002.

[59] R. Armitage, M. Rubin, T. Richardson, N. O'Brien, and Yong Chen. Solid-state gadolinium-magnesium hydride optical switch. *Appl. Phys. Lett.*, 75(13):1863–1865, 1999.

[60] J.L.M. van Mechelen, B. Noheda, W. Lohstroh, R.J. Westerwaal, J.H. Rector, B. Dam, and R. Griessen. Mg-Ni-H films as selective coatings: Tunable reflectance by layered hydrogenation. *Appl. Phys. Lett.*, 84:3651–3653, 2004.

[61] Carl M. Lampert. Heat mirror coatings for energy conserving windows. *Solar Energy Materials*, 6:1–41, 1981.

[62] Nebojsa I. Jaksic and Cem Salahifar. A feasibility study of electrochromic windows in vehicles. *Sol. Energy Mater. Sol. Cells*, 79:409–423, 2003.

[63] J.W.J. Kerssemakers, S. J. van der Molen, N.J. Koeman, R. Günther, and R. Griessen. Pixel switching of epitaxial Pd/YH_x/CaF_2 switchable mirrors. *Nature*, 406:489–491, 2000.

[64] A.T.M. van Gogh, D.G. Nagengast, E.S. Kooij, N.J. Koeman, and R. Griessen. Quenching of giant hysteresis effects in $La_{1-z}Y_zH_x$ switchable mirrors. *Phys. Rev. Lett.*, 85(10):2156–2159, 2000.

[65] S.J. van der Molen, J.W.J. Kerssemakers, J.H. Rector, N.J. Koeman, and B. Dam. Hydriding kinetics of Pd capped YH_x switchable mirrors. *J. Appl. Phys.*, 86(11):6107–19, December 1999.

Chapter 2

RE-hydrides prepared by Pulsed Laser Deposition

Epitaxial rare earth dihydride films (REH_2) on (111) CaF_2 are prepared by pulsed laser deposition (PLD) from a metallic yttrium target. Without adding any reactive hydrogen, the dihydride is formed in situ due to hydrogen evolving from the metallic target which contains ∼7 at% H. Upon pulsed laser irradiation, the target acts as a pulsed source of both RE and hydrogen. The increased hydrogen content of the film as compared to the target is due to diffusion assisted preferential ablation of hydrogen. Due to this deposition process the hydrogen load on the deposition system is minimized, which is important in view of the fabrication of hydride/oxide stacks for all-solid-state switchable mirror devices. Furthermore, the preparation of both nanocrystalline and epitaxial REH_2 films demonstrates the versatility of the PLD process. Comparing the switching behavior to that of MBE-grown, ex-situ hydrogenated RE films, PLD-grown RE films show a reduced optical and electrical contrast in switching, which is due to the additional formation of $RE(OH)_3$. Using a highly purified RE target the amount of oxygen is reduced, which improves the switching contrast. We found that for the in-situ PLD-grown nanocrystalline hydride films there is no hysteresis due to the absence of a phase transition. Moreover, these films have a smoother surface morphology. The latter effects make PLD an interesting technique for the implementation of switchable rare earth hydride films in all-solid-state devices.

2.1 Introduction

Smart windows will play an important role in reducing the energy consumption of buildings. Electrochromic materials such as WO_3 are already used in commercial energy saving windows [1]. Huiberts *et al.* [2] pointed out the relevance of Rare Earth (RE) hydrides for such applications. The advantage of RE-hydrides is that they are highly reflecting rather than dark blue as H_xWO_3 in their non-transparent state. By tuning the hydrogen concentration in $YH_{2+\delta}$ one controls the reflection. Upon hydrogenation the metallic face-centered cubic YH_2 β-phase transforms into the semiconducting hcp $YH_{3-\delta}$ γ-phase. The hydrogen concentration rather than the symmetry change is essential for the electronic transition [3, 4]. The reversible metal-insulator transition is of high technological importance, especially if it can be realized as an all-solid-state device. Such a device consists of two electrodes with a switching layer, a storage layer and an electrolyte.

The first demonstrator devices were prepared using sputtering to deposit the various (oxide and hydride) active layers [5, 6]. We alternatively explore the use of pulsed laser deposition (PLD) to manufacture switchable devices. The initial reason for choosing PLD as the deposition method is the simplicity and flexibility of the technique and the possibility of deposition at relatively high reactive pressure. The latter is important in view of the fabrication of hydride/oxide stacks for all-solid-state switchable mirror devices. We found that PLD has several important additional advantages. First of all, even when using metallic yttrium targets, we can deposit β-YH_2 films in situ without adding any hydrogen gas to the deposition system. Hydrogen dissolved in the metallic (α-phase) yttrium target provides for the necessary hydrogen. The background hydrogen pressure during this deposition process is only 10^{-7} mbar. Secondly, when keeping the substrate at room temperature, *nanocrystalline* dihydride films can be formed. Thus, using PLD, we can investigate the effect of the microstructure on the switching properties.

We compare the morphology and the optical and electrical switching properties of these films with MBE-deposited films. The latter films are deposited in the metallic hcp α-phase and loaded ex situ with hydrogen to form the fcc β- and hcp γ-phase. For an all-solid-state device, in-situ deposition of YH_2 is essential. To prevent shortcuts in the insulating electrolyte the surface should be flat. Moreover, in most applications, a hysteresis in the transition is to be avoided. We find that, although the PLD-films are promising in terms of surface flatness and hysteresis, the optical contrast on switching is severely reduced. This is due to the presence of oxygen in the film, coming from the with oxygen contaminated target. Since we have highly purified Gd-target available, this target is used in the PLD set-up. Now the optical contrast is increases, while the absence of hysteresis and the high flatness is preserved.

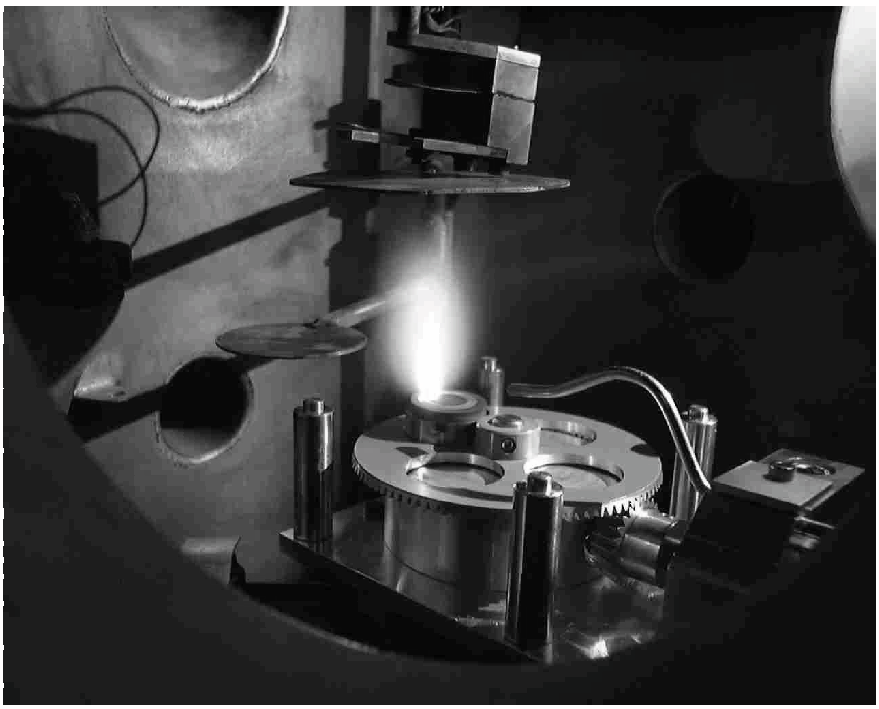

Figure 2.1: Picture of the pulsed laser deposition (PLD) set-up during ablation. Illumination of the target by the laser light, results locally in rapid heating. This causes removal of the target material in the form of a plasma. The target is rotated during ablation and the substrate is wobbled through the plume to get a uniform thickness.

2.2 Experimental

Thin REH_2 films are grown in high vacuum (base pressure $< 5 \cdot 10^{-8}$ mbar) by pulsed laser deposition (PLD). The Lambda Physik LPX 305i excimer laser with a pulse duration of 25 ns and a wavelength of 248 nm, is equipped with a beam homogenizer to obtain a spatially homogeneous spot. The beam is projected onto the target on an angle of 45°. Illumination of the target by the laser light, results locally in rapid heating due to absorption of the light. This causes removal of the target material in the form of a plasma forming a plume as can be seen in Figure 2.1. To hydrogenate the target, it is ablated in a few mbar H_2 during half an hour. After this treatment the target emits an increased amount of hydrogen upon laser ablation in vacuum. A fluence of 0.7 J cm^{-2} is used to minimize the formation of particulates: small metallic droplets originating from the target. During the deposition process the plume tilts towards the incoming laser beam. The tilting is a consequence of the repetitive illumination causing a change in the surface morphology of the target.

Hence, the target has to be polished before it is placed inside the vacuum chamber and it needs to be rotated during use. At a laser pulse repetition frequency of 5 Hz we obtain a deposition rate of about 0.1 nm s^{-1}. We monitor the deposition rate with a quartz crystal microbalance. In order to obtain a homogeneous layer thickness (100-300 nm), the substrate is wobbled through the plume. The distance between the target and the substrate is 3.5 cm. This is slightly larger than the size of the visible plume. Epitaxial films are deposited on CaF_2 at substrate temperatures (T_s) between 400°C and 600°C. Nanocrystalline films are grown on quartz substrates by depositing at room temperature. Epitaxial MBE grown Y films are deposited on CaF_2 at 700°C at a base pressure of $6{\cdot}10^{-9}$ mbar [7]. All films are covered with a 10 nm Pd cap layer by means of Pd-sublimation to prevent oxidation of the films and to catalyze hydrogen uptake.

X-ray diffraction measurements using Cu Kα radiation ($\lambda = 1.54$ nm) are performed on a Bruker D8 diffractometer. For residual gas analysis (RGA) we use a VSW quadrupole mass spectrometer. The surface morphology is investigated using a Nanoscope III tapping mode AFM. Simple hydrogenation experiments up to 100 mbar H_2 are performed in a separate vacuum chamber fitted with a LED-diode ($\lambda_0 = 635$ nm) and photodetector, while the resistivity is simultaneously recorded in a Van der Pauw geometry. More precise optical transmission and reflection spectra are recorded ex situ in a Bruker IFS 66/S spectrometer with a maximum pressure of 1 bar H_2.

2.3 Results and discussion

2.3.1 The deposition process

Pulsed laser deposition from a yttrium target typically leads to an increase in background pressure, especially when the target has been hydrogenated. From the residual gas analyzer (RGA), we learn that the hydrogen partial pressure increases to 10^{-7} mbar, while all other gases remain at least one order of magnitude lower in pressure. Other reactive gases such as O_2 and H_2O remain well below the $5\text{x}10^{-8}$ mbar level. Hydrogen evolves from the metallic (α-phase) yttrium target in which some hydrogen is dissolved. As the c-axis length of yttrium in the α-phase depends linearly on the hydrogen content, we estimate from the XRD spectrum that the hydrogen content of the target is approximately 7 at% hydrogen (Fig. 2.2).

To investigate the hydrogen evolution from the target, we measured the H_2 (mass=2) signal of the mass spectrometer as a function of time and fluence, at a laser repetition frequency of 5 shots per second on a stationary target. The amount of hydrogen increases with the laser fluence and increases steadily with time up to a fluence of 0.6 J cm^{-2} (Fig. 2.3). At higher fluences the hydrogen pressure has a maximum in time. Apparently, hydrogen is depleted from the yttrium target surface when $F > 0.6$ J cm^{-2}. Below this fluence a steady flow of hydrogen can be maintained.

To prevent the depletion of hydrogen at high fluences, we could increase the time

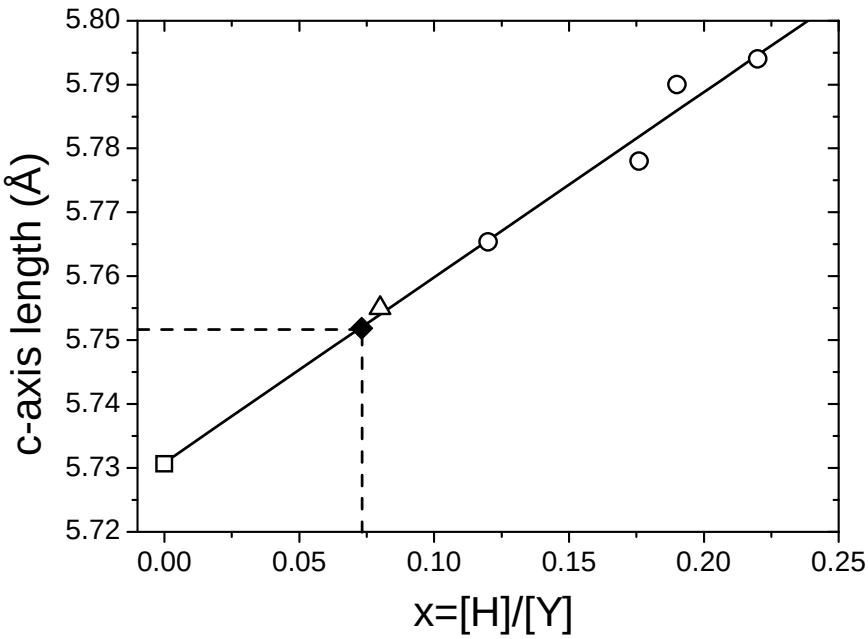

Figure 2.2: Determination of the hydrogen content of the yttrium target from the c-axis length. Open circles are data from Vajda [8], the open triangle from ref [9], the open square from ref [10] and the filled diamond represents our measurement. A c-axis length of 5.752 $\AA$ gives a hydrogen concentration of 7 at%.

between two laser pulses, thereby increasing the recovery time for replenishment. However, the deposition rate of yttrium would decrease simultaneously. Therefore, during the actual deposition process we *rotate* the target creating a circular track of laser ablation imprints on the target. As a result, the time between two ablation events at the same target position increases from 0.2 s to 4 s. In the latter case, we find a steady increase in hydrogen pressure with time during deposition, even at our standard deposition fluence of 0.7 J cm^{-2}, indicating a critical recovery time between 0.2 and 4 s.

If the laser plasma is allowed to condense on a CaF_2 substrate heated to 400-600 °C we obtain an epitaxial YH_2 film. The X-ray spectrum only shows the (111) and higher order reflections of the YH_2 phase (Fig. 2.4a). Metallic yttrium is not found. Around $2\theta = 26°$ we find proof for the presence of a small amount of $Y(OH)_3$. A texture measurement (a phi-psi scan with 2θ fixed at the (111) reflection of YH_2) showed the six-fold arrangement of symmetry equivalent (111)-reflections (two sets of (111)-reflections appear due to twinning [11]), which confirms the epitaxial nature of the YH_2 film (Fig. 2.4b). Nanocrystalline films were obtained when depositing at room temperature on a quartz substrate (Fig. 2.4c). Though we again expect the presence of some $Y(OH)_3$, this could not be identified in the XRD spectrum.

Although the plateau pressure of YH_2 at room temperature is of the order of

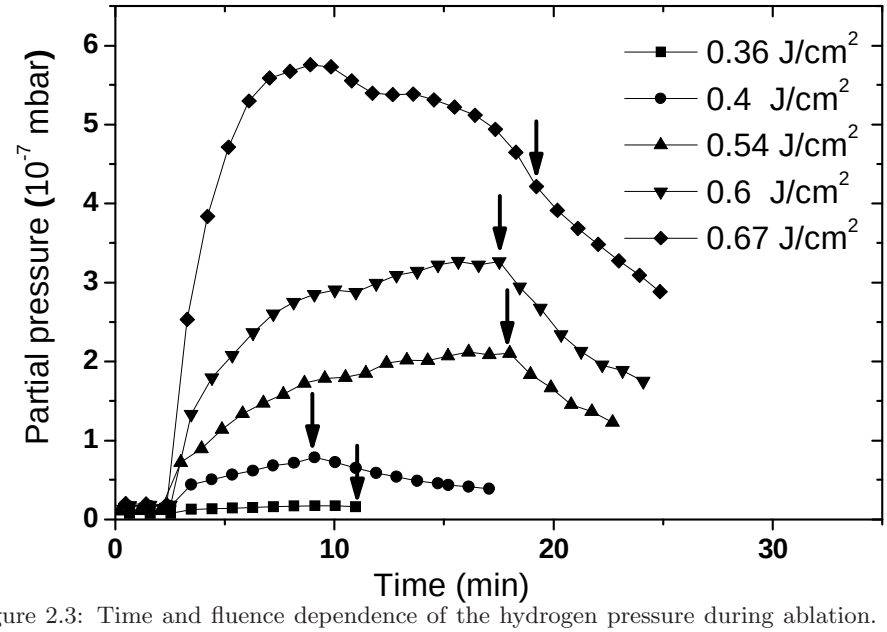

Figure 2.3: Time and fluence dependence of the hydrogen pressure during ablation. The RGA is positioned approximately 12 cm away from the plume. The amount of hydrogen increases as soon as the ablation starts (at $t = 3$ min) and increases steadily with time up to a fluence of 0.6 J cm^{-2}. At higher fluences the hydrogen pressure has a maximum in time. Arrows indicate when the ablation was halted and show a decrease in the partial hydrogen pressure. In this experiment the target is stationary, as opposed to rotation during actual deposition.

10^{-25} mbar, the direct formation of YH_2 is not trivial. To deposit YH_2-films under similar conditions in, for example, MBE, elaborate hydrogen purification and conditioning of the vacuum system are needed [12]. The fact that YH_2 is nevertheless formed in a relatively dirty PLD system, is either due to the pulsed nature of the PLD process, or due to the formation of atomic hydrogen. Although atomic hydrogen is the most likely ablation product, in our RGA analysis the H/H_2 ratio never exceeded 10%, not even when the ion-source of the mass spectrometer was positioned just above the ablation plume. Hence, we have no evidence that *atomic* hydrogen plays a significant role in the deposition process. We conclude therefore that the simultaneous pulsed supply of highly kinetic Y and hydrogen is responsible for the YH_2 formation.

For the all-solid-state switchable mirror device the reduced reactive gas load in this hydride PLD process is an advantage. In such switchable devices, metal and oxide functional layers have to be deposited subsequently. In order to prevent cross-contamination and facilitate a quick change of reactive gases, the deposition system should have a decent pumping capacity and the reactive gas load should be minimized.

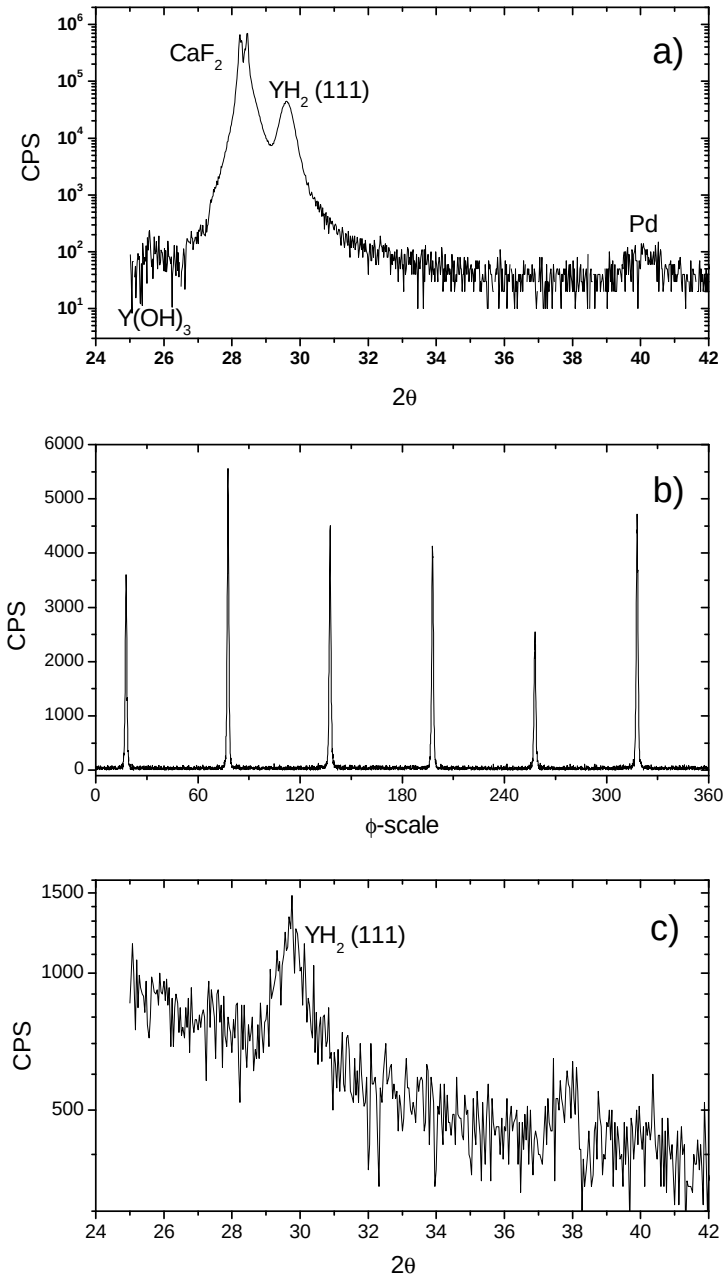

Figure 2.4: a) XRD $\theta - 2\theta$ scan of YH_2 film showing the preferential (111)-orientation of the fcc structure. b) Texture analysis of the (111)-reflection showing the 6-symmetry equivalent (111)-directions, confirming the epitaxial (albeit twinned) nature of the YH_2 films. c) At low substrate temperatures the peak intensity of the $\theta - 2\theta$ scan is enormously reduced as shown here.

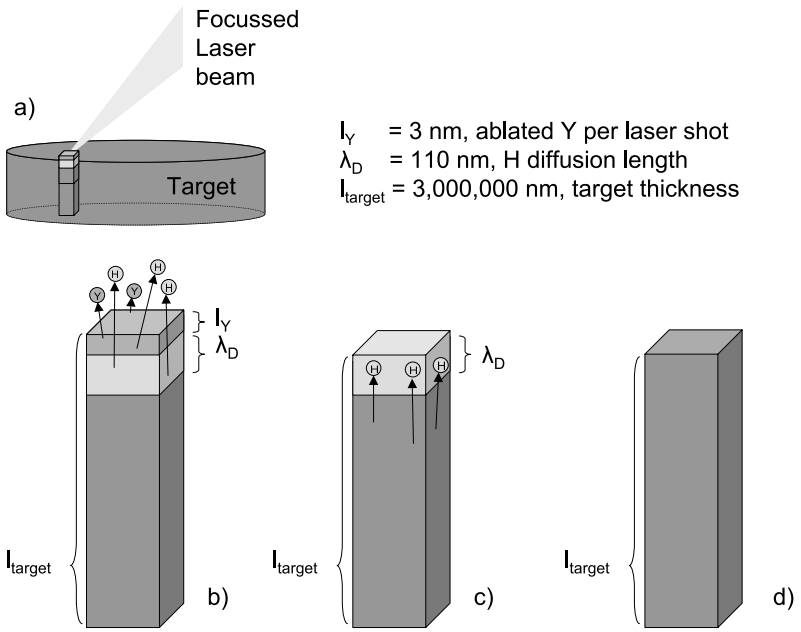

Figure 2.5: Schematic representation of the preferential hydrogen ablation and replenishment between the laser pulses. During one laser shot a 3 nm thick yttrium layer is ablated. The diffusion length of hydrogen in the molten yttrium during the 25 ns laser pulse is $\lambda_D = 110$ nm. Between the laser pulses, the hydrogen depleted surface area is replenished by hydrogen diffusion.

2.3.2 Diffusion assisted preferential hydrogen ablation

PLD is well-known for its ability to deposit congruent films from complex targets. However, as explained elsewhere, at low fluences target surface processes may preclude such congruent deposition and one of the target compounds may be preferentially ablated [13]. This non-stoichiometric ablation process may be maintained through a continuous supply of this compound towards the target surface by diffusion. As the diffusion of hydrogen is very fast, we propose a similar mechanism for the formation of YH_2. To explain the hydrogen enrichment of PLD yttrium films we need to assume: (1) preferential ablation of hydrogen during laser irradiation of the target and (2) sufficient internal hydrogen diffusion towards the target surface between two laser pulses.

If there is a strong preference to withdraw H from the $YH_{0.07}$ target during ablation, a H concentration gradient will set in. The concentration gradient is a driving force for diffusion towards the target surface. The mean diffusion length of the hydrogen during one laser pulse is roughly $\lambda_D = \sqrt{D_{H,m} \cdot \tau} \approx 110$ nm, in which

$D_{H,m}$ is the diffusion coefficient of hydrogen in molten yttrium (= $5{\cdot}10^{-3}$cm^{2}s^{-1}) and τ is the duration of the laser pulse (= 25 ns) (see Figure 2.5). At 0.7 J cm^{-2} one laser pulse ablates a 3 nm thick layer from the yttrium target surface (as determined by measuring the weight of the target before and after deposition). During this single laser shot hydrogen atoms from a depth of 110 nm may diffuse towards the target surface. As a result the H atoms present in the plasma due to a single laser shot can be ∼37 times larger than the number of H atoms present in the 3-nm layer of yttrium. This compares well with the ∼29-fold increase in hydrogen concentration from film to target and it shows that during a single laser shot a preferential ablation of hydrogen can be maintained by diffusion. Note, that PLD is not a simple evaporation process. The laser induced plasma formation is several orders of magnitude faster than the evaporation rate. We therefore assume, that hydrogen only evolves from the target during laser irradiation and that the evaporation of hydrogen from the target after the laser pulse is negligible.

After each laser pulse, the surface area of the yttrium target is depleted in hydrogen. Diffusion towards the surface from underlying layers will take place between the laser pulses. The very small volume heated by the laser beam quickly cools as soon as the laser pulse has stopped. If the time between the laser pulses is too short for the target to recover, the amount of hydrogen desorbed will decrease in the subsequent laser pulses. We observe such depletion effects when the time between two laser pulses is decreased from 4 to 0.2 s. This suggests an average hydrogen diffusion coefficient between $3 \cdot 10^{-11} < D_{H,Y} < 6 \cdot 10^{-10}$ cm^{2}s^{-1}. These are typical values for hydrogen diffusion in Y at temperatures between 350 and 410 K [14]. Hence, it appears that the target cooldown after each laser shot is the limiting factor to replenish the target surface.

We conclude that the incongruent deposition of YH_2 is due to a preferential ablation of hydrogen, which is assisted by hydrogen diffusion. During the laser shot, fast diffusion towards the ablated surface allows the hydrogen desorption to persist. Between the laser shots, sub-surface target depletion is replenished by low temperature hydrogen diffusion.

2.3.3 Morphological and structural properties

The surface morphology of the in-situ PLD YH_2 films is quite different from that of MBE-grown epitaxial Y films, which are ex-situ loaded to the YH_2 phase. These ex-situ hydrogenated thin films are characterized by flat crystalline regions with crystal growth steps, separated by large 'plate-like' protrusions [7, 15] as shown in Fig. 2.6a. This triangular ridge pattern is the result of a special kind of twinning; the (111)-direction being tilted by ∼90 degrees with respect to the main epitaxial orientation [11]. The initially formed ridge pattern is due to strain relaxation via misfit glides during growth [16]. Hydrogenation increases the amount of ridges [7] and causes the formation of a large amount of twin boundaries [11]. The triangular domains switch independently, the ridges acting as lateral hydrogen diffusion barriers [15, 17, 18].

Epitaxial PLD grown YH_2 films are formed at much lower substrate tempera-

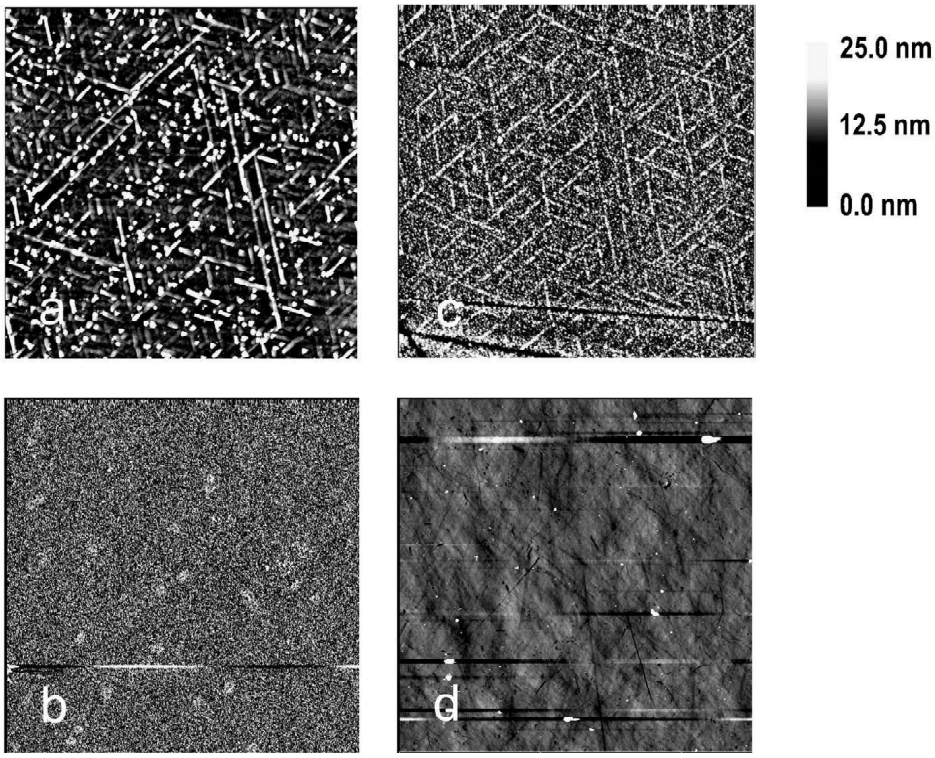

Figure 2.6: AFM tapping micrographs of YH_2 films. All images have the same height scale and have the same size (25x25 micrometers). a) Ex-situ hydrogenated epitaxial MBE film with typical ridge pattern. b) In-situ grown epitaxial PLD film with typical morphology. c) In-situ grown epitaxial PLD film. Ridges are only observed when using deposition temperatures above 500°C. These ridges consist of elevated grains. d) In-situ grown nanocrystalline YH_2 film at room temperature on quartz. The surface has a flat and wavy appearance. The horizontal lines are artifacts caused by the large contrast in height of some particles on the film surface.

tures compared to the MBE Y films (at $\sim$ 500 instead of 700°C, respectively). As demonstrated in Fig. 2.6b the PLD films are virtually particulate free. The grain size is around 30 nm, which precludes the observation of surface steps by AFM. Only for samples prepared at deposition temperatures above 500°C we find something of a ridge structure (Fig. 2.6c). The ridge, however, is now an area where grains are protruding slightly above their surroundings. The absence of ridges is an advantage for devices since these surface protrusions could cause electrical shorts through the electrolyte layer. Nanocrystalline YH_2 films (Fig. 2.6d) deposited at room temperature on quartz substrates have the lowest surface roughness compared to epitaxial PLD and MBE films ($r_{rms} = 0.6$ nm, $r_{rms} = 4$ nm and $r_{rms} = 1.8$ nm, respectively).

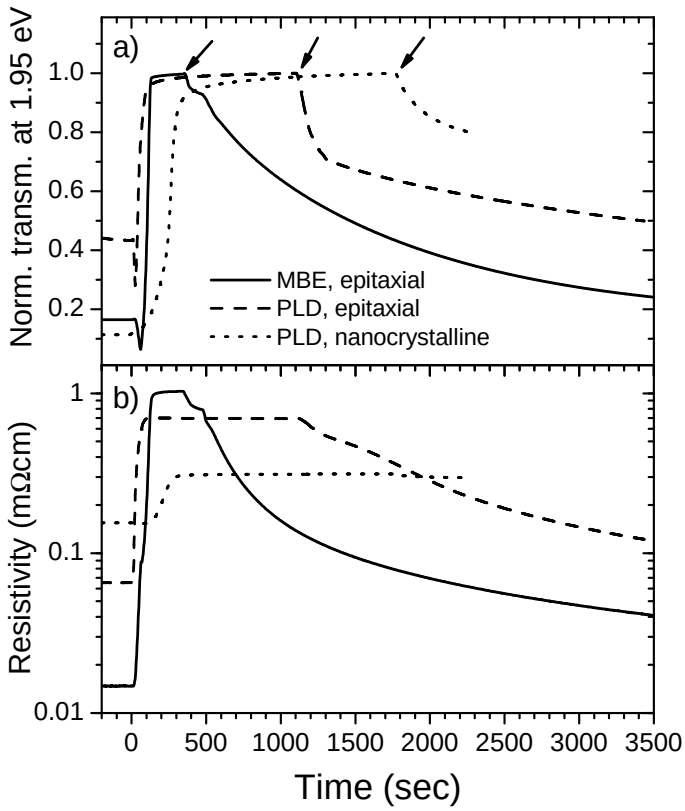

Figure 2.7: Comparison of the switching behavior of in-situ grown PLD YH_2 films with an ex-situ hydrogenated MBE YH_2 film during loading and unloading to the YH_3 phase. Arrows indicate the onset of hydrogen desorption. a) Normalized transmission at $\lambda = 635$ nm ($\hbar\omega = 1.95$ eV). In both epitaxial films the transmission drops before it starts to rise. The dip is absent for the nanocrystalline film. b) Resistivity. The change in resistivity is smallest for the nanocrystalline film.

These randomly oriented films have wavy surfaces without ever showing any ridge formation, nor can any individual grain be discerned.

2.3.4 Optical switching properties

In Figure 2.7 we compare the shape of the normalized transmission at 1.95 eV during hydrogenation of the MBE-grown film with the PLD-grown films, both epitaxial and nanocrystalline. In both epitaxial films the transmission first drops before it starts to rise. This corresponds to a commonly observed darkening within the dihydride phase upon loading in H_2 [2, 19]. The dip is absent in nanocrystalline films.

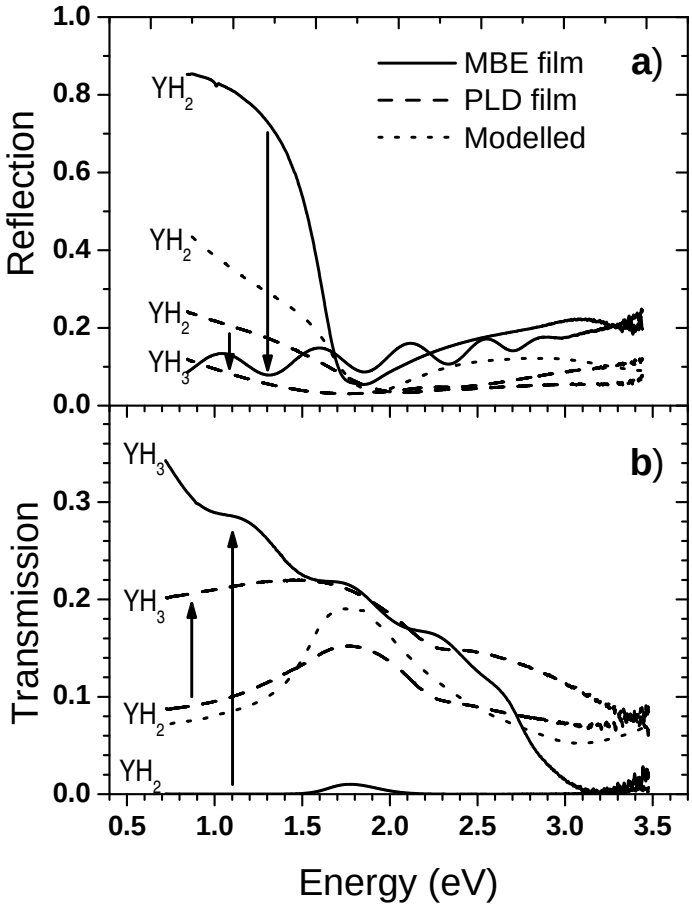

Figure 2.8: Comparison of the optical properties over a wide spectral range of the YH_2 and the $YH_{3-\delta}$ phase for epitaxial PLD (70 nm) and MBE (150 nm) grown films. a) Reflection. b) Transmission. The finite transmission at energies larger than the yttrium band gap, $E > E_g^{YH_3}$, indicates the presence of secondary phases. An 70 nm thick modelled film of a Bruggeman mixture of 60% yttrium dihydride and 40% yttrium oxide covered by a 10 nm thick Pd layer is represented by the dotted line

As seen in Figure 2.7b the resistive transition shows a much wider dynamic range in the MBE films than in the PLD films. The starting point of all films is the dihydride phase. MBE films in the β-phase have a lower resistivity than the PLD deposited films. The change in resistivity is smallest for nanocrystalline films.

The same differences in switching contrast between PLD and MBE films are observed when plotting the optical spectrum from 0.7 to 3.5 eV (Fig. 2.8b compared to Fig. 2.7b). Additionally, the transmission in the hydrogenated state extends

to much higher photon energies in the PLD than in the MBE films. Moreover, the reflection shows a larger variation at the low photon energy region (NIR) for the MBE film than for the PLD film (Fig. 2.8a). These observations suggest the presence of impurity phases, such as oxides and/or hydroxides [20]. Indeed, we observed a small amount of $Y(OH)_3$ as a secondary phase by XRD (see Section 2.3.1). Furthermore, we observe around 40% of oxygen in this sample by RBS. The presence of a secondary oxygen phase is confirmed by optically modelling (see Section 3.2.2) a Bruggeman mixture of 60% yttrium hydride and 40% yttrium oxide [21], which is added in Figure 2.8 as a dotted line. Both the high transmission as well as the low reflection are reproduced.

Combining the optical and resistivity data one observes a remarkable absence of any hysteresis in the hydrogenation behavior of the nanocrystalline PLD films (Fig. 2.9). As the resistivity is directly coupled to the H-concentration this means that the optical properties are uniquely determined. Especially the region at high resistivities is interesting in view of the implementation in a device, since the transmission doubles in only a very small resistivity range. The origin of the large hysteresis [22] in both optical transmission and pressure-composition isotherms in MBE films was described by Remhof *et al.* [23]. Upon loading with H_2, first a dark β-phase ($YH_{2.1}$) is formed before the system crosses the miscibility gap and $YH_{2.7}$ nucleates. Upon dehydrogenation the more transparent $YH_{1.9}$-phase is formed, which coexists together with the hexagonal $YH_{2.65}$ phase. This difference in hydrogen concentration of both phases is due to the different stress states during hydrogenation and dehydrogenation. The hysteresis can be quenched by addition of La. For $La_{1-z}Y_zH_x$ with $z \leq 0.67$ no uniaxial expansion is observed due to the absence of a phase transition [3, 24]. Examining the nanocrystalline film in more detail, we find, in contrast to the epitaxial PLD films, that the c-axis remains almost constant during loading (Figure 2.10). Hence the film probably remains in the fcc-phase during hydrogen loading. Apparently, the randomly oriented grains are too small to be transformed to the hcp-phase [25]. Note, that the lattice parameter at low hydrogen concentrations is large compared to bulk values, which is common for nanocrystalline materials [26].

2.3.5 Oxygen-free films

We find that, although the PLD-films are promising in terms of surface flatness and hysteresis, the optical contrast on switching is severely reduced. The results from Rutherford backscattering spectrometry (RBS) and the behavior of the optical properties indicate that this is due to oxygen contamination. The yttrium oxide and hydroxide are more stable then the hydride: $\Delta H_f = -1934$ kJ/mol Y_2O_3 [27] and $\Delta H_f = -1472.3$ kJ/mol $Y(OH)_3$ [28] as compared to $\Delta H_f = -228$ kJ/mol YH_2 [29].

When ablation of the target is started, the partial oxygen pressure increases as well as the hydrogen pressure, although less dramatically, i.e. the partial oxygen pressure stays below $5 \cdot 10^{-8}$ mbar during ablation. Since at a pressure of 10^{-6} mbar, one monolayer is deposited per second, the amount of oxygen on the sample due to

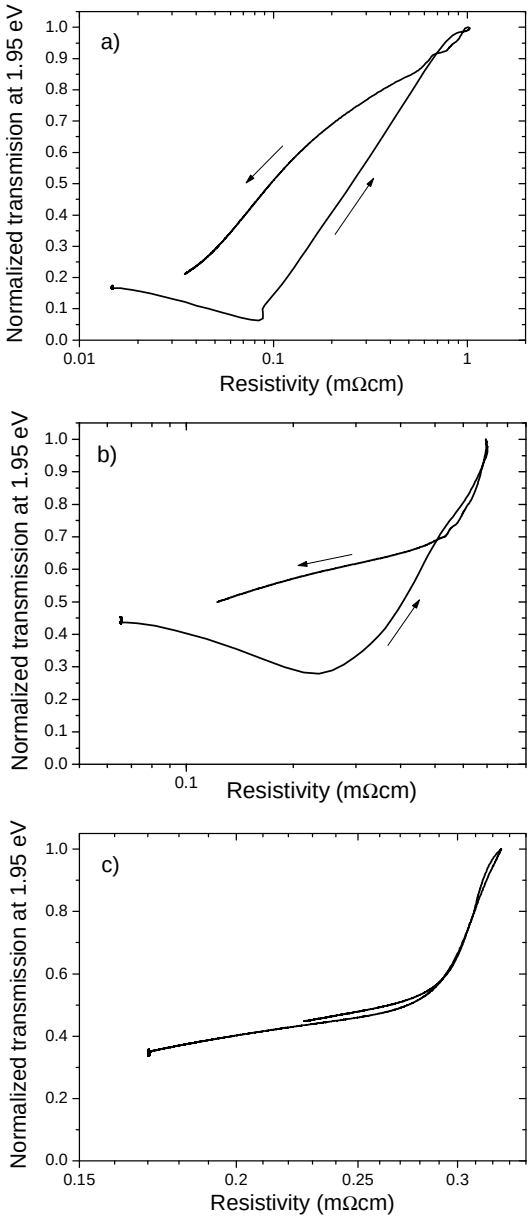

Figure 2.9: Combining resistivity and transmission during hydrogenation and dehydrogenation reveals the presence or absence of hysteresis in switching from the YH_2 to the YH_3 state. Dehydrogenation is in air at room temperature. a) Epitaxial MBE Y film. b) Epitaxial PLD film. c) Nanocrystalline PLD films. Only these films switch hysteresis free. Note the different scales.

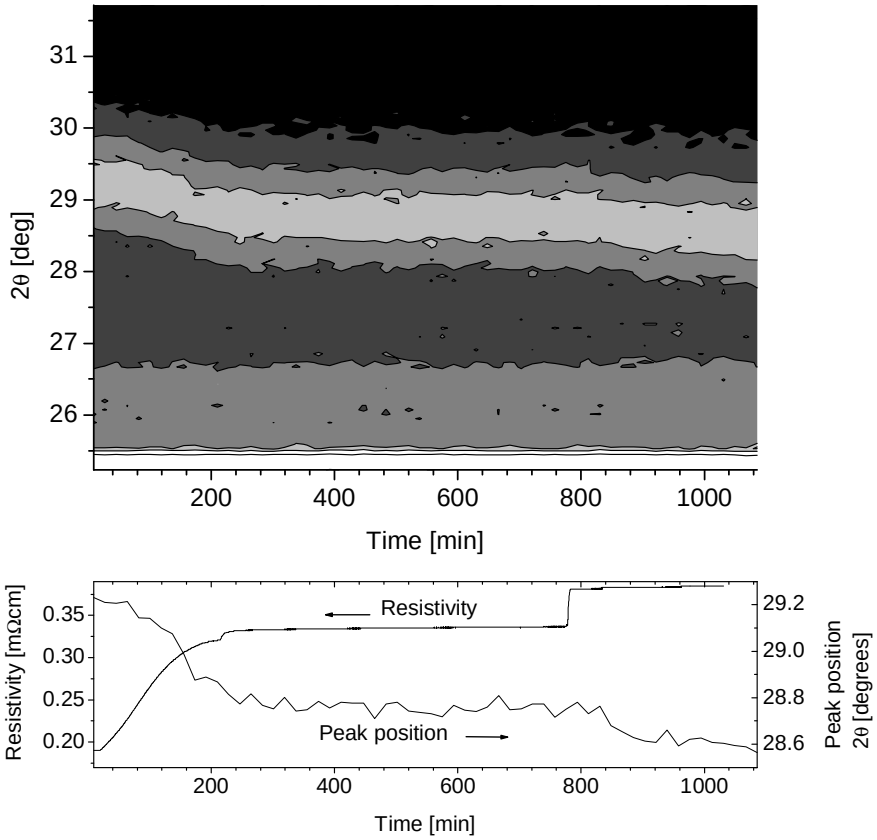

Figure 2.10: During loading of a nanocrystalline YH_2 film with hydrogen up to 1 bar the Bragg-peak shifts to lower angles indicating a lattice expansion due to hydrogen incorporation. The fcc to hcp phase transition is suppressed for nanocrystalline materials.

the background pressure, will not be more then 0.05 monolayers per second. The yttrium deposition rate is approximately one monolayer per second, so we have a maximum of $YO_{0.05}$, which is less than the $YO_{0.67}$ observed. Therefore, we conclude that the oxygen deterioration does not come from the background pressure.

The fact that the partial oxygen pressure increases upon target ablation points in the direction of the target being the source of the oxygen deterioration of our films. However, it is very unlikely that the oxygen contamination is due to diffusion assisted preferential ablation, the same mechanism as for hydrogen, since the diffusion of oxygen is orders of magnitude smaller than that of hydrogen. Therefore, the replenishment of the target surface with oxygen is unlikely. The amount of oxygen in the target is unknown. The target has an oxide layer at the surface, which is observed by XRD-measurements and disappears after polishing of the target surface.

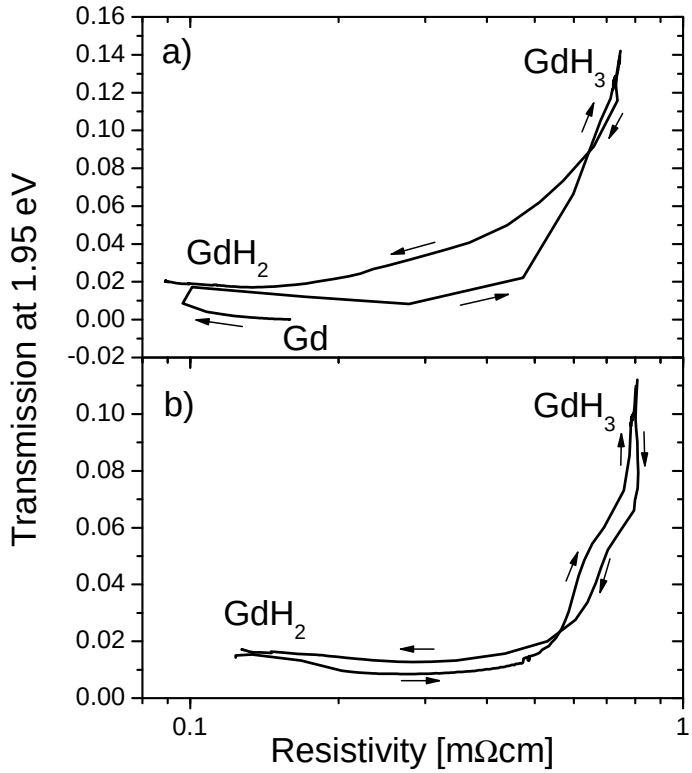

Figure 2.11: Transmission versus electrical resistivity during hydrogenation up to 1 bar H_2 at room temperature and dehydrogenation in air at 90°C. a) Combining resistivity and transmission during hydrogenation and dehydrogenation reveals the presence or absence of hysteresis in switching for the Gd film deposited with the use of a clean target. a) Metallic Gd-film showing hysteresis. b) In-situ grown GdH_2 film with almost no hysteresis. Optical and RBS measurements show a decreased oxygen concentration as compared to the YH_2 films. The optical range has increased considerably.

The target is always pre-ablated before the real ablation starts in order to get rid of this surface oxide. However, oxygen might have diffused along the grain boundaries of the target, formed (x-ray amorphous) yttrium-oxide which contaminated the yttrium films, even in the absence of replenishment by diffusion.

To prevent the formation of RE-oxides, the use of a contaminated target should be avoided. Since we have a highly purified Gd-target available with an oxygen content of only 304 at ppm, this target is used in the PLD set-up. This allows us to confirm the cause of the oxide formation and to improve the optical contrast of our films.

First, the pure Gd-target is used to prepare metallic films at room temperature.

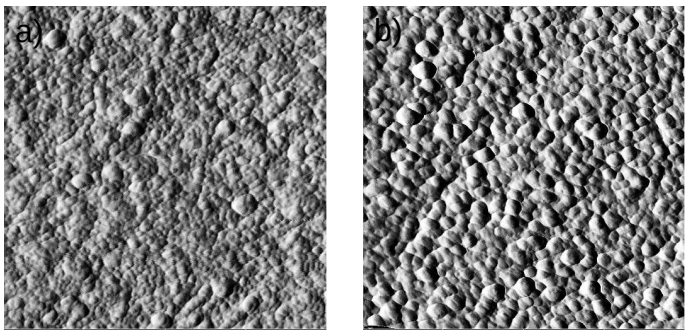

Figure 2.12: AFM tapping micrographs of a) as-deposited metallic 110 nm thick Gd film with an average grain size of ≈25 nm and a surface roughness of r_{rms} = 3 nm and b) as-deposited 70 nm thick GdH_2 film with an average grain size of ≈50 nm and a surface roughness of r_{rms} = 4 nm. Both pictures are 1 x 1 μm^2.

The transmission as a function of the resistivity is plotted in Fig. 2.11a. Clearly, hysteresis is observed. Then, we increased the hydrogen content of the Gd-target by ablation in a reactive hydrogen atmosphere. The films deposited hereafter are in the dihydride state, as observed by the transmission window, around 1.7 eV. Now, the transmission around 0.7 eV and 3.5 eV is zero, indicating the absence of oxygen, as is confirmed by RBS. Figure 2.11b shows the transmission as a function of the resistivity for the in-situ deposited nanocrystalline GdH_2 films. Almost no hysteresis is observed and the contrast ratio has markedly improved, i.e. by a factor of 13.

Figure 2.12 shows the AFM pictures of an as-deposited metallic and in-situ grown dihydride film. The absence of hysteresis depends on the absence of an uniaxial expansion due to a phase transition, which is believed to be suppressed by a reduced grain size. Therefore, the grain size of the in-situ dihydride film is expected to be smaller compared to the metallic films, because of the absence of hysteresis in the first one. However, the grain size of the dihydride and metallic film are 50 and 25 nm, respectively. The surface roughness is low, as for the Y-films, namely r_{rms} = 4 nm and r_{rms} = 3 nm for the dihydride and metallic film, respectively. Further analysis is needed to identify the reason for the absence of hysteresis in GdH_2

2.4 Conclusions

PLD facilitates the in-situ formation of YH_2 films at low hydrogen background pressures. The deposition process is extremely incongruent. Due to diffusion assisted preferential ablation this incongruent deposition process can be maintained. Crucial is the replenishment of the target between the shots. The PLD process has the advantage that a complicated hydrogen purification is unnecessary. Moreover, the gasload during deposition is minimal, which is beneficial for the fabrication of hetero-

structures consisting of metal, hydride and oxide functional layers.

The in-situ growth process allows us to study the switching behavior as a function of the crystallinity. Depending on the substrate temperature, the crystallinity of the film ranges from epitaxial ($T_s = 500°C$) to nanocrystalline (T_s=room temperature). The nanocrystalline films remain in the fcc phase upon hydrogen loading. As a result, we do not observe a hysteresis in these films. Surface flatness, the absence of hysteresis and a steep optical transition are important advantages if these materials are to be incorporated in all-solid-state chromogenic devices. Oxygen contamination can be prevented by using a highly purified Gd-target.

Bibliography

[1] C.G. Granqvist, A. Azens, A. Hjelm, L. Kullman, G.A. Niklasson, D. Rönnow, M. Strømme Mattsson, M. Veszelei, and G. Vaivars. Recent advances in electrochromics for smart windows applications. *Sol. Energy*, 63(4):199–216, 1998.

[2] J.N. Huiberts, R. Griessen, J.H. Rector, R.J. Wijngaarden, J.P. Dekker, D.G. de Groot, and N.J. Koeman. Yttrium and lanthanum hydride films with switchable optical properties. *Nature*, 380:231–234, 1996.

[3] A.T.M. van Gogh, D.G. Nagengast, E.S. Kooij, N.J. Koeman, and R. Griessen. Quenching of giant hysteresis effects in $La_{1-z}Y_zH_x$ switchable mirrors. *Phys. Rev. Lett.*, 85(10):2156–2159, 2000.

[4] A.F.Th. Hoekstra, A.S. Roy, T.F. Rosenbaum, R. Griessen, R.J. Wijngaarden, and N.J. Koeman. Light induced metal–insulator transition in a switchable mirror. *Phys. Rev. Lett.*, 86(23):5349–5352, 2001.

[5] R. Armitage, M. Rubin, T. Richardson, N. O'Brien, and Yong Chen. Solid-state gadolinium-magnesium hydride optical switch. *Appl. Phys. Lett.*, 75(13):1863–1865, 1999.

[6] P. van der Sluis and V.M.M. Mercier. Solid state Gd-Mg electrochromic devices with ZrO_2H_x electrolyte. *Electrochim. Acta*, 46:2167–2171, 2001.

[7] D.G. Nagengast, J.W.J. Kerssemakers, A.T.M. van Gogh, B. Dam, and R. Griessen. Epitaxial switchable yttrium-hydride mirrors. *Appl. Phys. Lett.*, 75(12):1724–1726, 1999.

[8] P. Vajda. *Handbook on the Physics and Chemistry of Rare Earth*, volume 20, chapter 137, page 207. Elsevier, Amsterdam, 1995.

[9] J.N. Huiberts, J.H. Rector, R.J. Wijngaarden, S. Jetten, D. de Groot, B. Dam, N.J. Koeman, R. Griessen, B. Hjörvarsson, S. Olafsson, and Y.S. Cho. Synthesis of yttriumtrihydride films for ex-situ measurements. *J. Alloys. Comp.*, 239:158–171, 1996.

[10] F.H. Spedding, A.H. Daane, and K.W. Herrmann. The crystal structures and lattice parameters of high-purity scandium, yttrium and rare earth metals. *Acta Cryst.*, 9:559, 1956.

[11] B.J. Kooi, E. Zoestbergen, J.Th.M. De Hosson, J.W.J. Kerssemakers, B. Dam, and R.C.C. Ward. Mechanism of the structural phase transformations in epitaxial YH_x switchable mirrors. *J. Appl. Phys.*, 91(4):1901–1909, February 2002.

[12] J. Hayoz, Th. Pillo, M. Bovet, A. Züttel, St. Guthrie, G. Pastore, L. Schlapbach, and P. Aebi. Preparration and characterization of clean, single-crystalline YH_x films ($0 < x < 2.9$) on W(110). *J. Vac. Sci. Technol., A*, 18(5):2417–2431, 2000.

[13] B. Dam, J.H. Rector, J. Johansson, J. Huijbregtse, and D.G. de Groot. Mechanism of incongruent ablation of $SrTiO_3$. *J. Appl. Phys.*, 83(6):3386–3389, March 1998.

[14] Sense Jan van der Molen. *Hydrogen Migration in Switchable Mirrors.* PhD thesis, VU Amsterdam, January 2002.

[15] J.W.J. Kerssemakers, S. J. van der Molen, N.J. Koeman, R. Günther, and R. Griessen. Pixel switching of epitaxial $Pd/YH_x/CaF_2$ switchable mirrors. *Nature*, 406:489–491, 2000.

[16] A. Borgschulte, S. Weber, and J. Schoenes. Interfacial reaction during the epitaxial growth of yttrium on CaF_2 (111). *Appl. Phys. Lett.*, 82(17):2898–2900, 2003.

[17] J.W.J. Kerssemakers, S.J. van der Molen, R. Günther, B. Dam, and R. Griessen. Local switching in epitaxial YH_x switchable mirrors. *Phys. Rev. B*, 65(7):075417, 2002.

[18] J.W.J. Kerssemakers, S.J. van der Molen, R. Günther, B. Dam, and R. Griessen. In situ monitoring of optical and structural switching in epitaxial YH_x switchable mirrors. *J. Alloys Compd.*, 330-332:342–347, 2002.

[19] E.S. Kooij, A.T.M. van Gogh, and R. Griessen. In situ resistivity measurements and optical transmission and reflection spectroscopy of electrochemically loaded switchable YH_x films. *J. Electrochem. Soc.*, 146(8):2990–2994, 1999.

[20] M. Miniotas, B. Hjörvarsson, and L. Douysset. Gigantic resistivity and band gap changes in GdO_yH_x thin films. *Appl. Phys. Lett.*, 76(15):2056–2058, 2000.

[21] E.D. Palik. *Handbook of Optical Constants of Solids book.* Academic Press, San Diego, 1998.

[22] E.S. Kooij, A.T.M. van Gogh, D.G. Nagengast, N.J. Koeman, and R. Griessen. Hysteresis and the single-phase metal-insulator transition in switchable YH_x films. *Phys. Rev. B*, 62(15):10088–10100, 2000.

[23] A. Remhof, J.W.J. Kerssemakers, S.J. van der Molen, R. Griessen, and E.S. Kooij. Hysteresis in YH_x films observed with *in situ* measurements. *Phys. Rev. B*, 65:054110, 2002.

[24] A.T.M. van Gogh, D.G. Nagengast, E.S. Kooij, N.J. Koeman, J.H. Rector, and R. Griessen. Structural, electrical and optical properties of $La_{1-z}Y_zH_x$ switchable mirrors. *Phys. Rev. B*, 63:195105, February 2001.

[25] L. Zaluski, A. Zaluska, and J.O. Ström-Olsen. Nanocrystalline metal hydrides. *J. Alloys Compd.*, 70-79:2417–2431, 1997.

[26] W. Qin, Z.H. Chen, P.Y. Huang, and Y.H. Zhuang. Crystal lattice expansion of nanocrystalline materials. *J. Alloys Compd.*, 292:230–232, 1999.

[27] A.R. Wildes, R.C.C. Ward, M.R. Wells, and B. Hjorvarsson. The formation of epitaxial YH_2 in MBE grown yttrim thin films with a thin gold capping layer. *J. Alloys Compd.*, 242:49–57, 1996.

[28] I.I. Diakonov, K.V. Ragnarsdottir, and B.R. Tagirov. Standard thermodynamic properties and heat capacity equations of rare earth hydroxides: Ii. Ce(iii)-, Pr-, Sm-, Eu(iii)-, Gd-, Tb-, Dy-, Ho-, Er-, Tm-, Yb-, and Y-hydroxides. comparison of thermochemical and solubility data. *Chem. Geol.*, 151:327–347, 1998.

[29] A.S. Chernikov, V.I. Savin, V.N. Fadeev, N.A. Landin, and L.A. Izhvanov. Thermodynamic and physical properties of yttrium and some rare eatth hydrides. *J. Less-Common Met.*, 130:441–452, 1987.

Chapter 3

Mg-TM-hydrides

Switchable metal-hydride layers change their optical properties reversibly with changing hydrogen concentration. At low concentrations, they are reflecting, while at high hydrogen content a transparent state is observed. Mg-Ni hydride films show a fascinating absorbing black state at intermediate hydrogen concentrations, which is interesting for the use as switchable absorbers for solar collectors. In this chapter we study the optical properties of fully hydrogenated Mg_yTM (TM=Co, Fe) thin films at photon energies between 0.2 and 5.5 eV and compare them with Mg_yNi. In addition, we investigate the intermediate optical black state caused by a self-organized double layer formation which is sometimes observed during hydrogen loading. The optical behavior is found to depend on the Mg-to-TM ratio, the specific transition metal used and the hydrogenation history. We argue that the presence of crystalline Mg promotes homogeneous nucleation by acting as nucleation sites in Mg_yTMH_x films (TM=Co, Fe). Furthermore, we propose Mg_yNi with $y = 6$ as the most suitable candidate for the use as a switchable absorber in an all-solid-state device.

3.1 Introduction

Mg_yTMH_x (TM=Ni, Co, Fe) thin films show drastic changes of their optical appearance upon hydrogen uptake at room temperature [1, 2]. The reversible switching between a reflecting metallic and a transparent semiconducting state make these films suitable for use as switchable mirrors [3]. In addition, in Mg_2NiH_x, Isidorsson *et al.* [4] found a peculiar black state at intermediate hydrogen concentration. This absorbing state extends over the whole solar range when using an optimized Mg-to-Ni ratio [5]. The absorbing nature of the Mg_yNiH_x is essentially an interference effect due to a self-organized double-layering. The Mg_yNi-hydride layer nucleates at the substrate-film interface and grows on hydrogenation at the expense of the upper $Mg_2NiH_{0.3}$ layer. As a result of the high contrast between the reflective and the absorbing state, Mg_yNiH_x can be used as a switchable solar absorber.

In this chapter we compare in some detail the hydrogen loading behavior and optical properties of Mg_2NiH_4, Mg_2CoH_5 and Mg_2FeH_6 thin films at various Mg-TM ratios. Note, that we use the term Mg_yTM to indicate the different ratios of Mg and TM present in a phase mixture, possibly containing both metal and alloy phases. Despite the fact that the MgTM-hydrides all conform the 18-electron rule and thus are expected to have approximately the same properties, there are some differences between the Mg-Ni, Mg-Co and the Mg-Fe system. First of all, the metal phase diagrams of the bulk materials are clearly different (Figure 3.1). Only in the case of Mg-Ni does a binary Mg-TM parent alloy exist with the same metal composition as the ternary Mg_2TMH_x hydride [6]. For the Mg-Co and Mg-Fe systems, such a binary Mg_2TM compound is not known. In the Mg-Co system two other binary intermetallic phases are reported: hexagonal $MgCo_2$ and cubic MgCo [7, 8], while for the Mg-Fe system no binary intermetallic compound has been found. Hence, only Mg_2NiH_4 is formed from the corresponding Mg_2Ni compound, while Mg_2CoH_5 [9, 10] and Mg_2FeH_6 are formed from the elements. Only in the Mg-Co case has a second complex hydride been reported, orthorombic $Mg_6Co_2H_{11}$ [11, 12].

In the Mg-TM (TM=Ni, Co, Fe) hydrides, mainly the hydrogen arrangement around the TM is different (Fig. 3.2). The TM-hydrides form tetrahedral $[Ni^0H_4]^{4-}$, square-pyramidal $[Co^{+1}H_5]^{4-}$ and octahedral $[Fe^{+2}H_6]^{4-}$ complexes, respectively. The sum of the valence electrons of the hydrogen complex always is 18, i.e. they all conform the 18-electron rule. Gupta *et al.* calculated the density of states of the Mg_2TMH_x. They found a semiconducting behavior for all Mg_2TMH_x (TM=Ni, Co, Fe) with band gaps of 1.36 eV [13], 1.92 eV [14] and 1.74 eV [15, 16], respectively and an experimental band gap of bulk Mg_2CoH_5 of 2.0 eV [14]. The optical band gap of Mg_2NiH_4 thin films was experimentally determined to be ∼1.6 eV [17, 18]. In Mg_yNiH_x the gap increases in the presence of MgH_2 [1, 17, 19]. A band gap of $E_g = 5.6$ eV was determined from the diffuse transmission of a MgH_2 thin film [20].

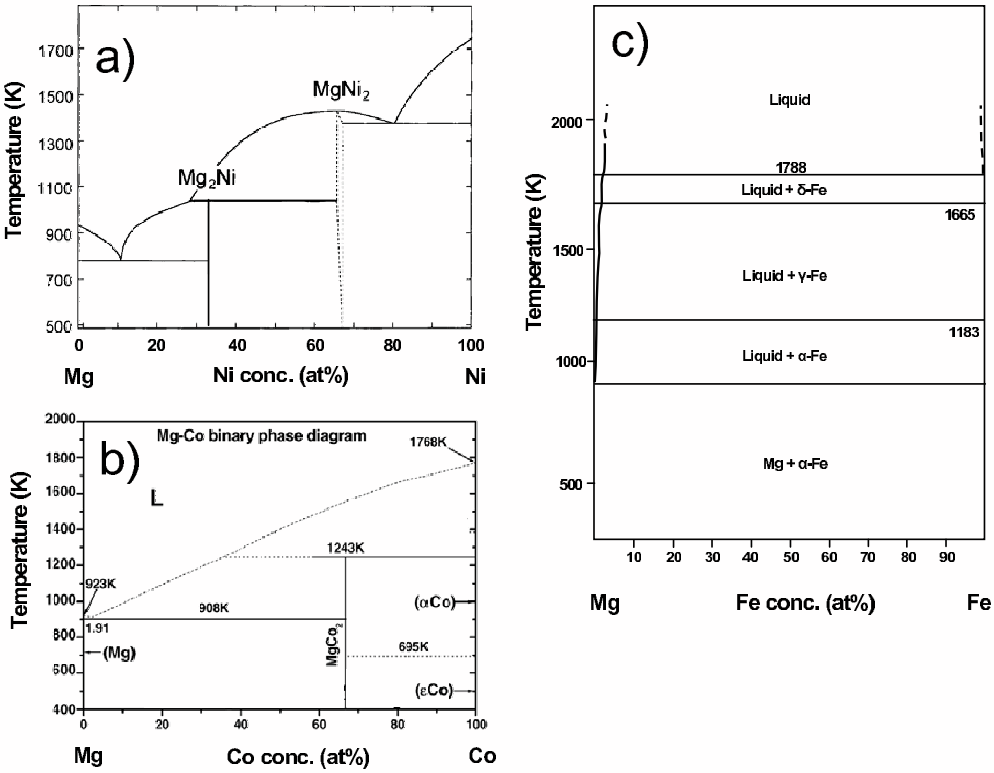

Figure 3.1: Temperature-composition metal phase diagrams of the binary systems for bulk materials of a) Mg-Ni [21] b) Mg-Co [22], Note, that the MgCo phase is not indicated in the phase diagram here [7, 8] and c) Mg-Fe [23]. Only for TM=Ni does a binary Mg-TM parent alloy exist with the same composition as in the ternary Mg_2TMH_x. For TM=Co two binary alloys exist with a different composition compared to the ternary alloy. The Mg-Fe system does not exhibit binary alloys.

Apart from considering Mg_yTMH_x (TM=Ni, Co, Fe) as possible solar absorbers in an all-solid-state device, these hydrides have been regarded as light-weight hydrogen storage materials. The hydrogen-to-metal weight ratio of Mg_2NiH_4, Mg_2CoH_5 and Mg_2FeH_6 is 3.6 wt %, 4.5 wt % and 5.4 wt % respectively, approaching the 6.5 wt % set as a goal by the U.S. Department of Energy (DOE). Especially when the ternary alloys are alloyed with MgH_2 (7.6 wt %), this goal can be approached even better. The volumetric H_2 density of Mg_2NiH_4, Mg_2CoH_5 and Mg_2FeH_6 is 1.0 x 10^2 kgH_2m^{-3} [26], 1.3 x 10^2 kgH_2m^{-3} [9] and 1.5 x 10^2 kgH_2m^{-3} [26], respec-

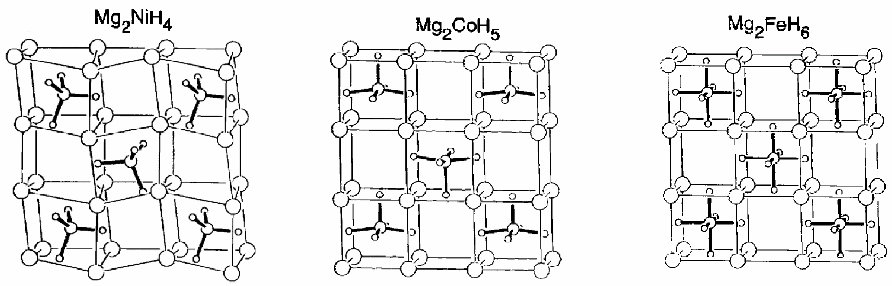

Figure 3.2: Crystal structure determined for bulk material of a) the low temperature phase of Mg_2NiH_4, b) tetragonal Mg_2CoH_5 and c) Mg_2FeH_6. TMH_x complexes are indicated by thick lines, Mg-Mg contacts by thin lines, Mg atoms are indicated by large circles, and H^- atoms by small circles [24, 25].

tively, i.e. much higher than that of liquid hydrogen (71 kgH_2m^{-3}). The thermodynamic condition for an ideal hydrogen storage material (1 bar hydrogen equilibrium pressure at room temperature) corresponds to a heat of formation of $\Delta H \cong -19$ kJ/mol of H [27]. This implies that Mg_2NiH_4 ($\Delta H \approx -32$ kJ/mol of H) [19], Mg_2CoH_5 ($\Delta H \approx$ -41 kJ/mol of H) [10, 11, 28], Mg_2FeH_6 ($\Delta H \approx$ -49 kJ/mol of H) [29], and MgH_2 ($\Delta H \approx$ -37 kJ/mol of H) [30–32] are all too stable. Note, that due to kinetic barriers the conditions for (de-)hydrogenation are even worse than expected on a thermodynamic basis [33].

A comparison of the optical properties of the Mg_2TMH_x-compounds during hydrogenation allows us to get a better insight in the nature of the hydrogen absorption process. Moreover, it enables us to compare their optical properties and evaluate their possible use in switchable devices.

This chapter is structured as follows. After a short description of the sample preparation and the characterization techniques used, we review the hydrogenation behavior of the Mg-Ni system and present the results of the Mg-Co and Mg-Fe systems. Then we compare the optical properties of their hydride states. We examine the contrast between the as-prepared and hydrogenated state for the different TM-hydrides and at various Mg-to-TM ratios. Furthermore, the existence of a black state due to a double layer formation and its dependence on different TM-hydrides, Mg-to-TM ratios and the number of hydrogenation cycles is investigated. These differences are then related to the nature of the phase formation process and the microstructure of the films.

3.2 Experimental

3.2.1 Preparation and characterization

Samples of 200 nm Mg_yTM thin films are co-sputtered from Mg and TM targets in a AJA sputter system with a base pressure of $\sim 10^{-8}$ mbar. The quartz (suprasil1) and CaF_2 substrates are kept at room temperature during deposition. A Pd layer of 5-10 nm is sputtered on top of the films to prevent oxidation and enhance hydrogen uptake. We use Rutherford backscattering spectrometry (RBS) to estimate the thickness and the composition of the films. For these films we use carbon substrates to minimize the substrate signal in the RBS measurement. A small oxygen contamination is observed only at the film surface and at the substrate-film interface which has increased after two hydrogenation cycles up to a maximum of the oxygen-to-metal concentration of [O]/[M]= 0.03. The enhanced oxygen content is presumably due to released oxygen from the carbon substrate upon heating. Pd-Mg_yTM intermixing is found to be negligible. During hydrogen loading the optical measurements are performed at near normal incidence (15°) from the substrate side in a Bruker IFS 66 Fourier transform spectrometer (0.72 eV-3.5 eV). We measure the reflection from the Pd-side of the sample with a laserdiode ($\hbar\omega$ = 1.95 eV). During hydrogenation the hydrogen pressure is increased stepwise up to 1 bar H_2. We dehydrogenate the samples by exposing them to air and increasing the temperature to 90°C. Additionally, optical properties of the as-prepared and hydride samples are measured in a Perkin Elmer Lambda 900 diffraction grating spectrometer (0.495 eV-6.19 eV). For structural characterization we use X-ray diffraction in a Bruker D8 X-ray diffractometer (Cu-Kα, λ = 1.5418 Å). Secondary Electron Microscopy (SEM) was performed using a Philips FEG XL series xl30s apparatus at a background pressure of 10^{-4} Pa.

To link the hydrogenation measurements of different techniques on samples with the same composition, the DC resistivity is recorded simultaneously in a Van der Pauw configuration [34]. For all Mg_yTMH_x the resistivity increases with increasing hydrogen concentration. Note, however, that there are two complications. Firstly, the measured resistivity of the Mg_yTMH_x with the Pd layer on top is mainly determined by this metallic cap layer, especially when the Mg_yTMH_x is in the hydride state. Graphs plotted as a function of resistivity are therefore compressed at high resistivity values. Secondly, the resistivity development depends on the hydrogenation process. When the nucleation of the hydride starts at the substrate-film interface creating a double layer, the resistivity of the film increases gradually, since it depends mainly on the decreasing metal layer thickness. When the nucleation starts homogeneously through the film, the resistivity initially hardly rises, until the percolation limit is reached. At this point, the resistivity shows a sudden large increase. Thus the development of the resistivity within the Mg_yTM-hydride layer depends on the hydrogenation behavior, which is not a priori known. No correction of the resistivity is applied. Therefore the presented resistivity data are only a qualitative measure of the hydrogen content.

3.2.2 Modelling

In the next paragraph the measured reflection and transmission of the Mg_yTMH_x (TM=Co, Fe) for various compositions are presented and compared together with previously reported Mg_yNiH_x results (see Section 3.3 for an overview of the Mg_2Ni data). However, to get insight in the hydrogenation process and the compounds formed upon exposure to hydrogen, modelling of the optical data is necessary. The dielectric function $\bar{\varepsilon}(\omega) = \varepsilon_1(\omega)+i\varepsilon_2(\omega)$ of the Mg_yTMH_x films in both the metal and the hydride state are estimated and used to model different types of nucleation during the hydrogenation process. Furthermore, the optical properties of the Mg_yTMH_x films are compared with (mixtures of) components of the films, e.g. pure Mg or a mixture of MgH_2 and Mg_2CoH_5.

To accomplish these investigations, several steps are needed. First, the optical properties of a stack of layers need to be described to account for all the different layers involved, e.g. the substrate, the Mg_yTMH_x and the Pd cap layer. Then we simulate the transmission and reflection of our stack with different substitutions for the Mg_yTMH_x layer. Alternatively, we separate the Mg_yTMH_x layer from the measured stack of layers for parametrization of its optical properties for modelling the hydrogenation process. Furthermore, for the description of a layer consisting of a mixture of two materials, an effective dielectric function has to be estimated.

The multiple reflections and refractions of the propagating light wave at the interfaces of the different sublayers in our samples are calculated with a transfer matrix method based on the Fresnel formulae [35, 36]. Normal incidence of the incoming light beam is assumed and the interfaces between the different layers are considered to be flat.

In a non-magnetic solid, the dielectric function is related to the refractive index n and the extinction coefficient k as:

$$\varepsilon_1 = n^2 - k^2 \tag{3.1}$$

$$\varepsilon_2 = 2nk \tag{3.2}$$

For the parametrization of the optical properties of the Mg_yTMH_x films we use the Drude-Lorentz model, since it is consistent with the Kramers-Kronig relations and has been used successfully for comparable materials [19, 20, 37, 38]. The Lorentz model is based on a classical theory in which the motion of the electrons is described as simple harmonic oscillators. It represents the electrons of an insulator being bound to the nucleus as a small mass connected to a large mass by a spring. The results are similar to quantum mechanical treatments in which the model describes the direct interband transitions [39, 40]. The Drude model describes the free electrons in a metal. It is mathematically of the same form as a Lorentz model with the spring constant $\omega_0 = 0$. It invokes, however, the plasma frequency ω_p given by:

$$\omega_p = Ne^2/(\varepsilon_0 m) \tag{3.3}$$

where N is the density of free electrons, ε_0 is the permitivity of free space, and the free election relaxation time $\tau = 1/\beta$. For the semiconducting phase we have used

one Drude term and four Lorentz oscillators to model the optical response of the free and bound electrons, respectively:

$$\varepsilon_1 = \varepsilon_\infty - \frac{\omega_p^2\tau^2}{1+\omega^2\tau^2} + \sum_{j=1}^{4} f_j \frac{\omega_{0j}^2 - \omega^2}{(\omega_{0j}^2 - \omega^2)^2 + \omega^2\beta_j^2} \tag{3.4}$$

$$\varepsilon_2 = \frac{\omega_p^2}{\omega^2}\frac{\omega\tau}{1+\omega^2\tau^2} + \sum_{j=1}^{4} f_j \frac{\beta\omega}{(\omega_{0j}^2 - \omega^2)^2 + \omega^2\beta_j^2} \tag{3.5}$$

Here, the constant ε_∞ accounts for excitations far above 6.0 eV, ω_p is the plasma frequency, τ is the free electron relaxation time, f is the oscillator strength, ω_0 the resonance frequency and β the broadening parameter.

To describe the dielectric function of a mixture of two phases, e.g. a metal and its hydride, we use the Bruggeman effective medium approximation [41]. The grains, which should be small compared to the wavelength of the light, are assumed to be distributed randomly. In this model the complex dielectric function $<\varepsilon>$ of the effective medium is implicitly given by:

$$f_A \frac{\varepsilon_A - <\varepsilon>}{L\varepsilon_A + (1-L)<\varepsilon>} + f_B \frac{\varepsilon_B - <\varepsilon>}{L\varepsilon_B + (1-L)<\varepsilon>} = 0 \tag{3.6}$$

where ε_A and ε_B are the complex dielectric functions of material A and B, respectively and f_A and f_B are the volume fractions of material A and material B. We have obviously $f_A + f_B = 1$. The factor L is a geometrical factor and is chosen here to be 0.33, which corresponds to spherical inclusions. The equation gives two solutions, of which only the one with a positive imaginary dielectric function ε_2 is physically relevant.

3.3 Present status of Mg_yNiH_x

The optical properties of Mg_yNiH_x have been studied intensively [1, 5, 17, 19, 42–46]. Richardson *et al.* observed that the optical appearance of Mg_yTMH_x thin films changes reversibly upon hydrogenation [1]. At low hydrogen concentrations the film is metallic reflecting, while at high concentrations it changes to a transparent semiconductor. In between, an absorbing black state is observed with low reflection and negligible transmission over the entire visible region [4]. The optical properties depend on the Mg-Ni ratio.

In the as-prepared metallic state Mg_yNi films of typically 100 nm exhibit a reflection of around 50 %, which increases with increasing Mg-content up to that of pure Mg [48], whereas no transmission is observed. Upon exposure to hydrogen the reflection decreases and the transmission increases. Figure 3.3 shows that the transmission edge shifts to higher energies with increasing Mg-content. At high Mg-concentrations ($y = 10$) the shape of the curve changes and the transmission vanishes at much larger energies, indicating the presence of MgH_2, which has a band gap of 5.6 eV [20].

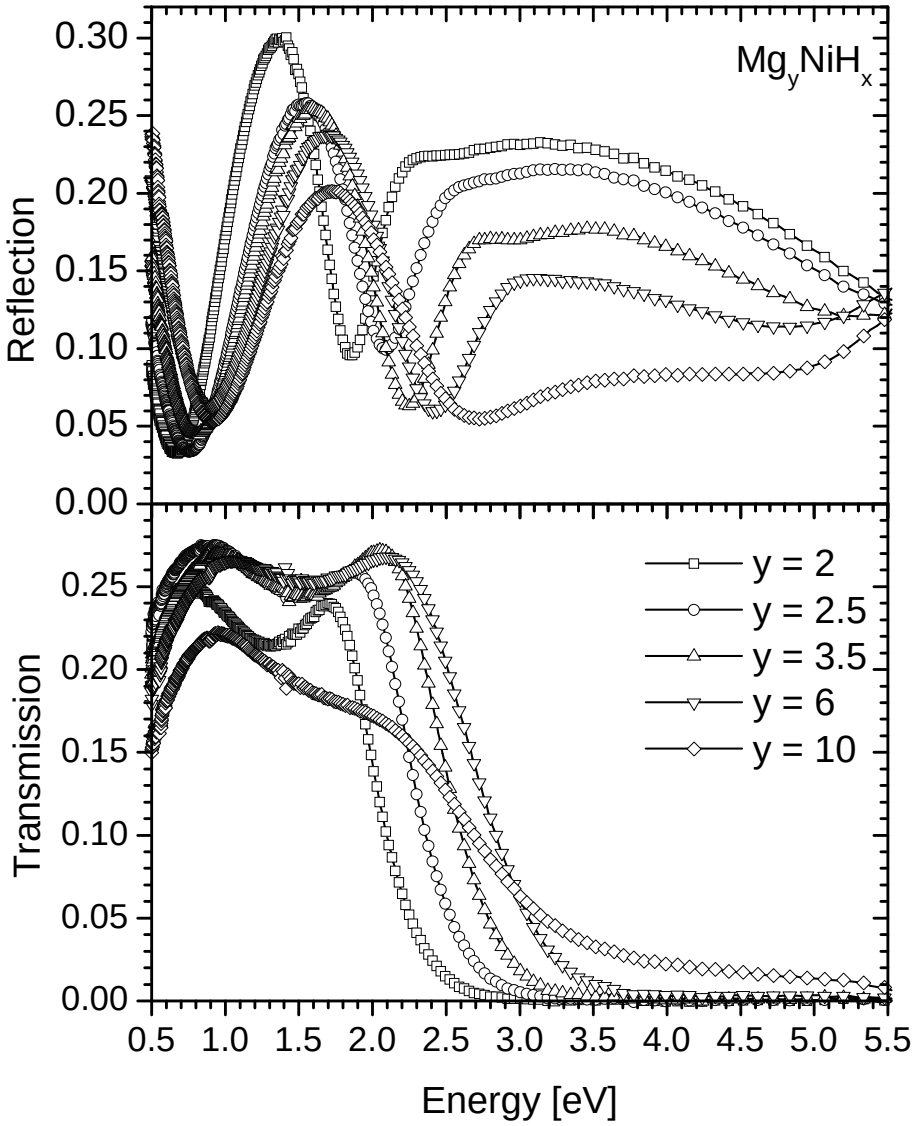

Figure 3.3: Experimental reflection and transmission of Mg_yNiH_x with $y = 2,\ 2.5,\ 3.5,\ 6$ and 10 for a 100-nm thick Mg_yNi film covered by 10 nm Pd after hydrogenation at 1 bar H_2 at 80°C [47].

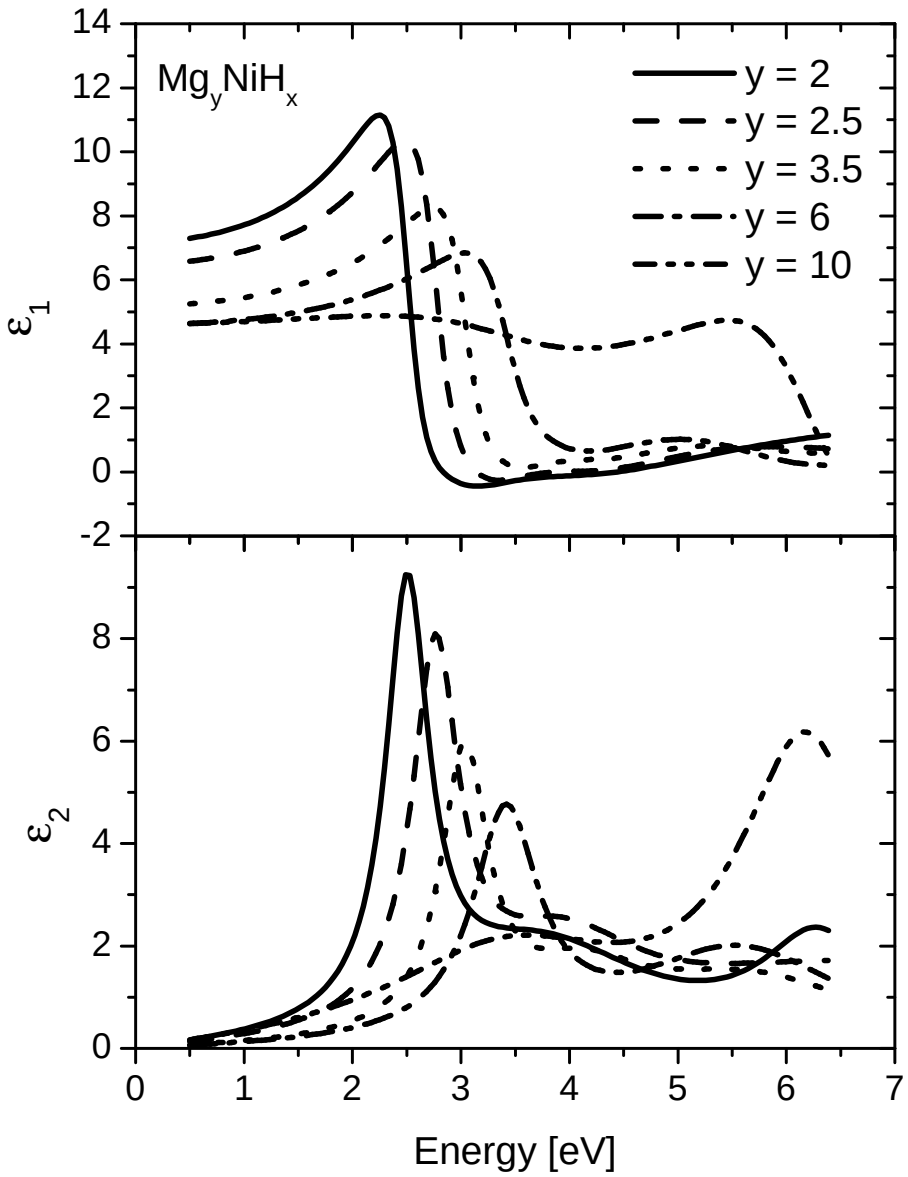

Figure 3.4: Fitted real ε_1 and imaginary ε_2 part of the dielectric functions of Mg_yNiH_x with $y = 2,\ 2.5,\ 3.5,\ 6$ and 10 [47].

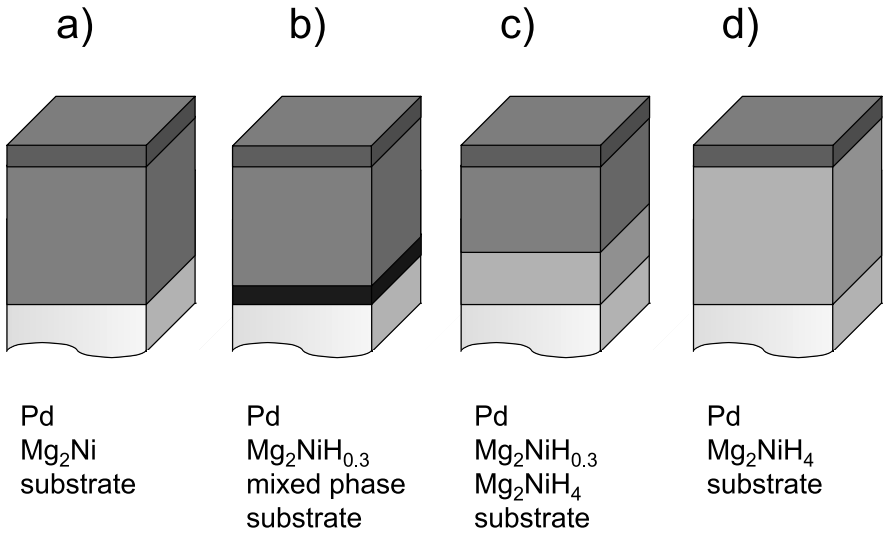

Figure 3.5: Schematic representation of the hydrogenation process of Mg_2Ni covered with Pd (a). Mg_2Ni absorbs hydrogen up to a concentration of $Mg_2NiH_{0.3}$. b) The nucleation of Mg_2NiH_4 starts in a thin layer at the substrate-film interface. c) When this ∼30-nm thick layer is completely converted into Mg_2NiH_4 the hydrogenated layer starts to grow at the expense of the metallic layer towards the Pd top layer. This means that the hydrogenation process causes a self-organized double layering. d) Finally, the entire layer is hydrogenated.

Lohstroh *et al.* [47] fitted the dielectric function of Mg_yNiH_x for various Mg-concentrations, as shown in Figure 3.4. The imaginary part of the dielectric function of Mg_yNi with $y = 2$ displays a strong peak just above the band gap (1.90 eV), which shifts to higher energies with increasing Mg-content. Lohstroh *et al.* points out that the dielectric function of a mixture of Mg_2NiH_x with MgH_2 obtained by the Bruggeman effective medium approximation (equation 3.6) does not reproduce such a shift. They conclude that the dielectric function cannot simply be described as a mixture of Mg_2NiH_4 and MgH_2, but that an excess of Mg alters the electronic structure of the Mg_2NiH_4 inclusions.

A strongly absorbing state is observed at intermediate hydrogen concentration. This black state is caused by a double layer formation resulting from the nucleation of the hydride in an approximately 30 nm-region at the interface between the film and the substrate [19, 44]. First, the hydrogen dissolves up to a concentration of the solubility limit of $Mg_2NiH_{0.3}$ [6]. Then, the complex hydride starts to form in a ∼30 nm region at the substrate-film interface and grows towards the Pd cap layer as schematically indicated in Fig. 3.5.

Figure 3.6 shows the reflection from the Pd top side (R_{Pd}) and through the transparent substrate (R_{sub}) at $\hbar\omega = 1.95$ eV of Mg_2Ni upon hydrogen loading as

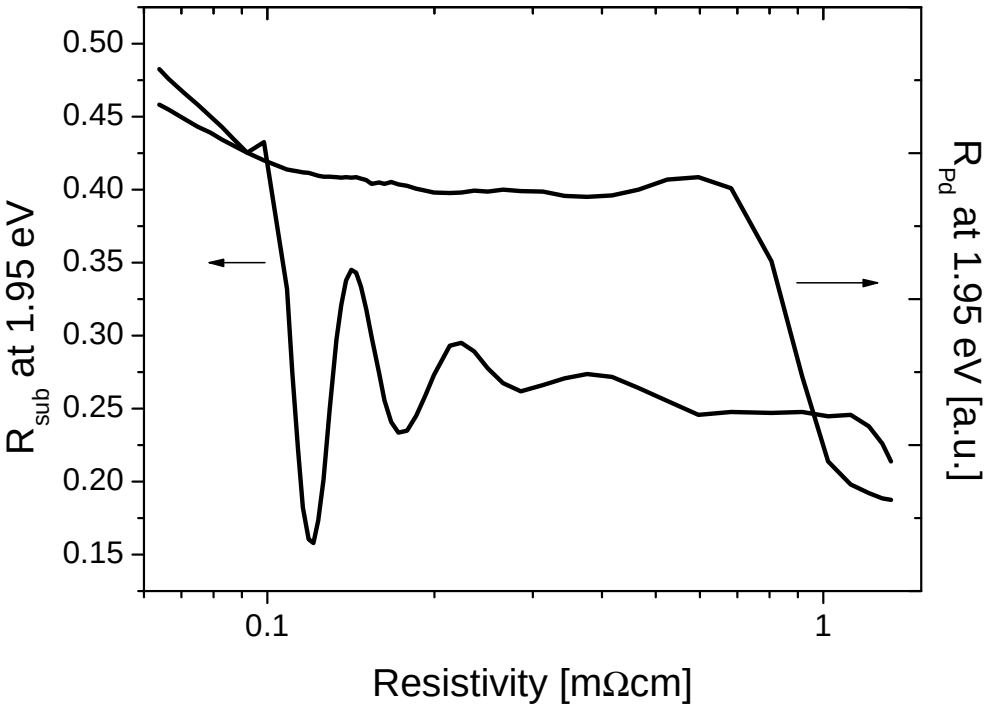

Figure 3.6: Reflection at $\hbar\omega = 1.95$ eV of a 250 nm $Mg_{1.7}Ni$ film with a 7 nm Pd cap layer viewed from the Pd side R_{Pd} and through the substrate R_{sub} during hydrogenation. The hydrogen concentration increases with time and causes an increase in the resistivity. Consequently, the resistivity is a measure for the hydrogen concentration. First, the reflection R_{sub} and R_{Pd} decrease as the metallic Mg_2Ni absorbs hydrogen up to a concentration of $x = 0.3$ [19]. With increasing hydrogen concentration the substrate-side reflection R_{sub} decreases rapidly due to the nucleation of the hydride at the film-substrate interface. Next interference oscillations are observed which disappear when the film approaches its fully hydrogenated state. The difference between R_{Pd} and R_{sub} is a direct consequence of the bilayer nature of the Mg_yNiH_x induced during hydrogenation.

a function of resistivity. First, the reflection at both sides decreases as metallic Mg_2Ni absorbs hydrogen up to a concentration of $x = 0.3$. When more hydrogen is absorbed, the reflection R_{sub} through the substrate decreases sharply due to the nucleation of Mg_2NiH_4 at the film-substrate interface. Then, interference oscillations appear which shift to lower energies as the hydride layer grows. Finally, when the film is almost fully hydrogenated, the Pd-side reflection R_{Pd} decreases. The large difference between R_{Pd} and R_{sub} clearly indicates the bilayering of Mg_2NiH_x during hydrogenation. The interference oscillations moreover suggest that the two layers are separated by a well-defined boundary. Note that due to the small thickness of

the Pd-layer its transmission is high and therefore its contribution to the Pd-side reflection R_{Pd} is relatively low.

The origin of the black state probably lies in the microstructure of the film [49, 50]. The double layer formation is independent of the substrate used and the Mg-Ni ratio is found to be constant throughout the film thickness. The microstructure, however, shows a two-layer structure. The 30 to 50 nm thick layer near the substrate consists of small grains and clusters of small grains, whereas the top has a columnar structure. From these observations it is concluded that the large amount of grain boundaries at the substrate-film interface facilitates the phase transformation process, while the columnar Mg_2Ni structure in the upper fraction of the film allows for fast diffusion kinetics. Therefore, the hydride formation starts at the substrate-film interface creating a self-organized double-layer system.

As some of our films contain a large amount of Mg, it is interesting to compare their hydrogenation behavior with that of pure Mg. Pure Mg-films exhibit also a high optical absorbance. However, MgH_2 is formed homogeneously throughout a 100 nm-thick film upon careful hydrogenation at elevated temperatures. The formation of a hydrogen-blocking MgH_2 layer at the interface between Pd and Mg can be circumvented by starting hydrogenation at relatively low hydrogen pressure [51]. In this case the intermediate high optical absorbance is not due to the interference effect caused by a double layer formation, but due to the coexistence of nano-sized grains of reflecting Mg and transparent MgH_2 [51].

Increasing the Mg-content in the Mg_yNi films results in an increasing MgH_2 character when fully hydrogenated. The transmission becomes higher and the reflection lower at fully hydrogenated state for larger Mg-to-TM ratios. Since the reflection for the metallic Mg_yNi films is higher if more Mg is present, the contrast between the metallic and semiconducting hydride state is increased with increasing Mg-content. Moreover, the optical gap in the hydride state is shifted to higher energies with larger Mg-content.

3.4 Results

We consider now two other Mg-TM hydrides: Mg_yCoH_x and Mg_yFeH_x. Firstly, we investigate the optical properties of the as-prepared and hydride state. Then, we monitor the hydrogenation process to detect whether the hydride nucleates at the substrate-film interface and a double layer is formed. We find that the optical properties and the cycling stability depend on the Mg-to-TM ratio and on the transition metal used. Finally, we argue that the observed differences in hydrogenation behavior of the Mg_yTM thin films are caused by the presence of Mg clusters, serving as random nucleation sites for hydrogenation. We investigate the hydride state for three reasons, namely: to examine the intrinsic properties of Mg_yTMH_x (TM=Co, Fe), to determine the optical properties for modelling the black state and to understand the phase formation process on hydrogen loading.

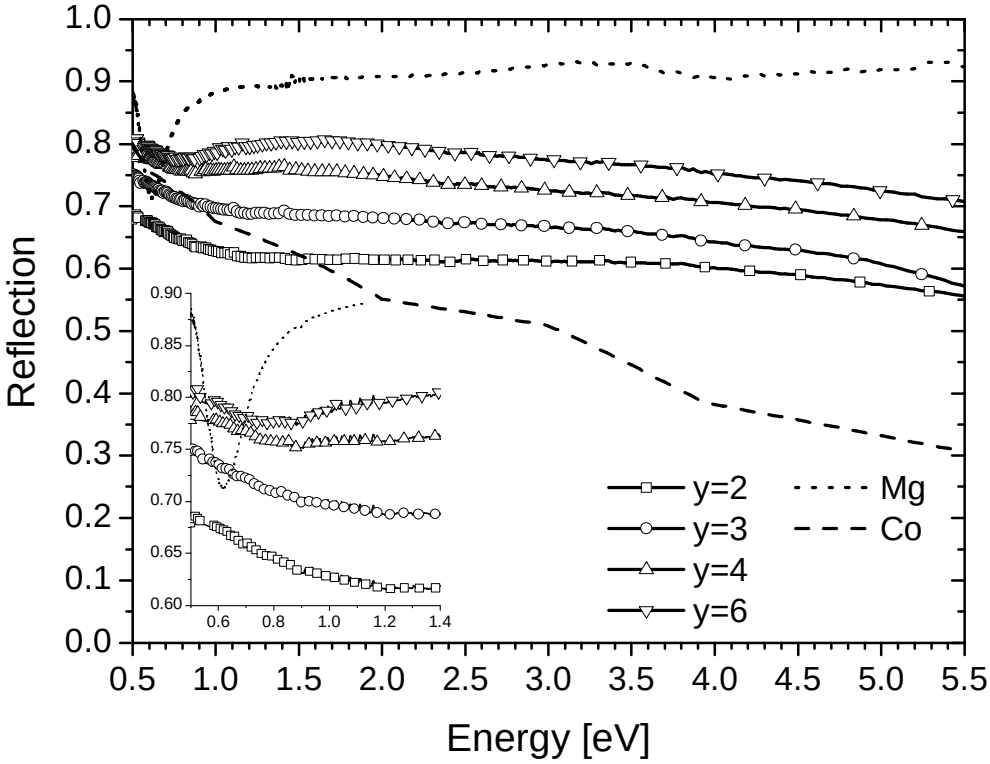

Figure 3.7: Measured reflection R_{sub} viewed through the substrate of the as-prepared samples of 200 nm Mg_yCo with $y = 2,\ 3,\ 4,\ 6$ on quartz and covered with 10 nm Pd. The reflection of pure Mg and Co films on quartz substrate covered with Pd are added indicating the two extreme cases of pure Mg and Co [52]. With increasing Mg content we observe an overall increase of the reflection. The insert shows a magnification of the low energy part of the curves.

3.4.1 Optical properties of as-prepared films

We investigate the as-prepared films to be able to compare the contrast between the as-prepared and the hydride state in the various Mg_yTM-films. Figure 3.7 and 3.8 show the measured reflection R_{sub} viewed through the substrate of the as-prepared samples of 200 nm metallic Mg_yTM (TM=Co, Fe) on quartz and covered by 10 nm Pd. The curves of the reflection of a pure Mg and a pure TM layer on a quartz substrate and capped by Pd are added. The reflection of pure Mg is approximately 90% over the whole energy range considered, while the reflection of pure Co decreases from 80 % at 0.5 eV to 30 % at 6.0 eV [52] and the reflection of pure Fe decreases from 85 % at 0.5 eV to 30 % at 6.0 eV [52]. The reflection of the as-prepared Mg_yTM films ($y = 2,\ 3,\ 4,\ 6$) roughly fall between the curves of the pure Mg and TM. For Mg_yFe

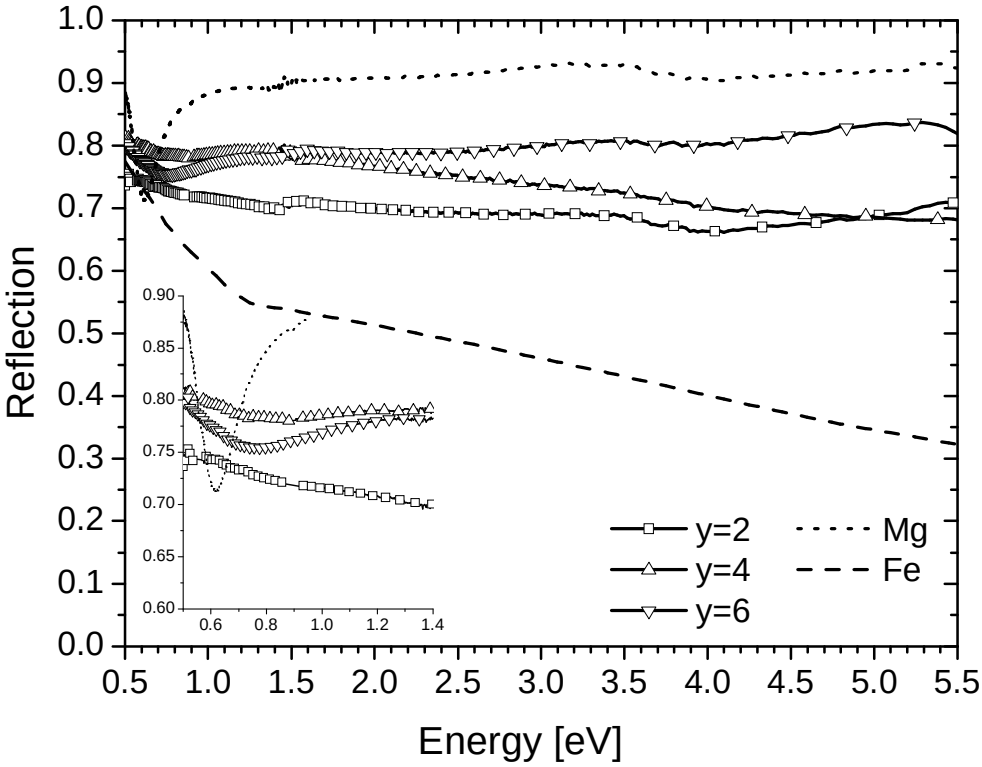

Figure 3.8: Measured reflection R_{sub} viewed through the substrate of the as-prepared samples of 200 nm Mg_yFe with $y = 2,\ 4,\ 6$ on quartz and covered with 10 nm Pd. The reflection of pure Mg and Fe films on quartz substrate covered with Pd are added indicating the two extreme cases of pure Mg and Fe [52]. With increasing Mg content we observe an overall increase of the reflection. The insert shows a magnification of the low energy site part of the curves.

($R = 70\%$ at 1.95 eV for $y = 2$) the reflection is higher than for Mg_yCo ($R = 61\%$ at 1.95 eV for $y = 2$), which in turn is higher than for Mg_yNi ($R = 55\%$ at 1.95 eV for $y = 2$). Only at high Mg-concentrations ($y = 6$) the characteristic dip of Mg around 0.6 eV, which is due to interband transitions, is observed, although shifted to slightly higher energies (see insert of Figure 3.7 and 3.8); i.e. the Mg-character becomes more pronounced at higher Mg-concentrations, as has been observed for Mg_yNi [53]. In the metallic state, none of the films are transparent.

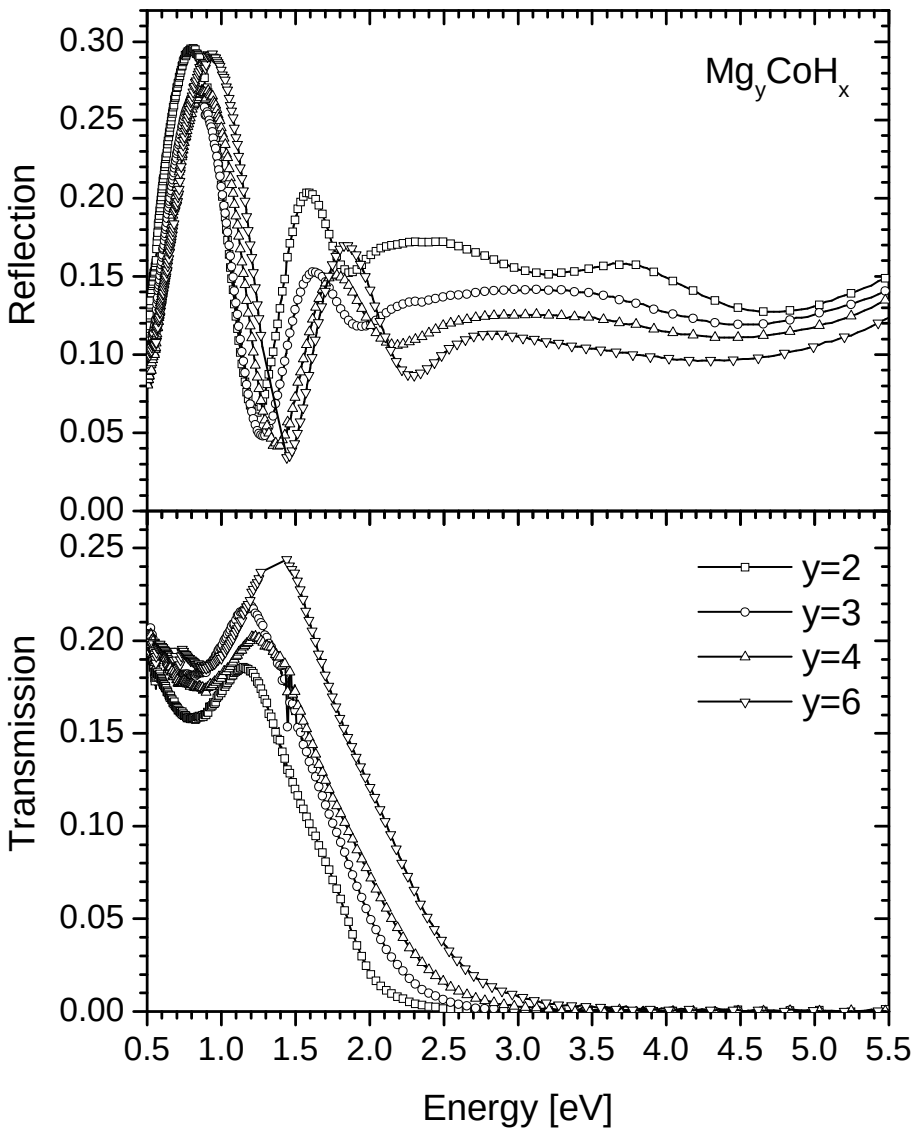

Figure 3.9: Experimental reflection viewed through the substrate and transmission of Mg_yCoH_x with $y = 2,\ 3,\ 4,\ 6$ for a 200-nm thick fully hydrogenated Mg_yCo film covered by 10 nm Pd on a quartz substrate.

sample	Mg_2CoH_x	Mg_3CoH_x	Mg_4CoH_x	Mg_6CoH_x
ε_∞	2.92	2.71	1.78	2.64
$\sqrt{f_1}$	2.17	0.733	1.79	2.13
ω_{01}	2.29	2.32	2.61	2.80
β_1	9.76	0.417	8.69	1.24
$\sqrt{f_2}$	3.05	5.85	1.70	3.65
ω_{02}	2.47	3.49	2.63	3.82
β_2	0.96	2.57	1.15	2.16
$\sqrt{f_3}$	5.20	5.96	4.22	7.72
ω_{03}	3.68	5.58	3.62	6.41
β_3	1.88	2.32	2.05	1.89
$\sqrt{f_4}$	5.30	-	9.98	5.24
ω_{04}	5.44	-	6.50	7.34
β_4	1.97	-	3.09	1.64
χ^2	0.0081	0.0388	0.0191	0.0164
Thickness	215	220	219	211

Table 3.1: Drude-Lorentz parameters of the Mg_yCoH_x samples. All parameters are in eV except ε_∞ and χ^2. χ^2 is a measure for the difference between the model and the measured data. The thickness is given in nm.

3.4.2 Optical properties of hydrogenated films

The reflection and transmission of the hydrogenated Mg_yCoH_x films are plotted in Fig. 3.9. These samples were hydrogenated at ∼10 bar at 90°C for more than one week to ensure a fully hydrogenated state. Clearly, the optical properties of these hydrogenated films depend on the Mg-to-Co ratio. At high energies, in the interference-free region, the reflection decreases with increasing Mg-content. Since in the as-prepared state the opposite is observed, the contrast in reflection between the as-prepared and the fully hydrogenated state increases with increasing Mg-to-Co ratio.

The higher the Mg-content the higher the transmission in the hydride state (see Figure 3.9). The transmission goes up to 24 % at the highest Mg-content at low energies. Furthermore, the transmission edge extends to higher energies upon increasing Mg-to-TM ratio. Although this might be due to the presence of MgH_2, the increase and shift are not as high as expected based on the model of the mixtures of MgH_2 and Mg_2CoH_5. Since metallic Mg lowers both the transmission and the energy of the transmission edge, we assume that not all excess Mg has been transformed into MgH_2. For Mg_yCoH_x films with $y = 4$ and $y = 6$ the maximum intensity of the transmission increases with the number of hydrogen loading cycle when exposed to 1 bar H_2 for one day. This is a first indication that these films change between subsequent hydrogenation cycles; i.e. that a larger amount of material has switched.

The dielectric function for the Mg_yCoH_x samples is fitted by using the Drude-

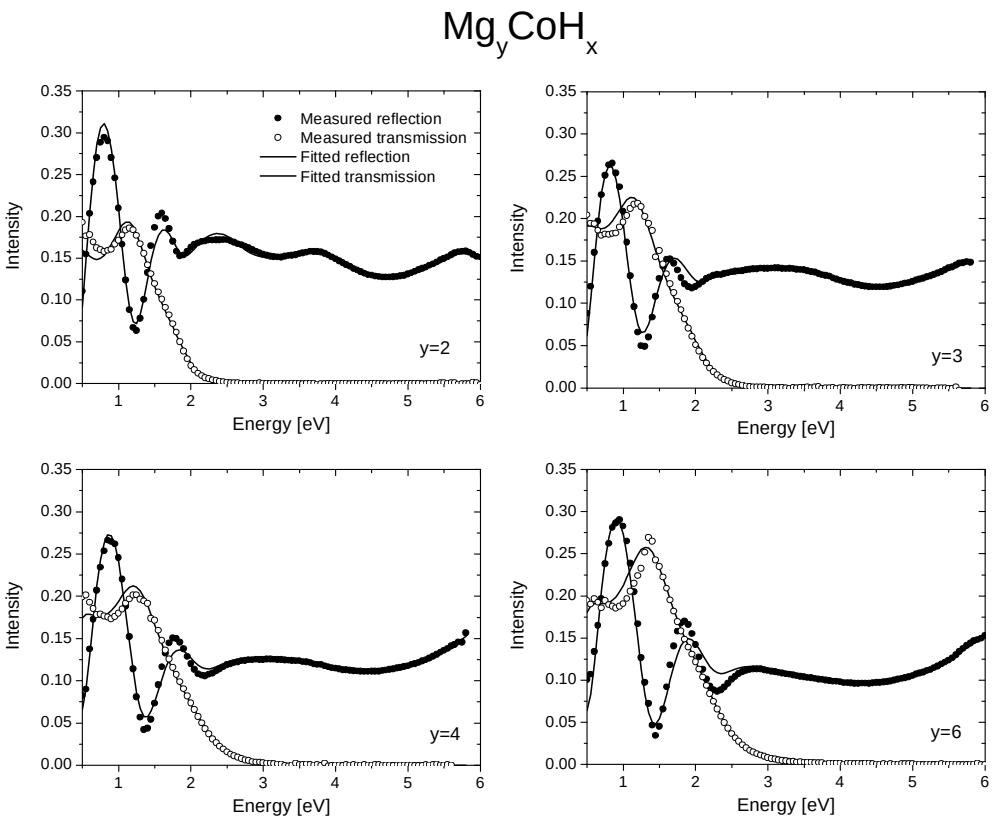

Figure 3.10: Experimental and fitted reflection viewed through the substrate and transmission of fully hydrogenated Mg_yCoH_x with $y = 2,\ 3,\ 4,\ 6$ for a 200-nm thick Mg_yCo film covered by 10 nm Pd on a quartz substrate. Modelling with 4 Lorentz oscillators gives a reasonably good fit.

Lorentz parametrization given in equations 3.4 and 3.5. The plasma frequency ω_p is set zero, since no free electrons are assumed to be present. As can be seen from Fig. 3.10, the measured reflection and transmission curves are well fitted using four Lorentz oscillators. The results of the fitted dielectric functions are shown in Table 3.1 and plotted in Fig. 3.11. Note that the Lorentz parameters should not be seen as the only solution to represent ϵ_1 and ϵ_2. Other parametrizations of the dielectric function in the considered energy range are possible. These parameters are presented here, since they will be used for modelling the black state in the following section. The fitted dielectric functions of Mg_yCoH_x are plotted along with the modelled dielectric functions of a Bruggeman effective medium approximation described by equation 3.6 of a mixture of Co and MgH_2 (see Fig. 3.11). Clearly, the

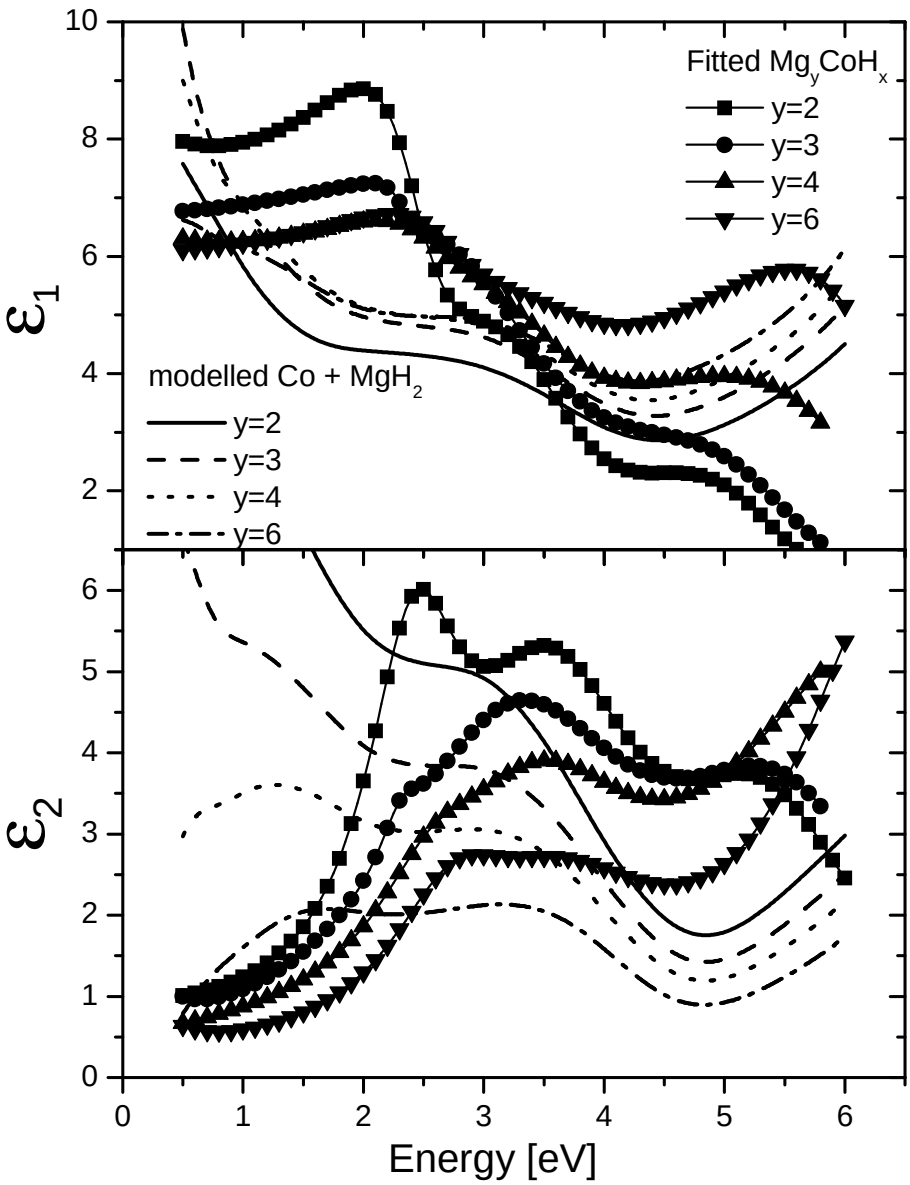

Figure 3.11: Fitted real and imaginary parts of the dielectric function of Mg_yCoH_x with $y = 2,\ 3,\ 4,\ 6$ together with the modelled dielectric function of Co and MgH_2 for several Co-to-MgH_2 ratios calculated by the Bruggeman effective medium approximation. The dielectric functions are clearly not a combination of Co and MgH_2, indicating that Co is involved in the hydrogenation process. Probably, Mg_2CoH_5 is formed.

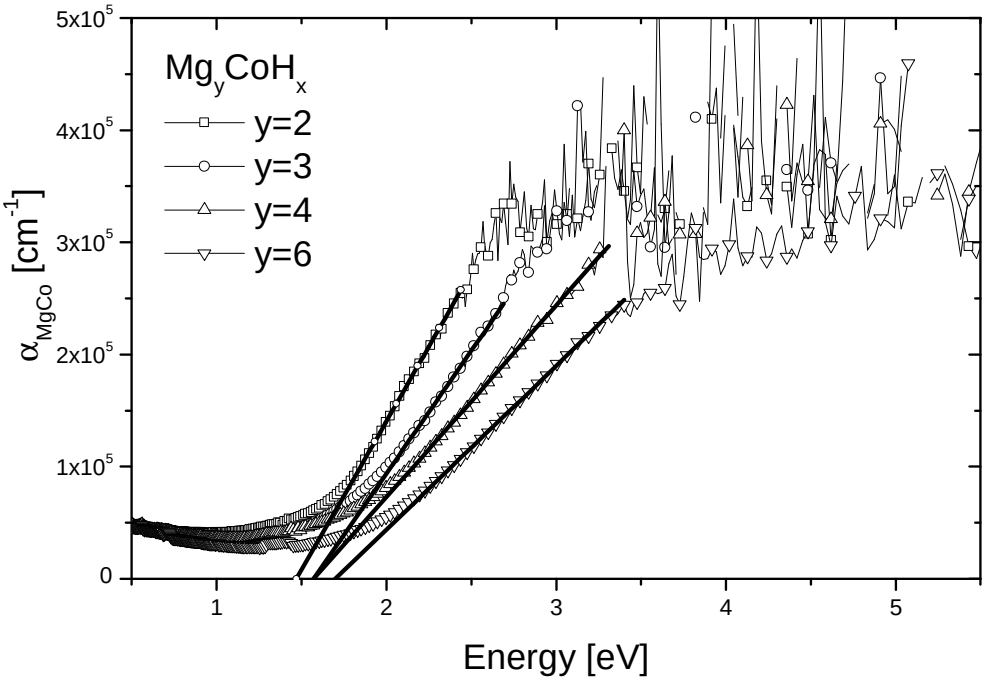

Figure 3.12: Absorption coefficient α_{MgCo} of the hydrogenated Mg_yCoH_x ($y = 2,\ 3,\ 4,\ 6$).

optical properties of the measured reflection and transmission cannot be described by such a mixture. The peak at 2.5 eV for $y = 2$ and the already smaller one for $y = 3$ indicate absorption by Mg_2CoH_5, whereas the peak at 6 eV in $y = 4$ and $y = 6$ show the presence of MgH_2. The peak at around 3.4 eV possibly indicates the existence of $Mg_6Co_2H_{11}$, since it is highest for $y = 3$.

We estimate the optical band gap by plotting the absorption coefficient as a function of photon energy. The absorption coefficient α_{MgTM}, corrected for the Pd top layer, is obtained from:

$$\alpha_{MgTM} = -\frac{1}{t_{film}}[\ln \frac{T}{1-R} + \alpha_{Pd} t_{Pd}] \tag{3.7}$$

Here, t_{film} and t_{Pd} is the thickness of the Mg_yTMH_x film and the Pd top layer, respectively. α_{Pd} is the absorption coefficient of Pd, taken from [52], ω is the frequency and c the speed of light. Plotting the absorption coefficient as a function of energy of the hydrogenated Mg_yCoH_x (see Fig. 3.12) indicates a band gap of $E_g \approx$1.5 eV for $y = 2$, $E_g \approx$1.6 eV for $y = 3,\ 4$ and $E_g \approx$1.7 eV for $y = 6$ when extrapolating the slope to zero. The optical band gap is lower than the previously reported gap of bulk Mg_2CoH_5 ($E_g \approx$2.0 eV [14]) and increases with increasing Mg-to-TM ratio.

At low energies the absorption coefficient does not go to zero indicating impurities. The slope of the absorption coefficient becomes more flat with increasing Mg-to-TM ratio, which could indicate some remaining metal phase. Note, that usually the slope of the absorption coefficient α provides information on the nature of the band gap. However, in our case both the nanocrystalline structure and the metal impurities left will dominate the observed slope [54].

For the Mg-Fe system even flatter slopes are observed. Again, the apparent band gap shifts to higher energies with increasing Mg-content as has been observed for the Mg-Ni [47] and Mg-Co systems.

In Figure 3.13 the reflection and transmission spectra in the infrared regime are shown for a 500-nm thick Mg_yTM (TM=Co, Fe) with $y = 2$ hydrogenated at room temperature in 1 bar H_2 for four days. At 0.19 eV (1530 cm^{-1}) and 0.20 eV (1610 cm^{-1}) vibrations of Mg_2CoH_5 [2, 55] and Mg_2FeH_6 [2, 29, 56] are observed, respectively. We find that the absorption bands are more pronounced at lower Mg-to-TM ratios; i.e. the more Co is present, the higher the Mg_2CoH_5 absorption band intensity. The Mg_yTMH_x ($y = 2$) film with TM=Co has a broader absorption band than the Mg_yTMH_x ($y = 2$) with TM=Fe. This is probably due to the difference in Co-H bond length between the basal (1.52 Å) and the apical bond (1.59 Å) [10], whereas the Mg_2FeH_6 has a more symmetrical [FeH_6] complex with a bond length of 1.56 Å [29]. The absorption band of Mg_2FeH_5 is less pronounced than the one of Mg_2CoH_5 which could indicate less Mg_2TMH_x formation. The Mg_2FeH_6 band is observed at higher energies, possibly due to the higher oxidation state of the Fe^{+2} as compared to the Co^{+1} [57].

3.4.3 Optical properties as a function of hydrogen concentration

Lohstroh *et al.* have shown that the optical appearance of the Mg_yNi-thin films during hydrogenation, cannot be explained if they remain homogeneous [44]. This follows qualitatively from the fact that the reflection, R, and transmission, T, of a thick film are given by:

$$R = \frac{(n - n_0)^2 + k^2}{(n + n_0)^2 + k^2} \tag{3.8}$$

$$T = e^{-2(\omega k d/c)} \tag{3.9}$$

Here, n and n_0 are the reflection index of the film and the transparent substrate respectively, k is the extinction coefficient, d is the thickness of the thick film, and c and ω are the velocity and frequency of the incoming light, respectively. This means that for a homogeneous, thick layer with thickness d and $T < 0.001$, a minimum k-value can be derived, which in turn implies a minimum value for the reflection. However, for some of the Mg_yTM films a reflection is observed which is clearly lower than expected on the basis of the observed transmission. This qualitative argument can be put on a firm quantitative basis. By using the transfer matrix method based on Fresnel's formulae for a homogeneous film on a quartz substrate

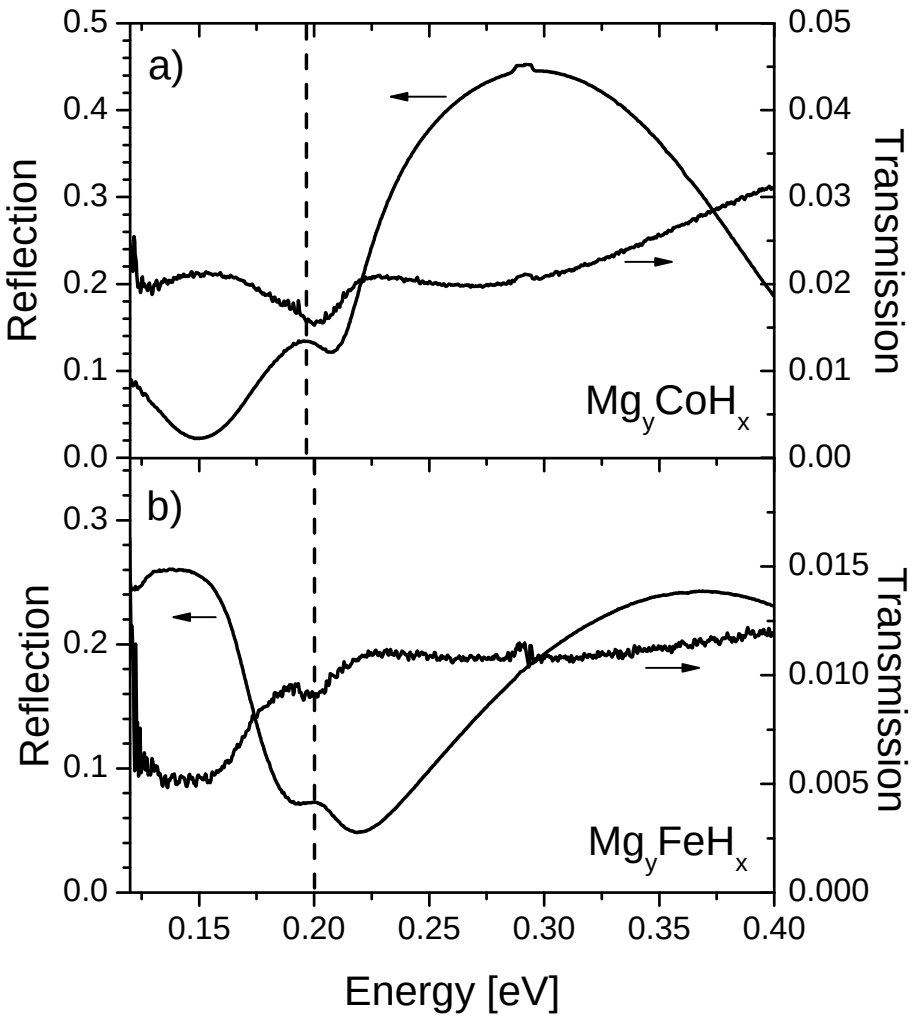

Figure 3.13: Reflection and transmission spectra in the infrared of a 500 nm hydrogenated Mg_yTMH_x film with $y = 2$ capped with 20 nm Pd. a) TM=Co. At 0.19 eV (1530 cm^{-1}) the absorption band of Mg_2CoH_5 is observed. b) TM=Fe. At 0.20 eV (1610 cm^{-1}) the absorption band of Mg_2FeH_6 is observed. From this figure we conclude that the Mg_2TM (TM=Co, Fe) hydrides are formed.

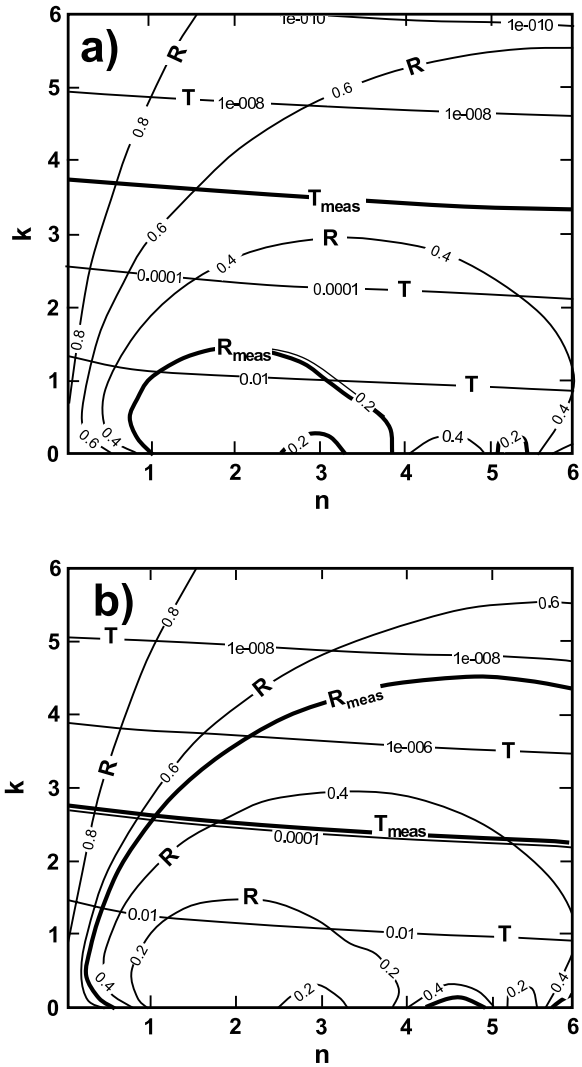

Figure 3.14: Contour map of the reflection through the substrate and transmission at $\hbar\omega = 1.95$ eV calculated for a) a 184 nm thick film on quartz covered by 8 nm Pd (thin lines) and compared with the measured reflection and transmission of a 184 nm thick Mg_yCoH_x film with $y = 2$ (thick lines) and b) a 180 nm thick film on quartz covered by 5 nm Pd (thin lines) and compared with the measured reflection and transmission of a 180 nm thick Mg_yFeH_x film with $y = 2$ during hydrogenation (thick lines). For the Mg_yCoH_x ($y = 2$) no (n,k)-couple exists describing both the measured reflection and transmission. This indicates that during hydrogenation the Mg-Co system must undergo bilayering during hydrogenation. This is similar to the situation in the Mg-Ni system. The contours of the Mg-Fe system cross, showing that for this system the dielectric function of the entire layer can be determined.

covered by Pd, the exact solution of the reflection and transmission on a (n, k)-grid can be estimated. The contour map at $\hbar\omega = 1.95$ eV in Figure 3.14a shows that the measured reflection and transmission values of Mg_yCoH_x with $y = 2$ measured in an intermediate hydrogenation state, do not cross; i.e. there is no set of n and k that describes for both the measured reflection and the measured transmission, hence it is not possible to describe these Mg_yCoH_x films as a single homogeneous layer. Figure 3.14b shows that for Mg_yFeH_x with $y = 2$ such a $n-k$ set does however exist and therefore the Mg_yFeH_x thin film with $y = 2$ can be described by a dielectric function of a single layer. We find that the transient optical behavior depends on the TM, the Mg-TM ratio and the number of hydrogen loading cycles.

During hydrogenation we measure the reflection at $\hbar\omega = 1.95$ eV of Mg_yTM thin films ($y = 2,\ 4,\ 6$) from the Pd capped side of the film R_{Pd} and through the transparent substrate R_{sub}. Figure 3.15 shows the reflection at both sides of Mg_yCoH_x ($y = 2,\ 4,\ 6$) at $\hbar\omega = 1.95$ eV during the first three hydrogen loading cycles as a function of the resistivity, which is a measure of the amount of hydrogen in the film. For $y = 2$ the reflection measured from the Pd top side R_{Pd} stays constant, before a sharp decrease is observed at higher resistivity values. The reflection R_{sub} through the substrate, however, decreases sharply immediately and shows one dip. Successive hydrogen loading cycles show approximately the same hydrogenation behavior as the first. For $y = 4$ R_{Pd} stays constant until the resistivity is $\rho \cong 0.2\ m\Omega$cm and the R_{Pd} starts to decrease slowly while the R_{sub} stays relatively constant. At the same time, at a constant hydrogen pressure, the resistivity starts to increase faster, as can be seen from Fig. 3.16. Furthermore, a difference is observed between the first and following hydrogen loading cycles. R_{Pd} starts to decrease at higher resistivity values and R_{sub} shows additional oscillations as compared to the first hydrogen loading cycle. The resistivity after the first hydrogen loading cycle does not go back to the as-prepared value, whereas the reflection does. Note, the logarithmic scale, which blows up this difference. For $y = 6$ the difference between the first and following hydrogenation cycles is even larger than for $y = 4$. The second hydrogen loading exhibits more pronounced oscillations.

To check whether the difference between the first and following hydrogen loading cycles for Mg_yCoH_x with $y = 4,\ 6$ is caused by the switching itself or by the elevated temperature (typically 75°C) used in the dehydrogenation procedure, a Mg_yCo ($y = 4$) film is annealed before the first hydrogen loading cycle and an identical sample is dehydrogenated at room temperature. The first shows a hydrogen loading behavior which is normally seen for as-prepared samples, while for the second sample the hydrogen loading behavior in the second cycle is changed in the same way as in Figure 3.15. Obviously, the change in hydrogenation behavior is caused by the hydrogen loading itself and not by the annealing during dehydrogenation.

For the Mg_yFe samples the first hydrogen loading cycle shows a gradual decrease in the reflection through the substrate R_{sub}. For $y = 4$ the reflection measured from the Pd-side (R_{Pd}) at $\hbar\omega = 1.95$ eV shows a gradual decrease. In contrast to the Mg-Co system, the Mg_yFe thin films show a large difference between the first and following hydrogen loading cycles for $y = 2$ (see Fig. 3.17). The films with $y = 4,\ 6$

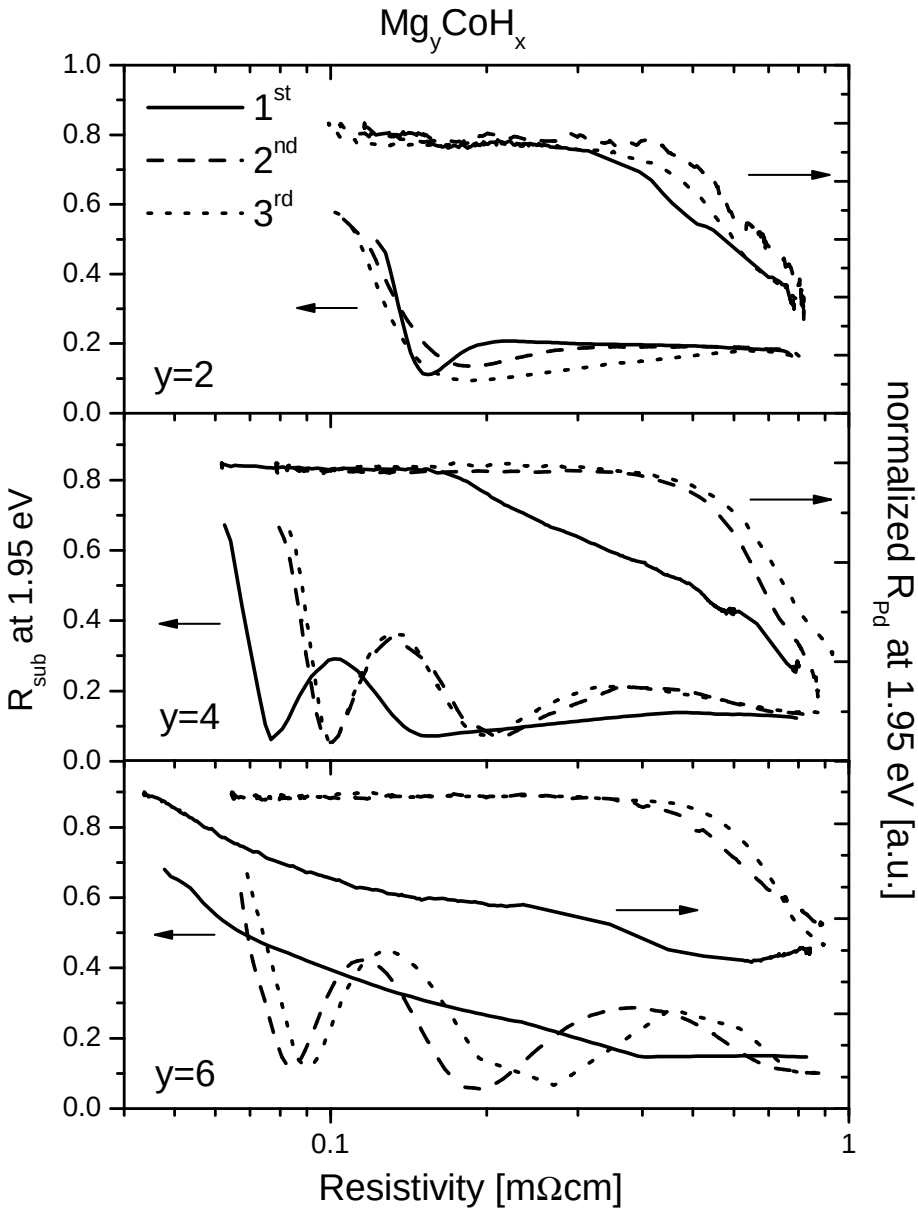

Figure 3.15: Reflection from the Pd top side R_{Pd} and through the transparent substrate R_{sub} at $\hbar\omega = 1.95$ eV of Mg_yCoH_x with $y = 2,\ 4,\ 6$ for the first few hydrogenation cycles. All R_{Pd} are normalized to the starting value of each hydrogen loading cycle. The 200 nm Mg_yCo films are capped with 10 nm Pd.

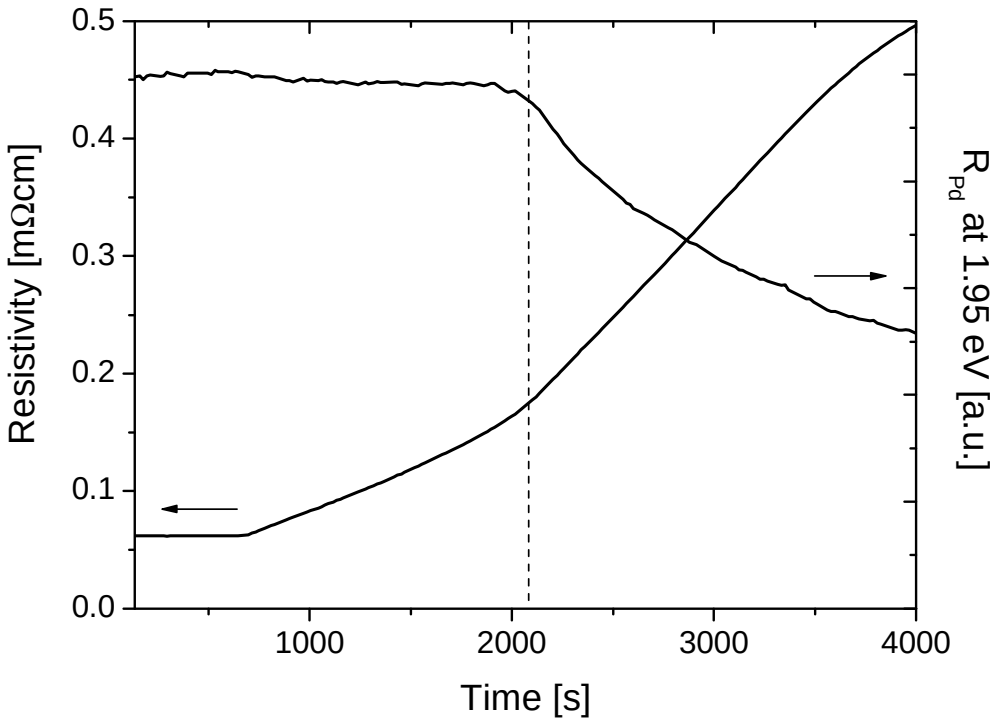

Figure 3.16: Resistivity and reflection R_{Pd} at $\hbar\omega = 1.95$ eV as a function of time for the first hydrogen loading at 5 mbar H_2 of a 200 nm Mg_yCo with $y = 4$ with 10 nm Pd on top. A change in the slope of the resistivity is observed around 2000 s simultaneously with the onset of the decrease of the Pd-side reflection R_{Pd} at constant H_2 pressure. This change of slope indicates the onset of homogeneously dispersed nucleation of Mg_2CoH_5 in the top metallic layer.

could not be dehydrogenated even when exposed to air at 95°C for more than six hours.

We have modelled the hydrogen loading behavior for Mg_yCoH_x films with $y = 2$ (see Figure 3.18-3.20) in three different ways with the method explained in paragraph 3.2.2. The first one (Fig. 3.18) represents the nucleation of the Mg_2CoH_5 phase homogeneously dispersed throughout the entire film. Both the reflection from the Pd top side R_{Pd} as well as through the substrate R_{sub} show a gradual decrease upon hydrogen uptake; the homogeneously distributed hydride-phase affects the reflection from both sides. The second (Fig. 3.19) assumes a double layer formation in which the hydride nucleates at the substrate-film interface and grows at the expense of the metallic top layer. R_{Pd} stays constant until it drops sharply at high hydrogen concentrations, while R_{sub} decreases immediately and shows oscillations while the transparent hydride layer grows in thickness. The third one (Fig. 3.20)

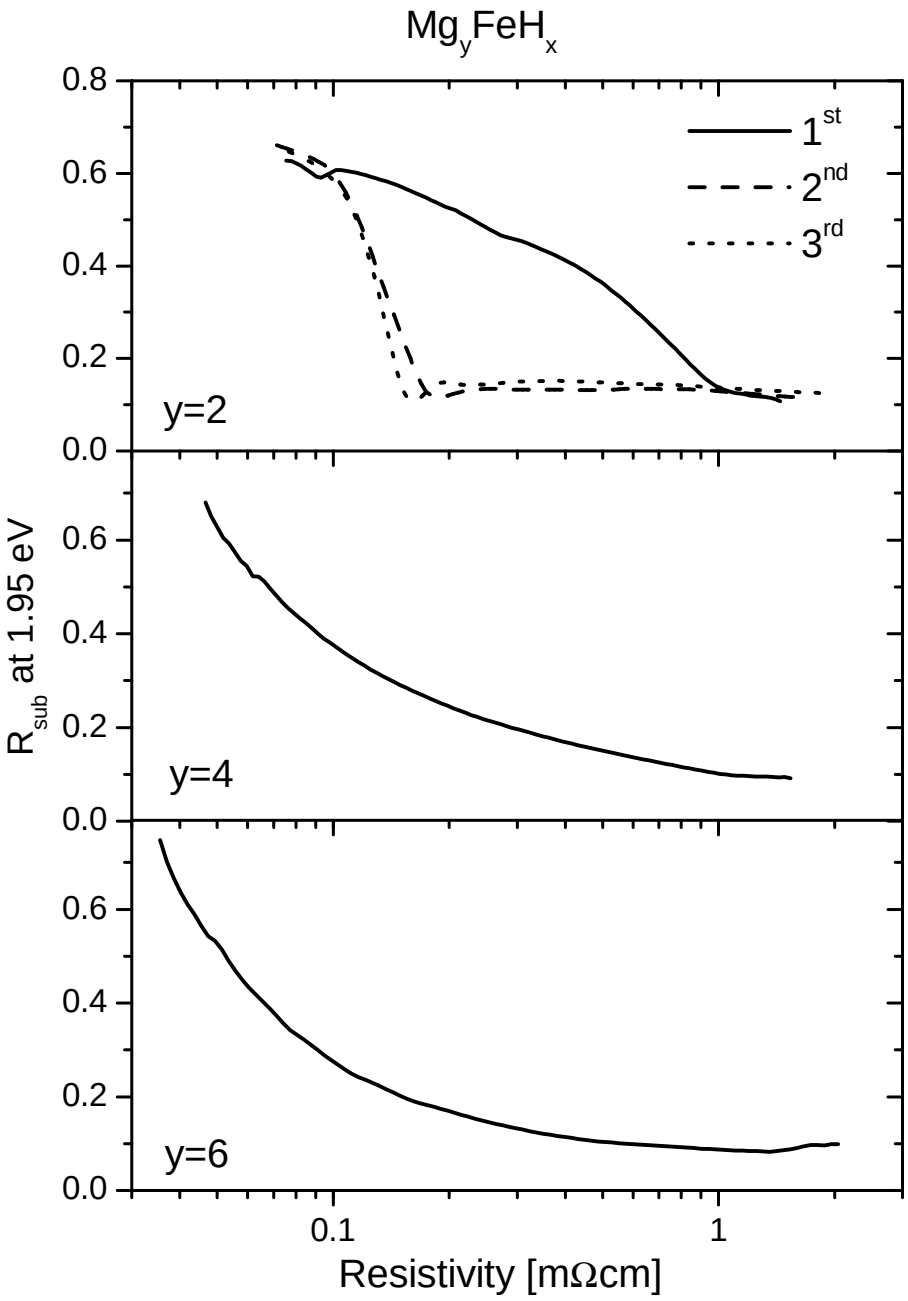

Figure 3.17: Reflection through the substrate R_{sub} at $\hbar\omega = 1.95$ eV of Mg_yFeH_x with $y = 2,\ 4,\ 6$ for the first three hydrogenation cycles. The 200 nm Mg_yFe films are capped with 5 nm Pd. For $y = 4,\ 6$ dehydrogenation in air was not possible even when heated up to 95 °C.

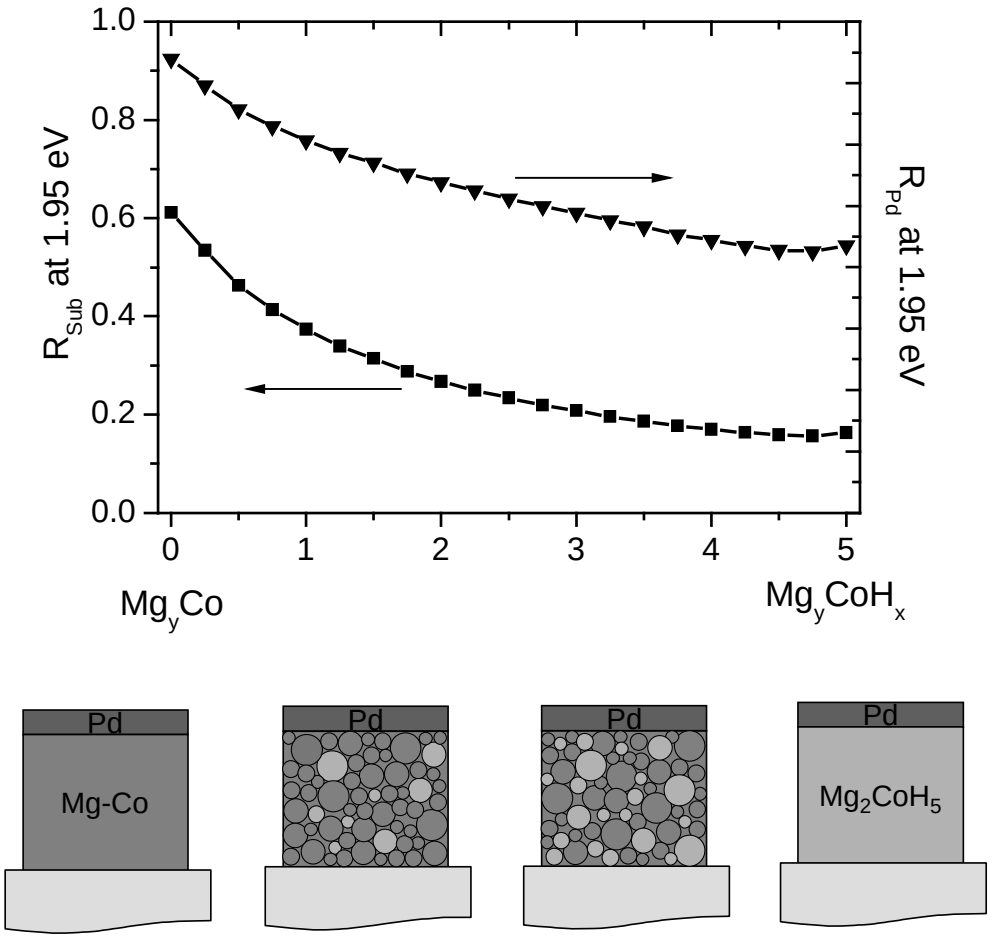

Figure 3.18: First model of the hydrogenation process of Mg_yCo with $y = 2$ of homogeneous nucleation throughout the film (see text).

represents a mixture of the first two cases. Nucleation starts at the substrate-film interface after which homogeneously dispersed nucleation through the entire film takes over. R_{Pd} stays constant while R_{sub} drops and starts to oscillate. When R_{Pd} starts to decrease, the oscillations fade away. Since the transmission and reflection of Mg_yCo with $y = 2$ are approximately similar to the optical properties of Mg_yCo with $y = 3,\ 4,\ 6$, we assume that the features in Figure 3.18-3.20 for Mg_yCo with $y = 2$ hold for the other compositions as well.

When comparing the model with the measured reflection in Figure 3.19, we conclude that the Mg_yCo ($y = 2$) shows a double layer formation. Especially for the second and third hydrogen loading cycle the oscillations in R_{sub} are only vague,

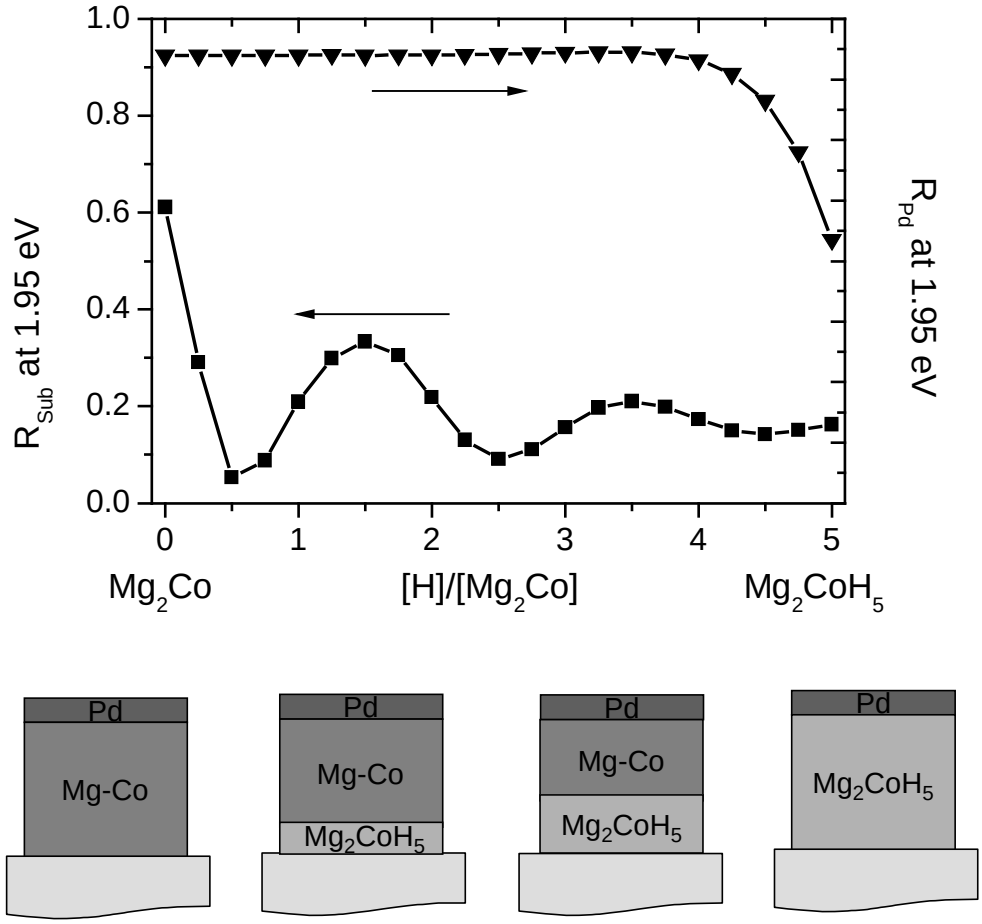

Figure 3.19: Second model of the hydrogenation process of Mg_yCo with $y = 2$. Nucleation at the substrate-film interface induces a double layer formation whereafter the hydride grows at the expense of the metallic upper layer.

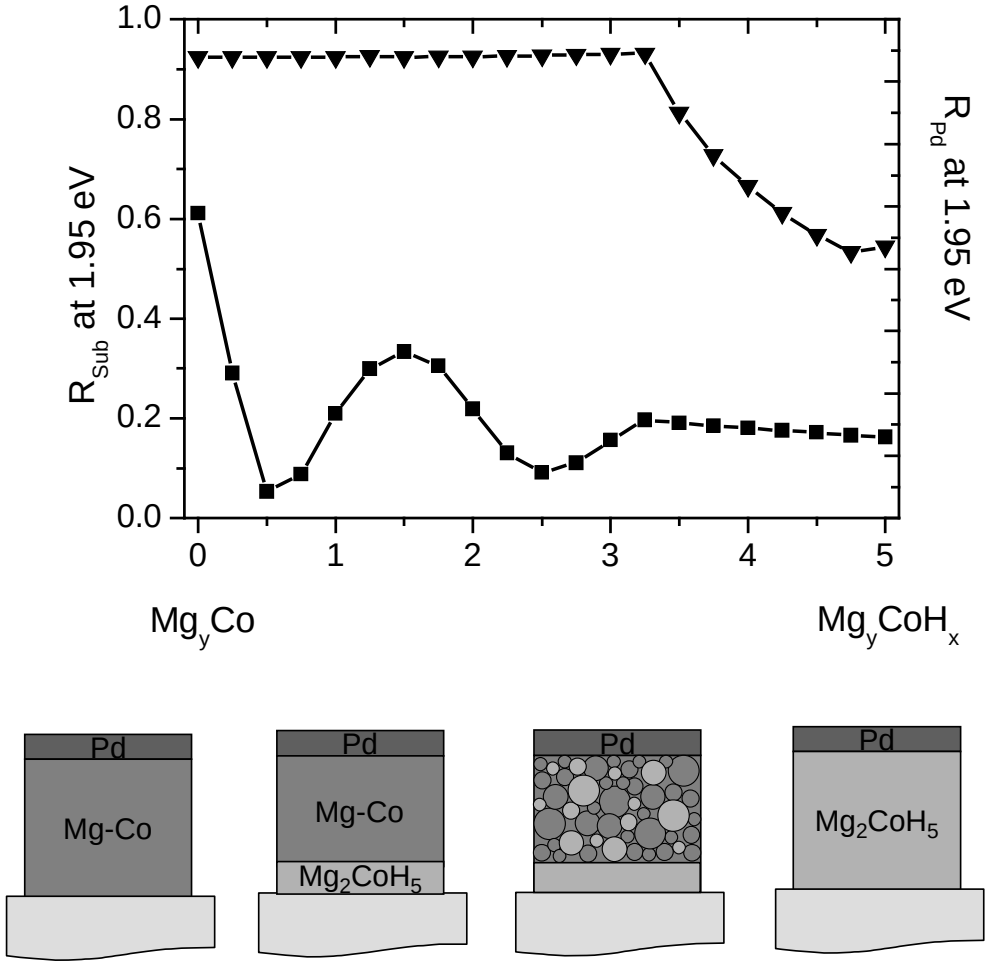

Figure 3.20: Third model of the hydrogenation process of Mg_yCo with $y = 2$. This is a combination of the first (see Fig. 3.18) and second (see Fig. 3.19) models; a double layer formation evolves into homogeneous nucleation at intermediate hydrogen concentration.

Material	Composition	X-ray peak	Mg-grain size	
			As-deposited	Dehydrogenated
Mg_yCo	$y = 2$	Mg (002)	amorph	-
	$y = 3$	Mg (002)	23	amorph
	$y = 4$	Mg (002)	33	-
	$y = 6$	Mg (002)	34	-
Mg_yFe	$y = 6$	Mg (002)	29	17

Table 3.2: As-deposited and dehydrogenated Mg-grain size in nanometers estimated from x-ray diffraction measurements by means of equation 3.10 for various Mg-concentrations of the Mg-Co and Mg-Fe system. If no peak is observed, the material is amorphous or polycrystalline with very small grains.

which might be due to a rough interface between the hydride and metal layer. R_{Pd} decreases at high hydrogen concentration. The first hydrogen loading of $y = 4$ shows a mixture of both nucleation types; a double layer formation evolves into homogeneous nucleation at intermediate hydrogen concentration. However, subsequent hydrogen loading cycles show a full double layer formation. Mg_yCo ($y = 6$) shows a complete homogeneous loading for the first hydrogenation cycle, the subsequent hydrogen loading cycle is completely double layer like. Mg_yFe ($y = 2,\ 4,\ 6$) shows homogeneous nucleation throughout the entire film during hydrogenation of the as-prepared film. For $y = 2$, the subsequent hydrogen loading cycles exhibit a more double-layer like formation behavior.

3.4.4 Structure

Figure 3.21 shows the SEM images of cross-sections of Mg_yCoH_x films with $y = 2,\ 4$ as-prepared and after three hydrogen loading cycles. After the final hydrogenation, the films were not dehydrogenated, which means that some hydrogen might have remained in the films. For as-deposited Mg_yCo with $y = 2$ very small grains are observed with a diameter in the order of ∼10 nm. After three switching cycles, grain boundaries are observed more clearly with a slightly larger grain size. No columnar structure or gradient in the grain size is observed. For as-deposited Mg_yCo with $y = 4$ the grain size is larger and much more visible than for $y = 2$. In this case, however, the grain boundaries become much less distinct after the three switching cycles. The grain size has decreased after the hydrogen loading cycles. At the substrate-film interface of the Mg_yCoH_x with $y = 4$, there is probably still some ± 35 nm expanded hydride phase left, as can be seen by the different microstructure in that layer.

XRD-measurements on the as-deposited Mg_yCo samples (see Figure 3.22) show an increasing peak height of the (002) and (004) Mg-peak with increasing Mg-to-Co ratio. For $y = 2$ no Mg-peak is observed. The higher the Mg-content, the more the peaks are shifted to higher angles (from $2\theta = 34.34°$ for $y = 3$ to $2\theta = 34.52°$ for $y = 6$. For bulk Mg $2\theta = 34.40°$ [58]), which means the lattice is compressed for

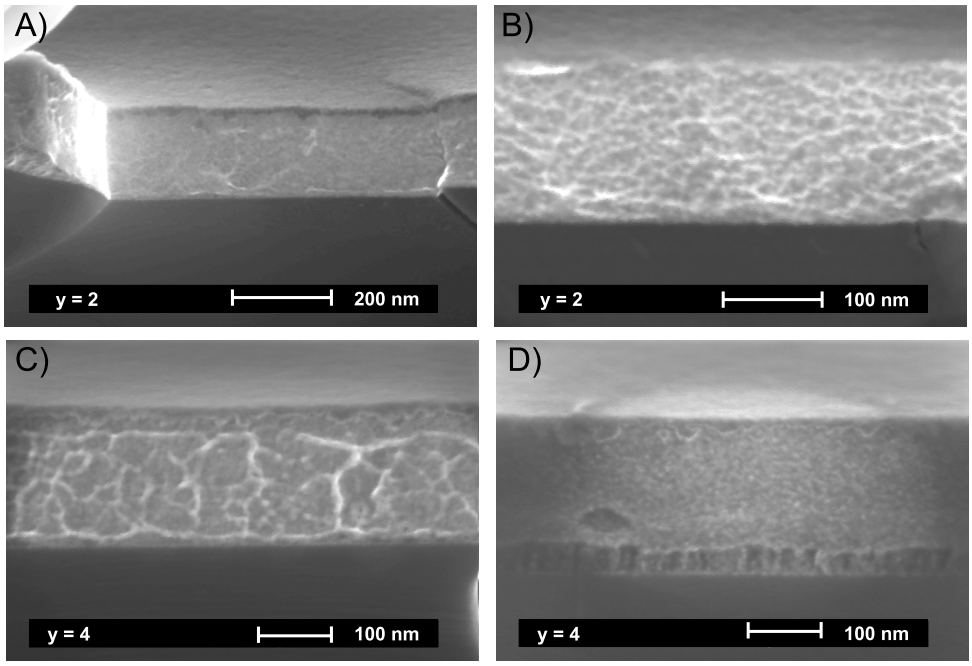

Figure 3.21: SEM micrographs of the cross section of 200 nm thick Mg_yCoH_x films deposited on a Si substrate and covered by 10 nm Pd. a) $y = 2$, as-prepared, b) $y = 2$, after three switching cycles c) $y = 4$, as-prepared d) $y = 4$, after three switching cycles. The film has not been dehydrogenated and there is probably some hydrogen left in the lower 40 nm. For $y = 2$ small grains of the order of ∼10 nm are observed. We find that the grain size increases with increasing Mg-content. For $y = 4$, the grain size decreased after the switching cycles. Note that the pictures have different scales. (RUG: B.J. Kooi and G.H. ten Brink)

$y = 6$ as compared to $y = 2$. The grain size can be estimated from the coherence length l_{coh} using the Scherrer equation:

$$l_{coh} = \frac{0.89\lambda}{\Delta(2\theta)cos\theta} \tag{3.10}$$

where λ is the wavelength of the x-rays (1.5418 Å), 2θ is the position of the center of the peak, and $\Delta(2\theta)$ is the full width at half maximum (FWHM) in radians. The results of the Mg (002) peak for Mg_yCo ($y = 3,\ 4,\ 6$) are given in table 3.2 The peak observed at $2\theta = 46.5°$ ($d = 1.95$ Å) which increases with increasing Mg-content

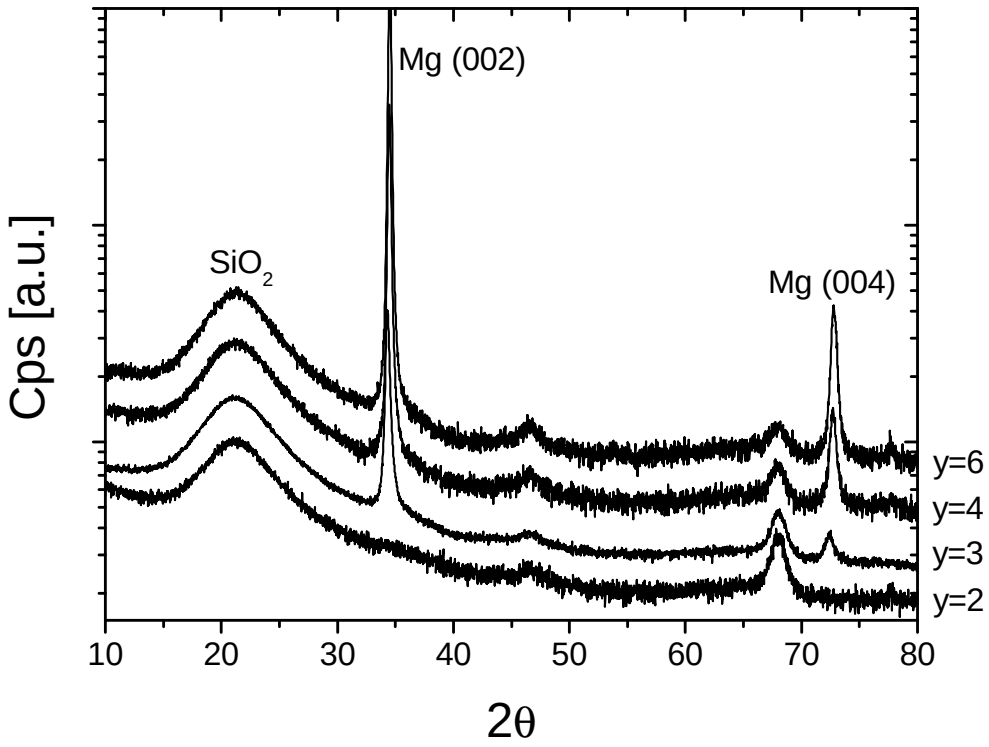

Figure 3.22: X-ray diffraction spectra of 200-nm thick Mg_yCo ($y = 2,\ 3,\ 4,\ 6$) samples. The different spectra have been shifted for clarity. We observe an increase of the peak height with increasing Mg-to-Co ratio for the (002) and (004) Mg peak and a decrease of the lattice spacing. The small peak at $2\theta = 46.5°$ ($d = 1.95$ Å) is probably due to Mg_2Pd_5 (222).

might be ascribed to Mg_5Pd_2 (222). At $2\theta = 68°$ ($d = 1.38$Å) a peak is observed which decreases with increasing Mg-content. Upon hydrogenation, the Mg-peaks disappear. The Mg_5Pd_2 (222) and the peak at position $2\theta = 68°$ shift to lower angles, indicating a lattice expansion due to hydrogen absorption (see Figure 3.23). In the hydride state a peak at $2\theta = 43.3°$ ($d = 2.09$ Å) appears. After dehydrogenation the Mg-peaks do not reappear, which means that they have either formed a compound or have become X-ray amorphous. The Mg_5Pd_2 (222) and the peak at position $2\theta = 68°$ shift back and even shift to slightly higher angles. The peak at $2\theta = 43.3°$, which appeared during hydrogenation, stays and does not move, so it can probably be ascribed to MgO (200).

XRD-measurements of Mg_yFe with $y = 6$ showed that after hydrogenation a smaller and broader Mg (002) peak reappears.

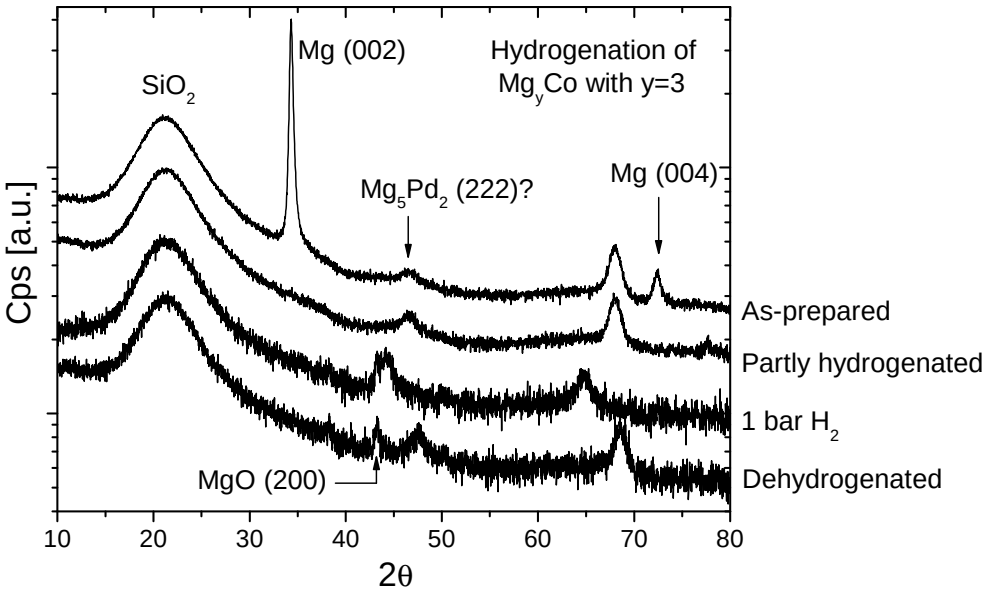

Figure 3.23: X-ray diffraction spectra of Mg_yCoH_x with $y = 3$ during hydrogenation. The Mg-peaks disappear and do not reappear after dehydrogenation. Two peaks shift to lower angles indicating hydrogen absorption. The MgO (200) peak appears during hydrogenation.

3.5 Discussion

We discuss the observed relation between hydrogen loading behavior and Mg-TM ratio, the transition metal used and the hydrogen loading cycle number. The hydrogenation behavior seems to correlate well with the amount of crystalline Mg present. We propose that the change in hydrogen loading behavior of Mg_yTM (TM=Co, Fe) from a partly random nucleation to a more double layer formation is caused by the improved mixture of the Mg and the TM upon subsequent hydrogen loading cycles.

X-ray diffraction measurements do not show Mg-peaks for the as-prepared Mg_yCo for $y = 2$. For Mg_yCo with $y > 2$, however, two Mg-peaks are observed, increasing in height with increasing y and disappearing during the first hydrogen loading cycle, indicating that after hydrogenation Mg becomes either x-ray amorphous or has formed an alloy compound. SEM-measurements of Mg_yCo ($y = 4$) confirmed the grain size reduction after hydrogenation. The hydrogenation behavior for Mg_yCo ($y = 2$) does not change upon subsequent hydrogen loading cycles, whereas the reflection of Mg_yCo with $y > 2$ shows a change from a partly homogeneously dispersed nucleation to a more double layer formation between the first and the second hydrogenation cycle, increasing with increasing Mg-content. Thus, a decrease in Mg-grain size in the Mg-Co films seems to correlate with a more pronounced double layer

formation upon hydrogenation. For Mg_yFe ($y = 2$) a smaller and broader Mg-peak reappears after the first hydrogen loading cycle; the grain size has decreased, but Mg has not become completely x-ray amorphous. The measured reflection of the sample suggests that the homogeneously dispersed nucleation becomes more double layer like during the second hydrogen loading and changes even further during the third hydrogenation of the film. Therefore, the Mg_yFe shows the same relation between Mg-grain size and hydrogen loading behavior. For bulk Mg_yFe materials a decrease in grain size upon subsequent hydrogenation cycles has been observed [59] as well.

Another indication for the reduced grain size in the Mg_yCo-films with $y > 2$ upon subsequent hydrogen loading cycles is the measured transmission of the Mg_yCoH_x in the hydride state. For $y = 2$ no change in the final transmission upon hydrogen loading cycle is observed. However, for Mg_yCoH_x with $y = 4,\ 6$ the transmission increases in subsequent hydrogen loading cycles. Not only the final transmission is higher, the oscillations in the transmission and reflection at low energies during the hydrogenation process, are stronger indicating that the transparent layer formed has a higher transmission. This increase in transmission can be explained by a lower amount of residual metallic Mg. If relatively large Mg-grains are present, the center part of the Mg-grain possibly stays metallic during the hydrogenation process.

While the change in hydrogenation behavior of Mg_yTM films during subsequent hydrogenation cycles is related to the Mg-grain size reduction, the difference between the Mg-TM metals (TM=Co, Fe, Ni) can be accounted for when looking at the phase diagram of the parent materials. For Mg_2Ni films a binary Mg-TM parent alloy exists with the same composition as the ternary Mg_2TM hydride. This compound has been observed with x-ray diffraction measurements, while no Mg-peak was observed. Hence the elements are mixed completely in the as-prepared state and no difference in subsequent hydrogen loading cycles is observed. For the Mg-Co system, two binary compounds are known, $MgCo_2$ and MgCo, although they differ in composition from the hydride and are not observed in our x-ray diffraction measurements. MgCo has only been observed after dehydrogenation or heating [8]. The changes in the hydrogenation process of the Mg_yCo system between the first and second hydrogen loading cycle can be explained by a hydrogen enhanced mixing of Mg and Co (see Figure 3.24. In the hydride phase Mg and Co atoms are combined in the ternary compound Mg_2CoH_5. The non-reacted Mg forms smaller grains. Mg and Fe do not form any binary compounds and hence the mixture of these elements is expected to be the least of all Mg_yTM (TM=Ni, Co, Fe). This results in large differences in the hydrogenation process on subsequent hydrogen loading cycles. The difference in microstructure between the bottom-layer and the top-layer has been proposed to be at the origin of the black state in Mg_yNi films [49, 50]. However, such a difference is not observed for Mg_yCo and Mg_yFe films. We propose that the origin of the hydride formation lies in the difference in high surface energy sites for nucleation. For the nucleation of the hydride phase a barrier is present. This barrier is caused by the lack of coherence between the metal and hydride crystal structure and the expansion upon hydride formation ($\sim$30%). In order to overcome this nucleation barrier, nucleation starts preferentially at heterogenous incongruent grain bound-

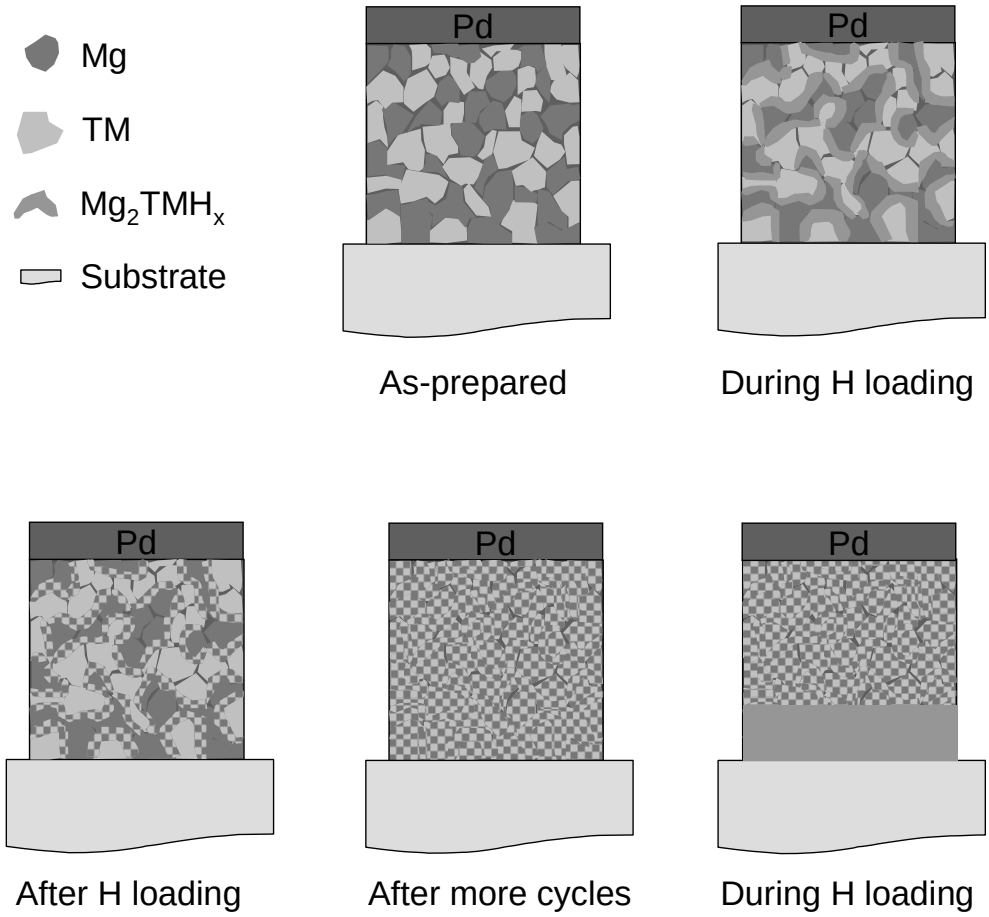

Figure 3.24: Structure changes during hydrogenation cycles: The as-prepared film consists of Mg and TM grains. During hydrogenation, the Mg_2TMH_x phase is formed at the grain boundaries between the different grains, i.e. nucleation is observed throughout the entire film. After dehydrogenation a more mixed film exists as compared to the as-prepared film. When the film is completely mixed, the hydride nucleation starts as usual at the substrate film interface.

aries, since these already have a high surface energy. The substrate therefore acts as a nucleation site for the hydride formation. However, in the as-deposited Mg_yCo and Mg_yFe with $y > 2$ Mg-grains and small transition metal grains coexists. The heterogenous incongruent boundaries between these grains possess a large surface energy and thus promote nucleation. The grain boundaries between grains of the same material have less surface energy and are therefore not suited for nucleation. Therefore, in the less well mixed films a competition between nucleation at the substrate and at the grain boundaries between the Mg and TM grains homogeneously dispersed throughout the film is observed.

3.6 Conclusions

We observed for all Mg_yTM (TM=Co, Fe) the characteristic phonons of the complex hydride Mg_2TMH_x. Furthermore, we have shown that the dielectric functions determined from the measured reflection and transmission are clearly not a combination of the metallic TM and MgH_2. Therefore, we conclude that the complex Mg_2TM hydrides have been formed upon hydrogenation at room temperature.

We find that the reflection in the as-prepared state increases with increasing Mg-content, whereas the reflection in the fully hydrogenated state decreases. Therefore, the contrast between the metallic and the hydride state is largest for the case with the highest Mg-content. Moreover, the transmission increases and the transmission edge shifts to higher energies with increasing Mg-content. Comparing the transition metals we find in the TM=Fe case the highest reflection in the as-prepared state, while TM=Ni has the lowest.

Besides the metal and the hydride state, we investigated the intermediate optical properties during the hydrogen loading. To better understand our experimental findings we have modelled different hydrogenation scenarios. The scenarios consist of i) a Bruggeman approximation with homogeneous nucleation throughout the film ii) nucleation at the substrate-film interface resulting in the formation of a double layer system iii) a mixture of both homogeneously dispersed hydride with a transparent layer at the substrate-film interface. From the model we find that a homogeneous nucleation is characterized by the absence of interference oscillations in the substrate reflection as well as a gradual decrease of both the Pd R_{Pd} and substrate reflection R_{sub} signals. The double layer formation is characterized by the presence of interference oscillations in the substrate reflection R_{sub} whereas, the Pd reflection R_{Pd} remains constant with a cut off at highest hydrogen concentration. We observed that in contrast to TM=Ni, which from the first hydrogen loading cycle shows a clear double layer formation upon hydrogen uptake, the hydrogenation behavior of TM=Co, Fe depends on the loading cycle. In subsequent cycles we observe that the hydrogenation behavior evolves from a mainly homogeneous nucleation throughout the film to a more double-layer like behavior. This change in loading behavior is more pronounced for TM=Fe than for TM=Co and increases with Mg-content. The influence of the Mg dispersion can be held responsible for the differences in the observed

optical behavior. We argue that Mg-clusters form heterogeneous incoherent grain boundaries which act as nucleation sites for hydride formation, thereby competing with the substrate-film interface and promoting homogeneously dispersed nucleation at the expense of a double layer formation. Both x-ray diffraction measurements and SEM observations confirm the relation between the Mg grain size and the homogeneous nucleation behavior. The difference between the different MgTM-systems in the amount of Mg-clusters can be understood when looking at the binary phase diagrams of the parent alloys. The existence of binary compounds, especially when having the same composition as the hydride, is thought to increase the mixing of the Mg and the TM and thereby reduce the size of the Mg-clusters. Hydrogenation itself is suggested to reduce the Mg grain size and improve the mixing of Mg and the transition metal.

Finally, the question remains which of the discussed systems is best suited for a switchable device. Although the largest contrast in optical properties between the metal and hydride state is observed in Mg_yFe with $y = 6$, this system changes continuously during hydrogen loading cycles. After a substantial amount of cycles, the system might become stable, however, training the material is too costly. The Mg-Ni system is much more stable. Therefore, we propose Mg_yNi with $y = 6$ as the most suitable candidate for the use as a switchable mirror in an all-solid-state device for the following reasons: i) Mg_yNi with $y = 6$ is known to have a large contrast in reflection between the metallic and hydride state ii) has a large and color neutral transmission spectrum and iii) as mentioned before, has no change in hydrogenation behavior on subsequent hydrogen loading cycles.

Bibliography

[1] T.J. Richardson, J.L. Slack, R.D. Armitage, R. Kostecki, B. Farangis, and M.D. Rubin. Switchable mirrors based on nickel-magnesium films. *Appl. Phys. Lett.*, 78(20):3047–3049, 2001.

[2] T.J. Richardson, J.L. Slack, B. Farangis, and M.D. Rubin. Mixed metal films with switchable optical properties. *Appl. Phys. Lett.*, 80(8):1349–1351, 2002.

[3] J.N. Huiberts, R. Griessen, J.H. Rector, R.J. Wijngaarden, J.P. Dekker, D.G. de Groot, and N.J. Koeman. Yttrium and lanthanum hydride films with switchable optical properties. *Nature*, 380:231–234, 1996.

[4] J. Isidorsson, I.A.M.E. Giebels, R. Griessen, and M. Di Vece. Tunable reflectance Mg-Ni-H films. *Appl. Phys. Lett.*, 80(13):2305–2307, April 2002.

[5] J.L.M. van Mechelen, B. Noheda, W. Lohstroh, R.J. Westerwaal, J.H. Rector, B. Dam, and R. Griessen. Mg-Ni-H films as selective coatings: Tunable reflectance by layered hydrogenation. *Appl. Phys. Lett.*, 84:3651–3653, 2004.

[6] J.J. Reilly and jr. R.H. Wiswall. The reaction of hydrogen with alloys of magnesium and nickel and the formation of Mg_2NiH_4. *Inorg. Chem.*, 7:2254–2256, 1968.

[7] M. Yoshida, F. Bonhomme, K. Yvon, and P. Fischer. On the composition and structure of the cubic delta-phase in the Mg-Co-H system. *J. Alloys Compd.*, 190(6):L45–L46, 1993.

[8] Fabiana C. Gennari and Facundo J. Castro. Formation, composition and stability of Mg-Co compounds. *J. Alloys Compd.*, 396:182–192, 2005.

[9] P. Zolliker, K. Yvon, P. Fischer, and J. Schefer. Synthese, Struktur und Eigenschaften von Mg_2CoH_5. *J. Helv. Phys. Acta*, 57(6):754, 1984.

[10] P. Zolliker, K. Yvon, P. Fischer, and J. Schefer. Dimagnesium cobalt (i) pentahydride, Mg_2CoH_5, containing square-pyramidal CoH_5^{4-}. *Inorg. Chem.*, 24:4177–4180, 1985.

[11] E.J. Ivanov, I. Konstanchuk, A. Stepanov, Yan Jie, M. Pezat, and B. Darriet. The ternary system Mg-Co-H. *Inorg. Chem.*, 28:613–615, 1989.

[12] R. Černý, F. Bonhomme, K. Yvon, P. Fischer, P. Zolliker, D.E. Cox, and A. Hewat. Hexamagnesium dicobalt undecadeuteride $Mg_6Co_2D_{11}$: containing $[CoD_4]^{5-}$ and $[CoD_5]^{4-}$ complex anions conforming to the 18-electron rule. *J. Alloys Compd.*, 187:233–241, 1992.

[13] Michèle Gupta, Esther Belin, and Louis Schlapbach. Density of occupied states of intermetallic hydride $NiMg_2H_4$. *J. Less-Common Met.*, 103:389–399, 1984.

[14] E. Berlin, M. Gupta, P. Zolliker, and K. Yvon. An experimental and theoretical investigation of the densities of states of dimagnesium cobalt pentahydride. *J. Less-Common Met.*, 130:267–274, 1987.

[15] Michèle Gupta. Electronic structure of intermetallic hydrides: Mg_2FeH_6 and Ca_2RuH_6. *J. Less-Common Met.*, 103:325–335, 1984.

[16] Emilio Orgaz and Michèle Gupta. The electronic properties of intermetallic hydrides with the K_2PtCl_6 structure. *J. Phys.: Condens. Matter*, 5(36):6697–6718, 1993.

[17] J. Isidorsson, I.A.M.E. Giebels, M. Di Vece, and R. Griessen. Electrochromism of Mg-Ni hydride switchable mirrors. In *Proc. SPIE*, volume 4458, pages 128–137, 2001.

[18] D. Lupu, R. Sârbu, and A. Biriş. Semiconducting properties of Mg_2NiH_4. *Int. J. Hydrogen Energy*, 12(6):425–426, 1987.

[19] W. Lohstroh, R.J. Westerwaal, J.L.M. van Mechelen, C. Chacon, E. Johansson, B. Dam, and R. Griessen. The structural and optical properties of $Mg_{2\pm y}NiH_x$ switchable mirrors upon hydrogen loading. *Phys. Rev. B*, 70:165411, 2004.

[20] J. Isidorsson, I.A.M.E. Giebels, H. Arwin, and R. Griessen. Optical properties of MgH_2 measured in situ by ellipsometry and spectrophotometry. *Phys. Rev. B*, 68:115112, 2003.

[21] S. Orimo and H. Fujii. Materials science of Mg-Ni-based new hydrides. *Appl. Phys. A*, 72:167–186, 2001.

[22] A.A. Nayeb-Hashemi and J.B. Clark. *Phase Diagrams of Binary Magnesium Alloys*. Metals Park, Ohio, 1988.

[23] Jack H. Westbrook, editor. *Handbook of Binary Phase Diagrams*, volume 3. Genium Publishing Corporation, New York, 1997.

[24] Klaus Yvon. Complex transition-metal hydrides. *Chimia*, 52:613–619, 1998.

[25] Klaus Yvon. *Encyclopedia of inorganic chemistry*, volume 3, chapter Hydrides: Solid State Transition Metal Complexes, pages 1401–1420. Chichester: Wiley, 1994.

[26] Louis Schlapbach. Hydrogen as a fuel and its storage for mobility and transport. *MRS Bull.*, pages 675–679, 2002.

[27] R. Griessen, A. Driessen, and D.G. de Groot. Search for new metal-hydrogen systems for energy storage. *J. Less-Common Met.*, 103:235–244, 1984.

[28] Huaiyu Shao, Hairuo Xu, Yuntao Wang, and Xingguo Li. Synthesis and hydrogen storage behavior of Mg-Co-H system at nanometer scale. *J. Solid State Chem.*, 177:3626–3632, 2004.

[29] J.-J. Didisheim, P. Zolliker, K. Yvon, P. Fischer, J. Schefer, M. Gubelmann, and A.F. Williams. Dimagnesium iron (ii) hydride, Mg_2FeH_6, containing octahedral FeH_6^{4-} anions. *Inorg. Chem.*, 23(13):1953–1957, 1984.

[30] James P. Blackledge William M. Mueller and George G. Libowitz. *Metal Hydrides*. Mueller, New York, 1968.

[31] Jr. J.F. Stampfer, Jr. C.E. Holley, and J.F. Suttle. The magnesium-hydrogen system. *J. Amer. Chem. Soc.*, 82:3504–3508, 1960.

[32] Borislav Bogdanović, Klaus Bohmhammel, Babett Christ, Alexander Reiser, Klaus Schlichte, Ralph Vehlen, and Ulrich Wolf. Thermodynamic investigation of the magnesium-hydrogen system. *J. Alloys Compd.*, 282:84–92, 1999.

[33] A. Zaluska, L. Zaluski, and J.O. Ström-Olsen. Nanocrystalline magnesium for hydrogen storage. *J. Alloys Compd.*, 288:217–225, 1999.

[34] L.J. van der Pauw. A method of measuring specific resistivity and hall effect of discs of arbitrary shape. *Philips Res. Rep.*, 13(1):1–9, February 1958.

[35] Marcel van Gogh. *Probing the Metal-Insulator Transition in Rare-Earth Based Switchable Mirrors.* PhD thesis, Vrije Universiteit, Amsterdam, February 2001.

[36] M. Born and E. Wolf. *Principles of Optics.* Pergamon Press, Oxford, 6th edition, 1980.

[37] A.T.M. van Gogh and R. Griessen. Dihydride transmission quenching in switchable $La_{1-z}Y_zH_x$ mirrors. *J. Alloys Compd.*, 330-332:338–341, 2002.

[38] A.T.M. van Gogh, D.G. Nagengast, E.S. Kooij, N.J. Koeman, J.H. Rector, and R. Griessen. Structural, electrical and optical properties of $La_{1-z}Y_zH_x$ switchable mirrors. *Phys. Rev. B*, 63:195105, February 2001.

[39] F. Wooten. *Optical properties of solids.* Academic Press, New York, 1972.

[40] Craig F. Bohren and Donald R. Huffman. *Absoprtion and Scattering of Light by Small Particles.* Wiley-Interscience, New York, 1998.

[41] D.A.G. Bruggeman. Berechnung verschiedener physikalischer konstanten von heterogenen substanzen. *Annalen der Physik*, 24(5):636, 1935.

[42] W.R. Myers, L.-W. Wang, T.J. Richardson, and M.D. Rubin. Calculation of thermodynamic, electronic, and optical properties of monoclinic Mg_2NiH_4. *J. Appl. Phys.*, 91(8):4879–4885, April 2002.

[43] K. Yoshimura, Y. Yamada, and M. Okada. Optical switching of Mg-rich Mg-Ni alloy thin films. *Appl. Phys. Lett.*, 81(25):4709–4711, December 2002.

[44] W. Lohstroh, R.J. Westerwaal, B. Noheda, S. Enache, I.A.M.E. Giebels, B. Dam, and R. Griessen. Self-organized layered hydrogenation in black Mg_2NiH_x switchable mirrors. *Phys. Rev. Lett.*, 93(19):197404, November 2004.

[45] B. Farangis, P. Nachimuthu, T.J. Richardson, J.L. Slack, B.K. Meyer, R.C.C. Perera, and M.D. Rubin. Structural and electronic properties of magnesium-3D transition metal switchable mirrors. *Solid State Ionics*, 165:309–314, 2003.

[46] W. Lohstroh, R.J. Westerwaal, A.C. Lokhorst, J.L.M. van Mechelen, B. Dam, and R. Griessen. Double layer formation in Mg-TM switchable mirrors (TM: Ni, Co, Fe). *J. Alloys Compd.*, 404-406:490–493, 2005.

[47] W. Lohstroh, R.J. Westerwaal, J.L.M. van Mechelen, H. Schreuders, B. Dam, and R. Griessen. The dielectric function of Mg_yNiH_x thin films ($y = 2 - 10$). *submitted to Phys. Rev. B.*

[48] Ingrid A.M.E. Giebels. *Shining light on magnesium based switchable mirrors.* PhD thesis, Vrije Universiteit Amsterdam, 2004.

[49] R.J. Westerwaal, A. Borgschulte, W. Lohstroh, B. Dam, and R. Griessen. Microstructural origin of the optical black state in Mg_2NiH_x thin films. *J. Alloys Compd.*, 404-406:481–484, 2005.

[50] R.J. Westerwaal, A. Borgschulte, W. Lohstroh, B. Dam, B. Kooi, G. ten Brink, M.J.P. Hopstaken, and P.H.L. Notten. The growth induced microstructural origin of the optical black state of mg_2nih_x thin films. *J. Alloys Compd. (in press)*, 2005.

[51] I.A.M.E. Giebels, J. Isidorsson, and R. Griessen. Highly absorbing black Mg and rare-earth-Mg switchable mirrors. *Phys. Rev. B*, 69:205111, 2004.

[52] E.D. Palik. *Handbook of Optical Constants of Solids book.* Academic Press, San Diego, 1998.

[53] Dook van Mechelen. The highly tunable mg-ni-h switchable mirror system. Master's thesis, Vrije Universiteit Amsterdam, 2004.

[54] E.A. Davis and N.F. Mott. Conduction in non-crystalline systems v. conductivity, optical absorption and photoconductivity in amorphous semiconductors. *Phil. Mag.*, 22:903–922, 1970.

[55] Stewart F. Parker, Upali A. Jayasooriya, John C. Sprunt, Manfred Bortz, and Klaus Yvon. Inelastic neutron scattering, IR and raman spectroscopic studies of Mg_2CoH_5 and Mg_2CoD_5. *J. Chem. Soc., Faraday Trans.*, 94(17):2595–2599, 1998.

[56] Stewart F. Parker, Kenneth P.J. Williams, Manfred Bortz, and Klaus Yvon. Inelastic neutron scattering, infrared, and raman spectroscopic studies of Mg_2FeH_6 and Mg_2FeD_6. *Inorg. Chem.*, 36:5218–5221, 1997.

[57] Stewart F. Parker, Kenneth P.J. Williams, Tim Smith, Manfred Bortz, Bernard Bertheville, and Klaus Yvon. Vibrational spectroscopy of tetrahedral ternary metal hydrides: Mg_2NiH_4, $RbZnH_5$ and their deuterides. *Phys. Chem. Chem. Phys.*, 4:1732–1737, 2002.

[58] JCPDS 35-0821. space group: $P6_3/mmc$, a=3.2136(3) Å, c=5.2113(2) Å.

[59] Borislav Bogdanović, Alexander Reiser, Klaus Schlichte, Bernd Spliethoff, and Bernd Tesche. Thermodynamics and dynamics of the Mg-Fe-H system and its potential for thermochemical thermal energy storage. *J. Alloys Compd.*, 345:77–89, 2002.

Chapter 4

Thermochromic devices

Thermochromic windows are usually based on oxides which change from metallic to transparent at a well-defined metal-insulator transition temperature. Here, we propose to make use of the optical properties of metal hydrides, which change strongly with their hydrogen content. These materials have the advantage that also the optical absorption can be switched. Such a metal-hydride thermochromic device can be realized in two different configurations: (1) a gas cell device in which a metal-hydride layer (e.g. Mg_yNiH_x) is in contact with a hydrogen atmosphere at constant pressure. Increasing the temperature results in hydrogen desorption from the metal-hydride film and thus in a change in the optical properties of the metal hydride. (2) an all-solid-state device which consists of a metal-hydride bilayer (a switchable mirror and an optically inert hydrogen reservoir layer). In this novel scheme the two layers are covered by a cap layer which is impermeable to hydrogen. Due to differences in the thermodynamic properties of the two metal-hydride layers, a temperature change results in the migration of hydrogen from one layer to the other, thereby changing the optical properties of the switchable mirror metal-hydride. The thermodynamical background of both the gas cell and the all-solid-state thermochromic device is presented, together with some preliminary results on experimental devices in the two configurations. Finally, we analyze the factors which affect the proper functioning of the device.

4.1 Introduction

The use of smart windows is envisaged to reduce the energy consumption for heating and cooling buildings without decreasing the level of comfort. Smart windows are often based on thermochromic materials, which by definition change their optical properties upon a temperature change. Due to a metal-insulator transition thermochromic VO_2 changes below 68°C from the reflecting high temperature phase to the transparent low temperature phase at wavelengths larger than 600 nm (i.e. $\hbar\omega \leq 2.1$ eV). This change is very abrupt, i.e. there are no intermediate states possible. Furthermore, since the thermally induced change in transmission is accompanied by a change in reflection [1], VO_2 cannot be used as a thermochromic absorber.

We propose here a much more versatile thermochromic device, which is based on the tunable optical properties of metal hydrides. The transition can be optimized for transmission, reflection or absorption depending on the materials chosen. Even the wavelength region in which the optical changes take place can be adjusted. Furthermore, the transition is much more gradual, than in the case of VO_2, where the optical change is due to a temperature-induced phase transition [1].

Possible applications of such a versatile thermochromic metal-hydride device include the fabrication of a thermochromic *absorber*. In such a device the absorbing coating is black and heat absorbing at low temperatures while reflecting at high temperatures. It could be used to optimize the efficiency of hybrid solar collectors - a device with a photovoltaic cell on top of a thermal solar collector - by keeping its operational temperature within practical limits (see Section 1.2 and 4.3.1). Another possibility for a metal-hydride device is a smart window for temperature control, which is transparent at low and reflecting at high temperatures (see Section 1.2 and 4.3.2).

We propose a metal hydride as the optically active layer in the thermochromic device. The reversible change of metal hydrides from shiny reflecting to transparent has first been observed in Y and La thin films [2]. All rare earth (RE) metals and their alloys with Mg were found to switch optically [3] and furthermore Richardson *et al.* [4] demonstrated that Mg-TM (TM: Ni, Co, Mn, Fe) also act as switchable mirrors. The RE-Mg [5] and Mg-TM (TM: Ni, Co, Mn, Fe) [6] exhibit a third, black, absorbing state at intermediate hydrogen concentrations (see Chapter 3).

The thermochromic effect of switchable mirrors was first seen by Giebels *et al.* [7] in a metal-hydride film in equilibrium with H_2 (g). They showed that the intrinsic temperature dependence of the optical properties is negligible and that the change of hydrogen concentration is the main cause of the thermochromic effect. By changing the temperature, the equilibrium between hydrogen in the switchable mirror and in the surrounding atmosphere is altered. Consequently, a change in hydrogen concentration is induced, which causes a difference in the optical appearance of the switchable mirror. They measured the transmission of YH_x and $Mg_{0.1}Y_{0.9}H_x$ in an open system at 1 bar H_2 gas pressure. The $Mg_{0.1}Y_{0.9}H_x$ layers showed a much larger reduction of transmission upon temperature increase than YH_x, which is due to a

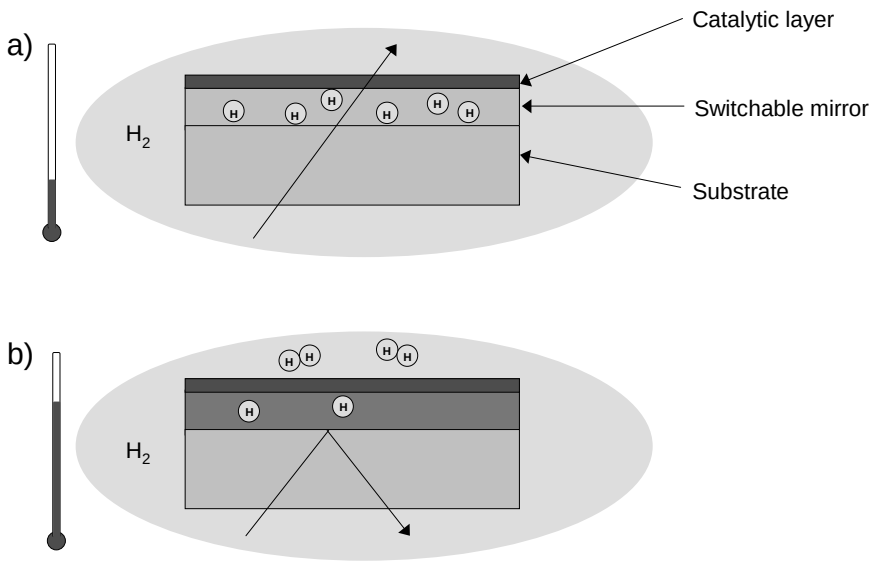

Figure 4.1: Schematic presentation of the layout and working principle of a thermochromic gas cell device. a) Device in a hydrogen atmosphere at low temperature. The metal-hydride layer appears transparent, due to the high hydrogen concentration. b) Device in the same hydrogen atmosphere at such a high temperature that most of the hydrogen has left the metal-hydride layer which therefore appears reflecting.

suppressed phase transition in the $Mg_{0.1}Y_{0.9}H_x$ layers. YH_x $(2 < x < 3)$ undergoes a phase transition upon hydrogenation. The isotherms therefore show a plateau at intermediate hydrogen concentrations, which induces a larger slope at high hydrogen concentrations. However, a two-phase region is absent for $Mg_{0.1}Y_{0.9}H_x$ resulting in both a smaller slope of the pressure-composition isotherm and the larger optical change as a function of hydrogen concentration around 1 bar H_2. Therefore, the largest thermochromic effect is observed for $Mg_{0.1}Y_{0.9}H_x$.

Compared to the work of Giebels *et al.*, the devices we propose are in principle more versatile. Whereas the YH_x or $Mg_{0.1}Y_{0.9}H_x$ films display a change in transmission upon a variation in temperature, Mg-Ni based materials can be optimized for reflection as well as absorption. The all-solid-state device has even more possibilities. While in a gas cell device the amount of hydrogen in the switchable mirror is always reduced upon a temperature increase, the all-solid-state device can be designed in such a way that the optically active layer absorbs hydrogen upon heating. Since the optical properties are related to the amount of hydrogen, in an all-solid-state device the direction of the optical switching with increasing temperature can in principle be adjusted by the choice of the reservoir layer. Moreover, the all-solid-state device is more easily integrated in applications.

Figures 4.1a and b illustrate the layout of a thermochromic gas cell device and its

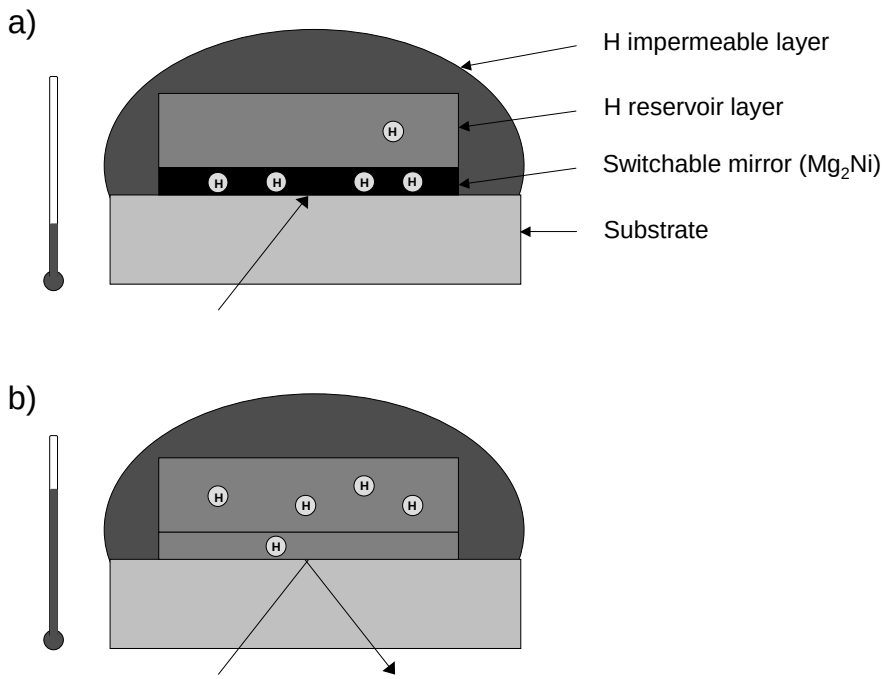

Figure 4.2: Schematic presentation of the layout and working principle of an all-solid-state device. a) Device at low temperature with some hydrogen in the switchable mirror layer which appears black b) Device at high temperature. As a result of the temperature change, some hydrogen moved from the switchable mirror to the hydrogen reservoir layer. The switchable mirror appears reflecting due to the decreased hydrogen concentration. Note, that the viewing direction is through the substrate.

working principle. The active layer of the device is the switchable mirror layer that changes its optical properties upon absorption of hydrogen. This switchable mirror layer is deposited on a transparent substrate to access optically the active layer. On top, a Pd layer is deposited, which acts as a catalyst for hydrogen uptake and as a protection against oxidation. The layers are placed into a hydrogen atmosphere with a fixed pressure and viewed from the substrate side. By changing the temperature, the equilibrium between the hydrogen in the switchable mirror and in the surrounding atmosphere is altered. Consequently, a change in hydrogen concentration and thus in the optical appearance is induced of which the magnitude depends on the thermodynamic properties of the switchable mirror.

Figures 4.2a and b show the layout of our proposed all-solid-state thermochromic device and its working principle. The device consists of two metal-hydride layers. The bottom layer has switchable optical properties. On top of this, a hydrogen reservoir layer is deposited. The metal-hydride layers are again deposited on a

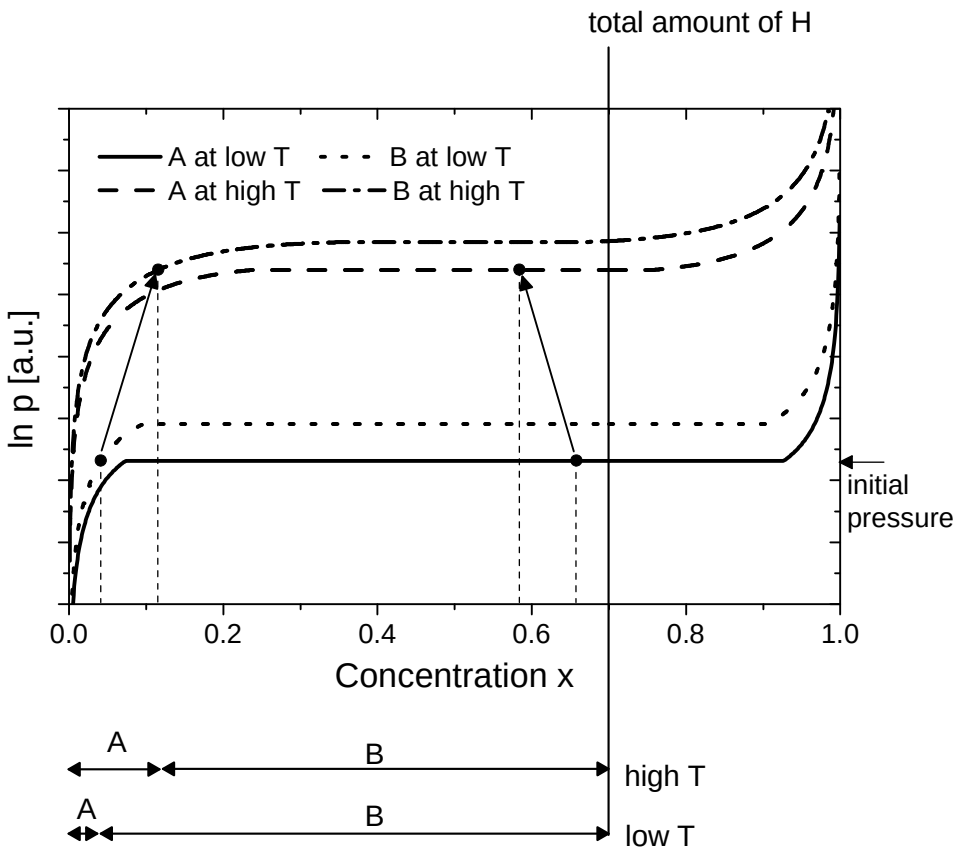

Figure 4.3: Schematic pressure-composition isotherms of metal hydrides A and B showing the hydrogen redistribution upon temperature increase in a closed system. In the example showed we have arbitrarily loaded the device with hydrogen to have $x_A = 0.04$ and $x_B = 0.66$ at low temperature. At a higher temperature these concentrations have changed to $x_A = 0.12$ and $x_B = 0.58$. It is important to note, that the total amount of hydrogen stays constant.

transparent substrate and the system is sealed by a hydrogen impermeable layer after hydrogenation at a well-defined hydrogen pressure. In an open system, hydrogen would leave the two layers upon a temperature increase, however this is prevented by the hydrogen impermeable cap. As a result, hydrogen is redistributed among the metal-hydride layers until the chemical potential of hydrogen is the same in the two layers. Figure 4.3 presents a schematic picture of the mechanism. The migrated hydrogen induces a change in optical properties of the switchable mirror layer. Depending on the required change in optical properties as viewed from the substrate side, the hydrogen reservoir layer should absorb or desorb hydrogen upon temperature increase and should therefore have a more negative or a less negative heat of absorption, respectively.

In the following, we discuss the thermodynamic properties which determine the behavior of both the gas cell and the all-solid-state thermochromic device. Furthermore, we estimate the optical change upon temperature increase of some example systems. In addition, the first results on devices based on different material system are presented.

4.2 Thermodynamic model

The change in optical appearance of our metal hydride based thermochromic devices is based on the dependence of its optical properties on its hydrogen concentration. Therefore, we investigate in which way the amount of hydrogen depends on the temperature for the two types of devices. We give a quantitative description of the hydrogen concentration in a switchable mirror layer as a function of temperature, both in a gas cell device and in an all-solid-state device.

4.2.1 Gas cell device

Let us first examine the typical behavior of a metal hydride in a hydrogen gas environment as illustrated by the pressure-composition isotherms of Figure 4.4. In the dilute α-phase the equilibrium hydrogen concentration is proportional to the square root of the hydrogen pressure, which is known as Sievert's law. At higher hydrogen concentrations, above the solubility limit of the α-phase, the β-phase precipitates. The presence of two coexisting phases is responsible for the appearance of the plateau in the pressure composition diagram. This coexistence region exists up to the critical temperature T_c, above which no distinction can be made between the α and β-phase.

The gas cell device consists of a switchable-mirror layer that is in equilibrium with the surrounding hydrogen gas (see Figure 4.1a). Then, the chemical potential μ_{H_2} of hydrogen molecules in the gas and the chemical potential μ_H of hydrogen in the metal-hydride layer M are related by:

$$\frac{1}{2}\mu_{H_2} = \mu_H \tag{4.1}$$

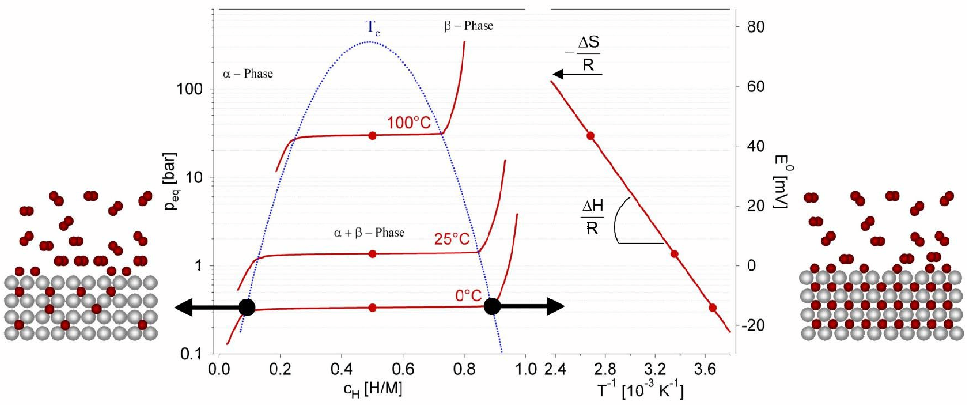

Figure 4.4: Schematic pressure-composition isotherms of a typical metal hydride. Below the critical temperature T_c the two-phase region exists indicated by the plateau. On the right hand side the Van 't Hoff plot is shown from which the formation enthalpy ΔH and entropy ΔS can be determined [8].

since hydrogen is absorbed atomically in the metal, i.e. not as an H_2 molecule. The chemical potential for the hydrogen gas is given by:

$$\mu_{H_2} = \varepsilon_{H_2} + kT \ln \frac{p}{p_0(T)} \tag{4.2}$$

where ε_{H_2} is the binding energy of the H_2 molecule (we take the zero of energy at the energy of a single H-atom, so ε_{H_2}=-4.46 eV), k the Boltzmann constant, T the absolute temperature, p the applied hydrogen pressure and the term $p_0(T)$ is given by:

$$p_0(T) = \left(\frac{(kT)^{7/2} \Theta_{H_2} m_{H_2}^{3/2}}{\hbar^5 (2\pi)^{3/2}} \right) \tag{4.3}$$

in which Θ_{H_2} is the moment of inertia and m_{H_2} ($4.72 \cdot 10^{-47}$ kgm^2 [9]) is the mass of the hydrogen molecule. In the case of hydrogen, we can approximate $p_0(T)$ by [10]:

$$p_0(T) = \left(\frac{T}{9.13} \right)^{7/2} \tag{4.4}$$

with p_0 in bar and T in K.

To describe the chemical potential of hydrogen in the metal a mean-field theory of a lattice gas is used. The term lattice gas comes from the analogy of the hydrogen atoms in a metal and a one-component material in its gaseous, liquid and solid state. At low concentrations the hydrogen atoms behave as a 'gas' in the metal;

the dissolved atoms can move throughout the whole volume of the metal. At higher concentrations and below the critical temperature T_c the hydrogen condenses i.e. the interstitial hydrogen atoms start to form clusters (β-phase) within the low-concentration α-phase, thereby entering the two-phase region [11–14]. In the Bragg-Williams approximation [15] of the lattice gas it is assumed that hydrogen atoms are distributed randomly among a number of equivalent interstitial sites. The H-H interaction consists of an electronic and an elastic part [16, 17] of which the latter one dominates. The host lattice expands upon hydrogen uptake, thereby lowering the elastic energy for further hydrogenation. The attractive elastic interaction decreases the energy of absorption. The chemical potential of hydrogen in metal M can then be given by [18, 19]:

$$\mu_H = kT \ln\left(\frac{x}{1-x}\right) + \varepsilon + ax \tag{4.5}$$

Here, x is the fraction of relevant interstitial sites that is occupied by H-atoms. ε is the energy of an H-atom in the metal host M and a is the H-H pair interaction coefficient, which is negative.

Combining equations 4.1, 4.2, 4.4 and 4.5 gives the following expression for the pressure-composition isotherms of H in metal M:

$$\ln p = 2\ln\left(\frac{x}{1-x}\right) + \frac{2}{kT}\left(\varepsilon + ax - \frac{1}{2}\varepsilon_{H_2}\right) + \ln p_0(T) \tag{4.6}$$

Using equation 4.6 the parameters a and ε can be estimated from the measured pressure-composition isotherms. The partial molar enthalpy of formation:

$$\Delta\bar{H}_H = \frac{\bar{H}_{H,\beta} - \bar{H}_{H,\alpha}}{x_\beta - x_\alpha} - \frac{1}{2}\bar{H}_{H_2} \tag{4.7}$$

is given by:

$$\Delta\bar{H}_H = \frac{1}{2}(2\varepsilon + a - \varepsilon_{H_2}) \tag{4.8}$$

where $\bar{H}_{H,\alpha}$ and $\bar{H}_{H,\beta}$ are the enthalpy of solution of hydrogen in the low-concentration α-phase and the concentrated β-phase, respectively.

However, in the two-phase region $\ln p$ is not described correctly by equation 4.6 as can be seen from the dashed line in Figure 4.5, which does not show a plateau pressure as is experimentally observed in the two-phase region. In order to obtain the physical solution, the so called Maxwell's equal-area construction has to be applied. For that, we consider only the x-dependent part of equation 4.6:

$$y = 2\ln\left(\frac{x}{1-x}\right) + \frac{2ax}{kT} \tag{4.9}$$

y is an odd function of $x - 0.5$ with $y(0.5)$=a/kT. The areas of $y - a/kT$ above and below the y-axis are equal. The boundaries of the two-phase region x_α and x_β can be calculated using:

$$y - a/kT = 0; \qquad \ln\left(\frac{x_{\alpha\backslash\beta}}{1-x_{\alpha\backslash\beta}}\right) = \frac{a}{kT}\left(0.5 - x_{\alpha\backslash\beta}\right) \tag{4.10}$$

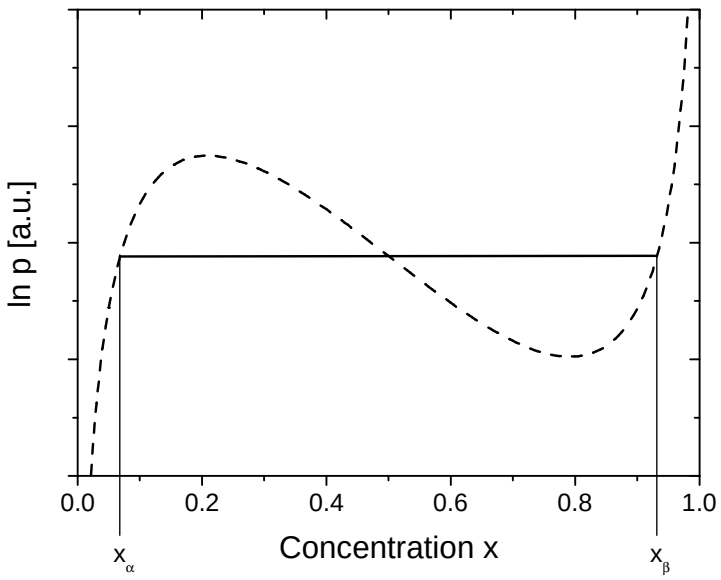

Figure 4.5: Schematic pressure-composition isotherm. The dashed line represents equation 4.6, which does not describe the pressure-composition isotherm correctly in the two-phase region, i.e. $x_\alpha < x < x_\beta$. The plateau pressure is indicated properly by the solid line.

Which implicitly gives the solubility line:

$$T = \frac{a\,(0.5 - x_\alpha)}{k \ln\left(\frac{x_\alpha}{1-x_\alpha}\right)} \tag{4.11}$$

So, for $x_\alpha < x < x_\beta$ the pressure is constant and given by:

$$x = \frac{1}{2}; \qquad \ln(p) = \frac{2\varepsilon + a - \varepsilon_{H_2}}{kT} + \ln(p_0(T)) \tag{4.12}$$

Now we can estimate from equation 4.6 the hydrogen concentration in the metal hydride as a function of temperature. For $x < x_\alpha$ and $x > x_\beta$ the hydrogen concentration in the metal-hydride layer as a function of temperature is implicitly given by equation 4.6. Instead of solving it numerically to obtain $x = x(T, p)$ it is much simpler to calculate $T = T(x, p)$, with:

$$T(x,p) = \frac{\varepsilon - \frac{1}{2}\varepsilon_{H_2} + ax}{\frac{1}{2}k \ln\left(\frac{p}{p_0(T)}\right) - k \ln\left(\frac{x}{1-x}\right)} \tag{4.13}$$

which is schematically represented in Figure 4.6.

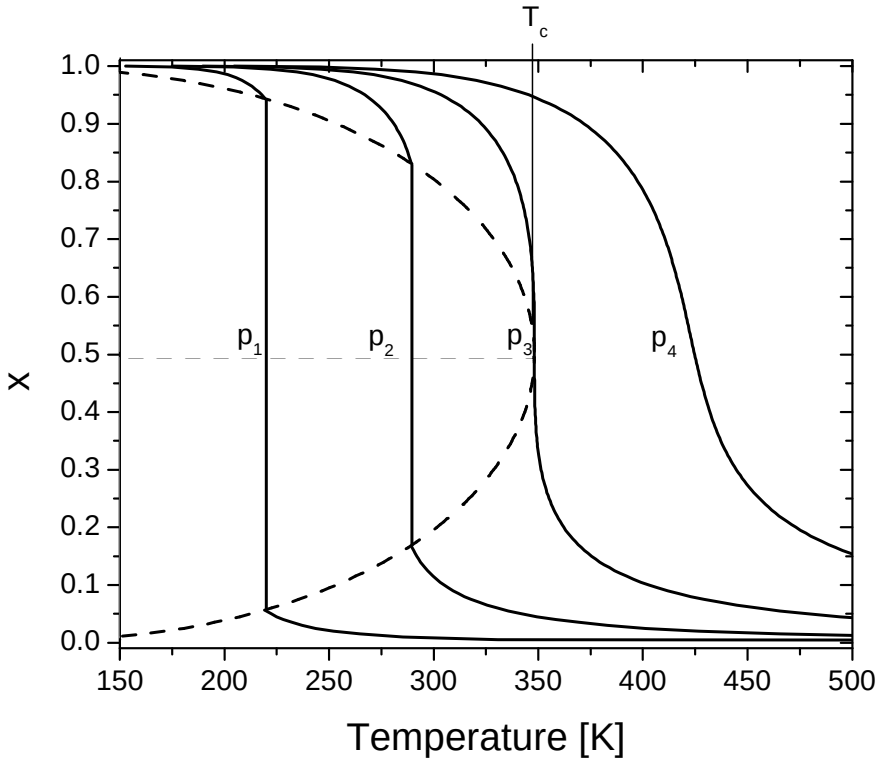

Figure 4.6: Schematic representation of the concentration of hydrogen x_M in a metal-hydride layer of a gas cell device as a function of temperature as given by equation 4.13 at different hydrogen pressures with $p_1 < p_2 < p_3 < p_4$. If the initial temperature and pressure are chosen in such a way that the hydrogen concentration is just above the plateau pressure, the change in concentration upon temperature increase is largest. The dashed line represents the solubility line of equation 4.11. The critical temperature T_c is indicated.

Equation 4.6 provides us insight to enhance the thermochromic effect of a gas cell device, which starts with optimizing the change in the amount of hydrogen in the metal hydride as a function of temperature. Evidently, the largest change in the amount of hydrogen upon temperature increase is observed when a pressure is applied, which is just above the plateau pressure. This plateau pressure is a function of temperature. Since for practical reasons the working temperature should be between room temperature and 100°C and the pressure between 10^{-3} and 1 bar, the enthalpy of formation ΔH of the metal hydride used in the thermochromic gas cell device should be around -23 kJ/mol H. Since the metal hydride should have a plateau in the considered region, the critical temperature should be higher than room temperature. Therefore the H-H interaction coefficient a should be more

negative than -0.10 eV, since the critical temperature is given by $T_c = -a/(4k)$. Since the two-phase region increases with increasing difference between the working temperature and the critical temperature, $T_c - T$, a should be as much negative as possible.

In these calculations the gas pressure increase due to a temperature increase of the gas is not taken into account. Also, we did not take into consideration the pressure increase due to the hydrogen released from the metal-hydride layer. For a double-glassed window with a Mg-Ni switchable mirror layer covered with a 5 nm Pd layer, separated 1 cm from the other window, a hydrogen gas pressure of 5 mbar will increase by about 15 % when the temperature is raised from room temperature to 70°C. This is primarily due to the expansion of the hydrogen gas.

4.2.2 All-solid-state device

The all-solid-state thermochromic device consists of two hydrogen absorbing layers, i.e. a hydrogen reservoir layer and a switchable mirror capped with a hydrogen impermeable layer (see Figure 4.2). Initially the reservoir layer as well as the switchable mirror are partly hydrogenated and are in thermodynamical equilibrium. In the all-solid-state device the thermochromic effect is caused by a rearrangement of the hydrogen between the constituent metal-hydride layers upon changing temperature. This is due to a different temperature dependence of the chemical potential of hydrogen in the reservoir and in the switchable mirror. The hydrogen redistribution (see Figure 4.3) causes a change in the optical appearance of the switchable mirror. We discuss here how the characteristic shape of the chemical potential curves, as well as their temperature response, influences the hydrogen rearrangement. In this way we identify the thermodynamic properties required for the bilayer of the device. The optimization of the performance of the all-solid-state thermochromic device is obtained from a quantitative model describing the chemical potential of the layers involved. Finally, the effect of a difference in the entropy between the layers is discussed.

For the all-solid-state thermochromic device, two conditions should be fulfilled. Firstly, the hydrogen in both materials should stay in thermodynamical equilibrium with each other, i.e. they should have the same chemical potential also at all temperatures, $\mu_{H,A} = \mu_{H,B}$. Secondly, the total amount of hydrogen should stay constant. As the quantity of hydrogen is fixed due to the hydrogen impermeable cap layer, the hydrogen which is desorbed by one layer will be absorbed by the other and vice versa. For simplicity we take the number of available H sites in layer A and B equal, i.e. $N_A = N_B$. Layer A is assumed to have the most negative heat of formation ΔH, i.e. the hydrogen concentration x_A in layer A is always higher than x_B at the same chemical potential.

Figure 4.7 shows how the thermochromic effect functions in terms of the induced change in hydrogen concentration in layer A and B. Although a description in terms of hydrogen pressure as depicted in Figure 4.3 would seem more appealing, rewriting the thermodynamic equilibrium in terms of hydrogen pressure instead of chemical

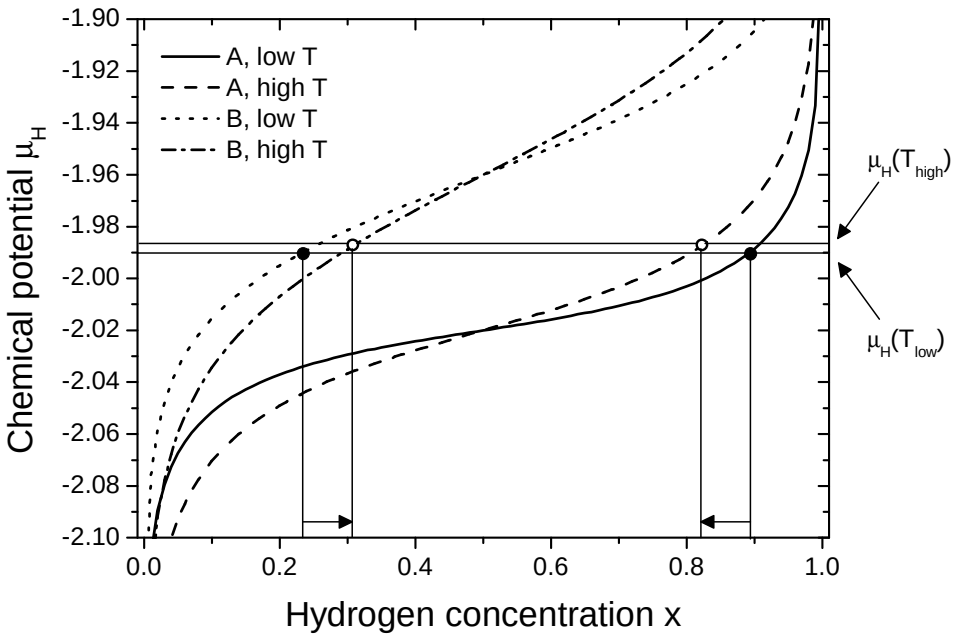

Figure 4.7: Schematic representation of the hydrogen redistribution in an all-solid-state device with a typical combination of two different materials. The chemical potential $\mu_H(T_{low})$ at low temperature is chosen arbitrarily. To preserve thermodynamical equilibrium, the chemical potential of both materials is always equal $\mu_{H,A} = \mu_{H,B}$ at any temperature. Moreover, the total amount of hydrogen in the device is conserved. Therefore, a change in temperature causes a shift in the chemical potential of both materials to such a level that the total amount of hydrogen is conserved. This causes a redistribution of the hydrogen over the two layers A and B (indicated by the arrows). It should be noted, that the number of available H sites in layer A and B is taken equal, i.e. $N_A = N_B$, therefore the increase of x_A is equal to the decrease in x_B.

potential would make the discussion more complex. From equations 4.5 and 4.6 it can be seen that the chemical potential is related to the pressure by $\mu_H \propto T \ln p$, which makes a discussion on the temperature dependence of the hydrogen concentration based on the hydrogen pressure unnecessarily complicated. It should be noted, that Figure 4.7 illustrates the case in which both isotherms do not exhibit a plateau, i.e. they are above their critical temperature T_c. First we only consider material A. When the temperature is increased, the chemical potential as a function of hydrogen concentration becomes steeper as a result of the entropic term $kT \ln \frac{x}{1-x}$. The amount of hydrogen release or uptake upon a change in temperature at constant chemical potential depends on the initial hydrogen concentration, e.g. at x_A=0.5 ($\mu_{H,A}$=-2.02 eV) no change in hydrogen concentration x_A is induced in layer A upon a temperature increase, while at x_A=0.1 ($\mu_{H,A}$=-2.05 eV) the change is relatively

large. Now we consider both materials. Then, we have to take into account the conditions mentioned above, i.e. the chemical potential of the hydrogen in both materials should stay equal and the total amount of hydrogen should not change. Let us first look at the chemical potential. For the sake of simplicity, we keep the chemical potential at the same value as at low temperature. Layer A would then absorb hydrogen, while layer B would desorb hydrogen. However, in most cases, the total amount of hydrogen desorbed by one layer would not be the same as absorbed by the other. Therefore, the chemical potential is increased up to the level indicated in Figure 4.7 in order to fulfill both conditions. The amount of desorbed hydrogen of layer B is now limited by the absorption capacity of layer A. We observe that a large change in hydrogen concentration x can be induced if both chemical potentials exhibit a large change in concentration x at the same chemical potential. However, if one of the materials has a small change, it limits the change in concentration of the other material, since the hydrogen desorbed by one material should all be absorbed by the other.

For a more quantitative description we introduce now a somewhat simplified model (see Figure 4.8), which has two advantages. Firstly, it is simplified in such a way that it is analytically solvable, but still incorporates most of the necessary features. Secondly, it describes a combination of chemical potentials which induces the highest possible hydrogen redistribution. In the model we assume a chemical potential $\mu_{H,S}$ of the switchable layer, which is independent of concentration and temperature. This corresponds to a plateau over the entire concentration range and describes the equilibrium between a metal and its hydride both without any solubility range (Figure 4.8). As a result, a temperature change induces the maximum change in H-concentration in the reservoir material R, since the plateau of material S will not limit the hydrogen redistribution and freely absorbs or desorbs hydrogen. It should be noted, that the height of the plateau in relation to the chemical potential curve of material R is very important, since it determines the amount of redistributed hydrogen. To obtain the largest change in hydrogen concentration it should be chosen in such a way that the change of the chemical potential R upon a temperature change is largest near the plateau of material S.

Now that we roughly determined the optimal conditions for a large hydrogen rearrangement upon changing temperature, we quantitatively determine the following thermodynamic parameters by means of our simplified model: the initial hydrogen concentration, the difference between ΔH of the two combined materials and the ratio of the thicknesses of both layers, here expressed by the ratio of the amount of interstitial sites for hydrogen available in either of the materials.

We describe the layers in terms of their chemical potential. Hydrogen in layer R, which represents the hydrogen reservoir layer, is assumed to have a chemical potential $\mu_{H,R}$ given by:

$$\mu_{H,R} = kT \ln \frac{x_R}{1 - x_R} + \varepsilon_R + a_R x_R \tag{4.14}$$

Here, we assume the temperature to be above the critical temperature T_c, avoiding the need to use the Maxwell construction as explained in the former paragraph

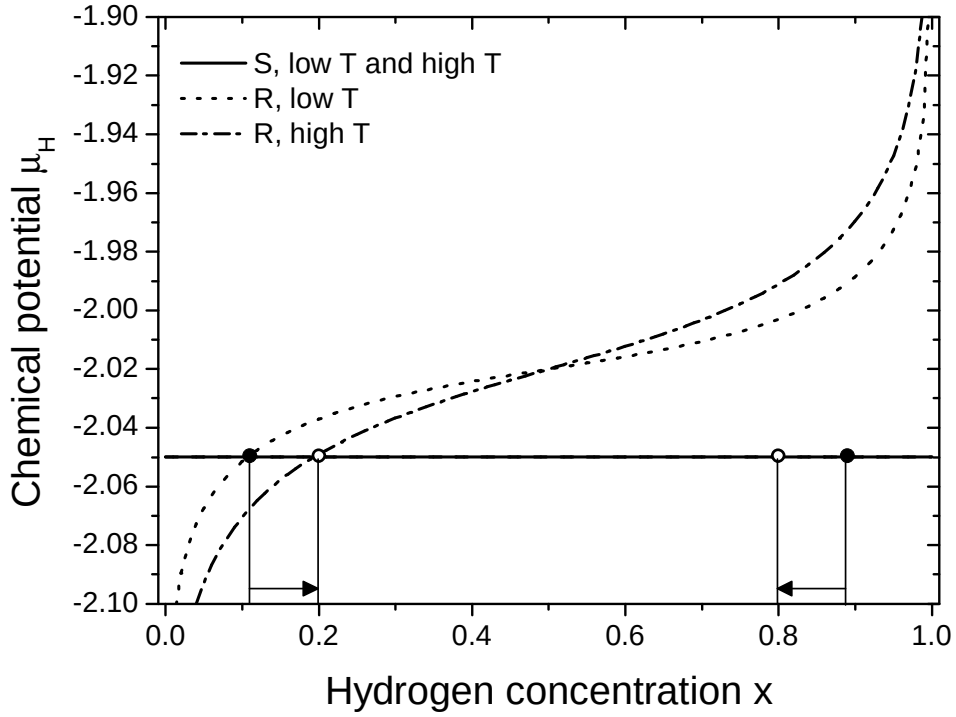

Figure 4.8: Schematic representation of the hydrogen redistribution in an all-solid-state device with the chemical potentials used in our quantitative model. One of the chemical potential curves of Figure 4.7 is replaced by a horizontal line which represents a broad plateau independent of temperature. It should be noted, that the change in concentration of the reservoir material R is not limited by the switchable material S which freely absorbs hydrogen. Observe as well that the amount of hydrogen redistribution depends critically on the relative position of the two isotherms, i.e. on $\varepsilon_S - (\varepsilon_R + a_R/2)$.

and sketched in Figure 4.5. Therefore, the H-H interaction term a_R is restricted to $-a_R = 4kT_c$, with $T_c < 293K$. Layer S, the switchable mirror, is assumed to have a broad plateau extending from x_S=0 to x_S=1, with

$$\mu_{H,S} = \varepsilon_S \tag{4.15}$$

In thermodynamical equilibrium, the chemical potentials $\mu_{H,R}$ and $\mu_{H,S}$ of hydrogen in the layers R and S are equal:

$$\mu_{H,R} = \mu_{H,S} \tag{4.16}$$

Combining equation 4.16 with equations 4.14 and 4.15 gives:

$$\varepsilon_S - \varepsilon_R = kT \ln\left(\frac{x_R}{1 - x_R}\right) + a_R x_R \tag{4.17}$$

To optimize the change in concentration x_S in the switchable mirror upon a temperature change, dx_S/dT should be maximized. This implies optimizing dx_R/dT of the reservoir, since the total amount of hydrogen in the bilayer is constant and therefore all hydrogen leaving the switchable mirror migrates into the reservoir and vice versa.

$$\frac{d}{dT}\left(\varepsilon_S - \varepsilon_R\right) = \frac{d}{dT}\left[kT\ln\left(\frac{x_R}{1-x_R}\right) + a_R x_R\right] \tag{4.18}$$

Since ε_S and ε_R are assumed to be constant this results into:

$$k\ln\left(\frac{x_R}{1-x_R}\right) + kT\frac{1}{x_R\left(1-x_R\right)}\frac{dx_R}{dT} + a_R\frac{dx_R}{dT} = 0 \tag{4.19}$$

and

$$T\frac{dx_R}{dT} = -\left[\frac{\ln\left(\frac{x_R}{1-x_R}\right)}{\left(\frac{1}{x_R(1-x_R)} - \frac{4T_c}{T}\right)}\right] \tag{4.20}$$

Figure 4.9 shows the temperature dependence of the hydrogen concentration in the reservoir predicted by equation 4.20 for various H-H interactions a_R. At low (high) initial hydrogen concentration x_R, the reservoir absorbs (desorbs) hydrogen upon a temperature increase, as dx_R/dT is positive (negative). Since the switchable mirror is assumed to have a plateau extending from x=0 to x=1, the initial hydrogen concentration in the reservoir is determined by the relative height of the plateau compared to the pressure-composition isotherm of the reservoir and is thus determined by $\varepsilon_S - (\varepsilon_R + a_R/2)$ (see Figure 4.10). If hydrogen in the switchable mirror is more stable than in the reservoir, i.e. $\varepsilon_S - (\varepsilon_R + a_R/2) < 0$, the plateau of the switchable mirror crosses the pressure-composition isotherm of the reservoir at low hydrogen concentration $x_R < 0.5$ and the change in hydrogen concentration dx_R/dT is positive (see Figure 4.9). However, if the hydrogen in the reservoir is more stable than in the switchable mirror, the hydrogen concentration in the reservoir is high $x_R > 0.5$ and decreases upon a temperature increase.

To find the optimal conditions for hydrogen migration from one layer to the other, we first consider the H-H interaction a_R. Figure 4.9 shows that the more negative a_R, the larger the minimum and maximum values of the difference in hydrogen concentration upon temperature increase dx_R/dT. This seems to be preferred at first sight. However, let us consider the difference between the enthalpies of formation of both layers $\varepsilon_S - (\varepsilon_R + a_R/2)$. The optimum amount of hydrogen in the reservoir is x_R=0.18 or x_R=0.82 for a_R=0. Using equation 4.17 gives $\varepsilon_S - \varepsilon_R$=-0.038 eV and +0.038 eV at room temperature, respectively, which corresponds to a difference in ΔH of -3.7 and +3.7 kJ/mol H. For $a_R = -3kT$ the amount of hydrogen in the reservoir is x_R=0.29 or x_R=0.71 which gives $\varepsilon_S - (\varepsilon_R + a_R/2)$=-0.0067 eV and +0.0067 eV at room temperature, respectively, corresponding to a difference in ΔH of -0.6 and +0.6 kJ/mol H (see equation 4.8). This implies that the switchable mirror and the reservoir must have very similar enthalpies, which might be rather difficult to achieve in a practical device.

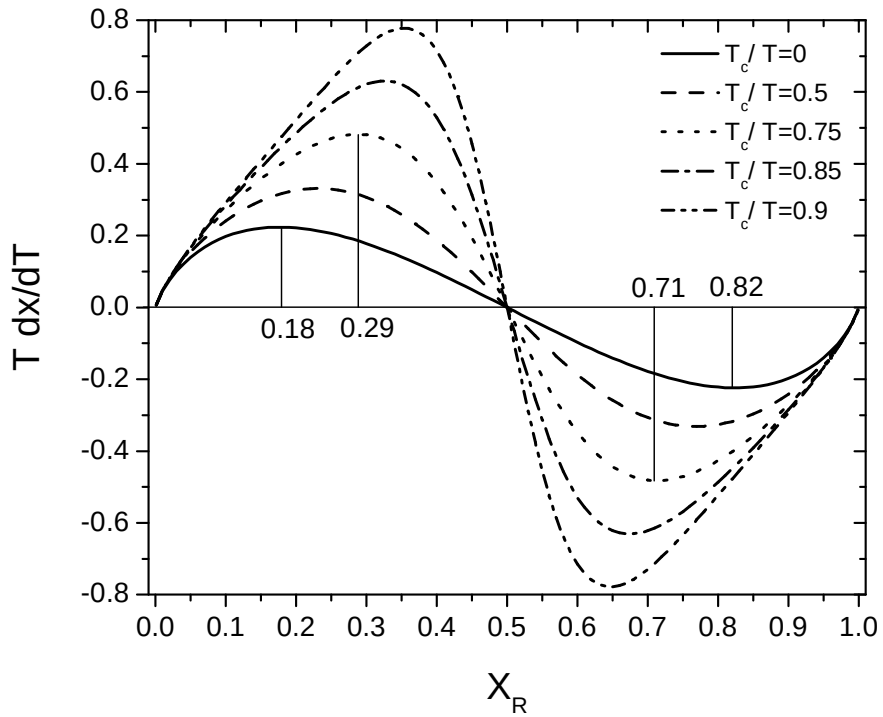

Figure 4.9: Temperature dependence of the H concentration in the reservoir layer for various ratios of T_c/T, i.e. for various strength of the H-H interaction parameter a_R, since $T_c = \frac{-a_R}{4k}$. The more negative a_R, the larger the minimum and maximum values of the difference in hydrogen concentration upon temperature increase dx_R/dT.

We look now more closely at the thicknesses of the layers, or the number of available H-vacancies of the materials present and the initial hydrogen concentration of both layers. In a sealed bilayer consisting of a reservoir layer R and a switchable mirror S, the total amount of hydrogen N_{Htot} is constant and equal to the sum of the hydrogen content in layer R and S, i.e.:

$$N_{Htot} = x_R N_R + x_S N_S \tag{4.21}$$

where $x_{R,S}$ is the concentration of hydrogen in layer R or S varying between $x = 0$ and $x = 1$ and $N_{R,S}$ is the number of interstitial sites that can be occupied in material R or S. The relative amount of relevant hydrogen interstitial sites in the reservoir layer R is:

$$y \equiv \frac{N_R}{N_R + N_S}; \qquad \frac{N_S}{N_R + N_S} = 1 - y \tag{4.22}$$

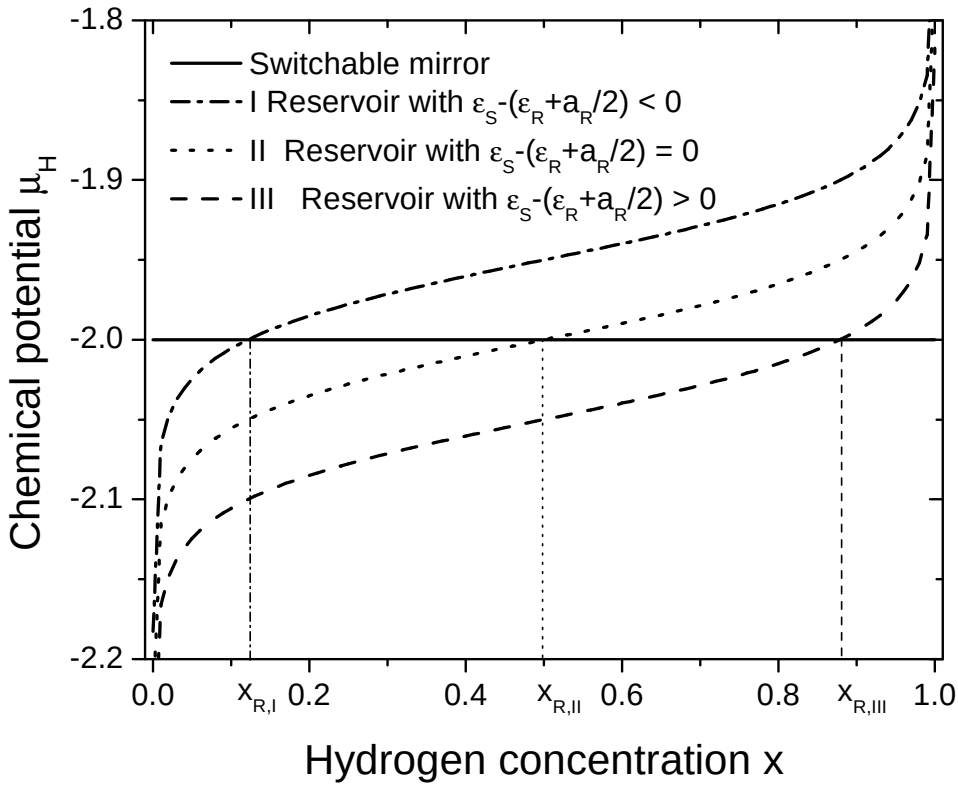

Figure 4.10: Chemical potential μ_H of the switchable mirror S and the reservoir layer R showing the dependence of the initial hydrogen concentration in the reservoir layer on the difference between the enthalpies of both layers. If $\varepsilon_S - (\varepsilon_R + a_R/2) < 0$ the plateau of the switchable mirror crosses the pressure-composition isotherm of the reservoir at low hydrogen concentration $x_{R,I} < 0.5$ and the change in hydrogen concentration dx_R/dT is positive. However, if hydrogen in the reservoir is more stable than in the switchable mirror, the hydrogen concentration in the reservoir is high $x_{R,III} > 0.5$ and decreases upon a temperature increase. The chemical potential $\mu_{H,S} = -2.0$ of the switchable mirror is chosen arbitrarily.

The average concentration of hydrogen $\bar{x}$ in the bilayer is given by:

$$\bar{x} = yx_R + (1-y)x_S \tag{4.23}$$

Which gives for the hydrogen concentration x_R in the reservoir layer:

$$x_R = \frac{\bar{x} - (1-y)x_S}{y} \tag{4.24}$$

At thermodynamic equilibrium (equations 4.14, 4.15 and 4.16) follows that:

$$kT \ln \frac{x_R}{1-x_R} + \varepsilon_R = \varepsilon_S \tag{4.25}$$

Which can be rearranged into:

$$x_R = \frac{1}{e^{-\frac{\varepsilon_S - \varepsilon_R}{kT}} + 1} \tag{4.26}$$

However, we are not so much interested in the change of hydrogen concentration in the reservoir layer. Of interest is the temperature dependence of the optical properties of the switchable mirror, which is proportional to the hydrogen concentration x_S. Using equations 4.24 and 4.26 gives:

$$x_S = \frac{\bar{x} - \left[\frac{y}{e^{\frac{\varepsilon_R - \varepsilon_S}{kT}} + 1}\right]}{1-y} \tag{4.27}$$

To switch from absorbing to reflecting, the hydrogen concentration in the switchable mirror layer should be high at low temperatures and low at high temperatures. Hence, the hydrogen must migrate from the switchable mirror layer to the reservoir layer upon a temperature increase. Therefore, the switchable mirror has to have a larger negative enthalpy of hydride formation as compared to the reservoir, i.e. $\varepsilon_R - \varepsilon_S > 0$. This can be checked by estimating the hydrogen concentration x_S in the switchable mirror by using equation 4.27. If $\varepsilon_R - \varepsilon_S > 0$, then at low temperature x_S is high and at high temperature x_S is low.

With equation 4.27 we find that the larger the amount of hydrogen interstitial sites in the reservoir layer as compared to the switchable mirror layer, the larger the amount of migrated hydrogen upon a temperature change, i.e. $y \to 1$, because of two reasons. Firstly, in the numerator y multiplies the temperature dependent term. Secondly, the $\frac{1}{1-y}$ is large when $y \to 1$.

Now we only need to know the optimal average hydrogen concentration $\bar{x}$. At high temperature, when the hydrogen concentration x_S in the switchable mirror should be low, $x_S = \bar{x} - \frac{y}{2}/(1-y)$. Taking $x_S = 0$ this leads to an average hydrogen concentration $\bar{x}$ of $\bar{x} = \frac{y}{2}$. At low temperature, $x_S = \bar{x}/(1-y)$. Since we must always have $x_S \leq 1$, this leads to the restriction for the relative amount of hydrogen interstitial sites y in the reservoir layer of $y < \frac{2}{3}$.

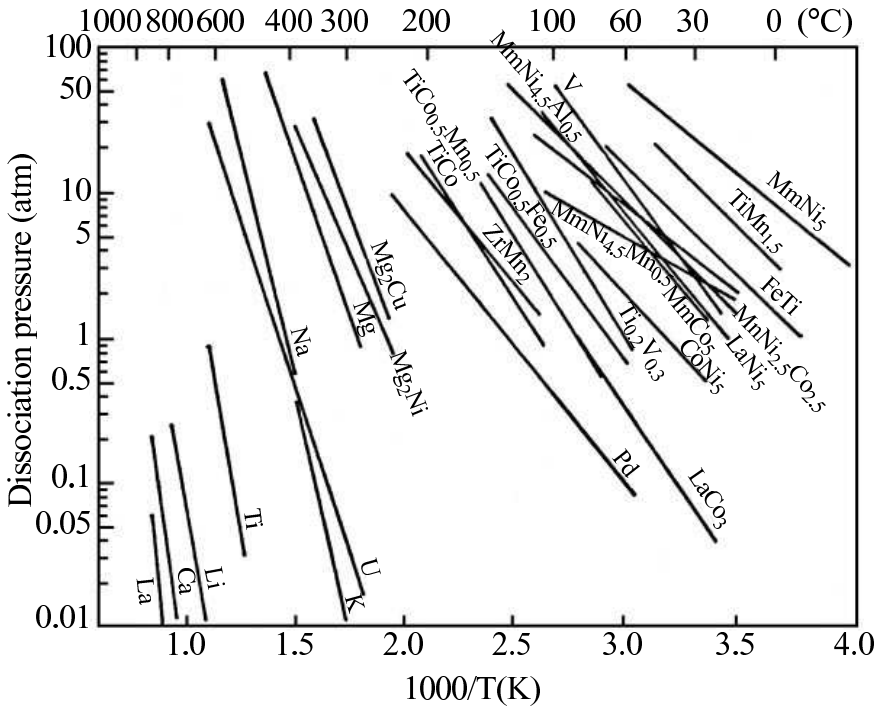

Figure 4.11: Van 't Hoff plots of the temperature dependence of the plateau dissociation pressure for various hydrides [20].

The model described above has some limitations. Firstly, the switchable mirror is assumed to have a broad plateau. Therefore, if the switchable mirror is in its one-phase region, i.e. not at the plateau, the model is not applicable and we should switch to a much more complicated model. Secondly, the entropy of formation ΔS_{H_2} is considered equal for both materials. The entropy loss of the gaseous hydrogen upon absorption by the metal is $\Delta S^0_{H_2}$=-130.8 J/K mole H_2 and is by far the largest contribution to the entropy of formation ΔS_{H_2}. Other (excess) entropy terms, e.g. the non-ideal configurational entropy, however, may be different. If the entropy of formation of the switchable mirror and the reservoir layer would be the same, then in a Van 't Hoff plot (see Figure 4.4) where the logarithm of the equilibrium plateau pressure is plotted against the reciprocal temperature, the isoconcentration lines of the two different layers never cross, since ΔS and therefore the intercept with the axis is the same. However, as can be seen from Figure 4.11, in which the Van 't Hoff plots of plateau pressures of various materials are presented, some isoconcentration lines do cross, indicating that this in not always true. A difference in entropy would result into an extra temperature dependent term of the chemical potential. The chemical potential curve of layer R in Figure 4.8 would then not only become steeper, but

would shift up upon a temperature increase. We note however, that this is rare and that none of the crossing isoconcentration lines include switchable mirrors.

4.3 Results

In the former paragraph we discussed the thermodynamic properties needed to make a thermochromic device with a high optical contrast between low and high working temperatures. For a gas cell device we derived that the optically active layer needs to have a broad range of plateau pressures and that the applied hydrogen pressure should be just above the plateau. From a practical point of view, this amounts to a material with a low critical temperature T_c and a plateau pressure between 10^{-4} and 1 bar around room temperature, i.e. with an enthalpy of hydride formation ΔH between -30 kJ/mol H and -19 kJ/mol H. For the all-solid-state device one of the layers should have a plateau. This plateau pressure should be the hydrogen pressure to which the device is exposed before it is sealed with the hydrogen impermeable cap layer. The other component of the bilayer should have a very similar ΔH and should have a critical temperature T_c just below room temperature.

In this paragraph we have chosen several thermochromic devices which fulfill most of the above mentioned criteria. We calculated the expected change in hydrogen concentration upon a temperature change based on equations of the former paragraph. Combined with measurements of the optical properties as a function of hydrogen concentration we obtain the optical properties as a function of temperature. These estimates are then compared with the experimental results of the thermochromic devices.

4.3.1 Mg-Ni gas cell device

Since the plateau pressure of Mg-Ni is about $p = 4 \cdot 10^{-4}$ bar, it might be applied in a thermochromic gas cell device. However, the optical transitions in these materials are quite complex. In addition to a shiny metallic state at low hydrogen concentrations and a transparent state when fully loaded to Mg_2NiH_4, Mg_2NiH_x exhibits a third optical state at intermediate hydrogen concentrations [6]. In this state, reflection is low (R $<$ 25%) and transmission is negligible (T $<$ 0.01%) over the entire visible spectrum, hence the film appears black. The origin of this unusual state lies in the hydrogenation mechanism of the film: the nucleation of the hydrogen rich phase starts in an approximately 30 nm thick layer close to the film-substrate interface and not, as intuitively expected, close to the Pd cap layer [21]. For achieving the black state, only a hydrogen concentration change in the first 30 nm is necessary. Therefore, Mg_2NiH_x can be used as the active layer of a device that changes its optical appearance from black to reflecting by a relatively small reduction of its hydrogen content. Specifically, for a 200 nm Mg_2NiH_x film to be in the black state, the average hydrogen concentration equals [H]/[Mg_2Ni]=0.8 (30 nm of Mg_2NiH_4 and 170 nm of $Mg_2NiH_{0.3}$). When Mg_2Ni absorbs hydrogen it forms first a dilute solution up to $Mg_2NiH_{0.3}$. At higher concentrations the Mg_2NiH_4 phase nucleates

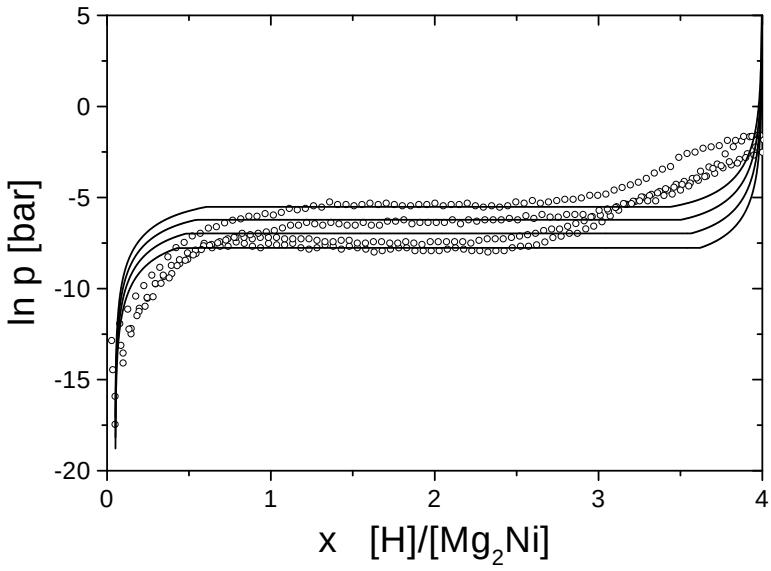

Figure 4.12: Pressure-composition isotherms of a 200 nm thick $Mg_{1.8}NiH_x$ film at 20, 30, 40 and 50°C (from bottom to top). The experimental isotherms are determined electrochemically [22]. The saturation of the isotherms near [H]/[Mg_2Ni]=4 is due to H_2 evolution during electrolytic charging. The full lines are obtained from equation (4.6) and the values of the parameters are ε_{Mg_2Ni}=-2.42 eV and a_{Mg_2Ni}=-0.14 eV.

and there is a coexistence of Mg_2NiH_4 and $Mg_2NiH_{0.3}$. To describe the pressure-composition isotherms of Mg_2NiH_x, we use our simple lattice gas model, although the crystal structure of $Mg_2NiH_{0.3}$ and Mg_2NiH_4 have different symmetries.

We obtain ε_{Mg_2Ni}=-2.42 eV and a_{Mg_2Ni}=-0.14 eV from a fit of Mg_2NiH_x isotherms [22] using equation 4.6 as described in paragraph 4.2. The measured and fitted isotherms are shown in Fig. 4.12. Note that 1 eV corresponds to 96.49 kJ/mol H, giving ΔH_{Mg_2Ni}=-25.1 kJ/mol H. Using these parameters the amount of hydrogen in the Mg_2NiH_x-layer can now be estimated at various temperatures when the initial hydrogen pressure is known. Starting at room temperature just above the plateau pressure at $p = 4 \cdot 10^{-4}$ bar and increasing the temperature by 100 degrees results in a concentration change from $x = 0.94$ to $x = 0.01$, i.e. from [H]/[Mg_2Ni]=3.76 to [H]/[Mg_2Ni]=0.05 (see Figure 4.13). The reflection then changes from 16% through the black state at 10% to 59% at a wavelength of 1.25 eV.

Note, that the black state is not a stable state in the gas cell device and therefore only applications which require a change between the transparent and reflecting state

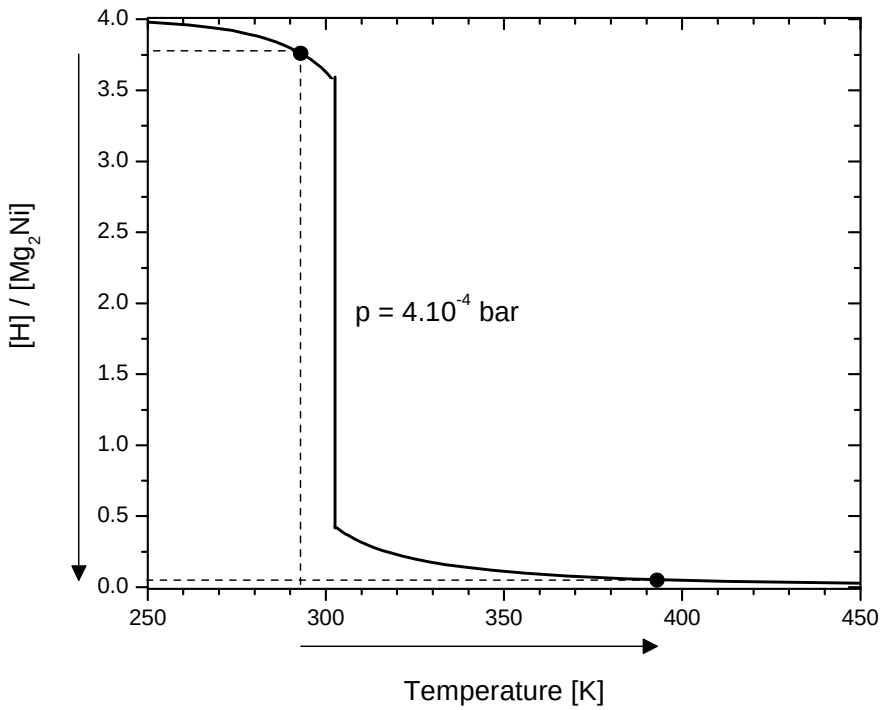

Figure 4.13: Hydrogen concentration [H]/[Mg_2Ni] in a Mg_2Ni gas cell device as a function of temperature at a hydrogen pressures of $p = 4 \cdot 10^{-4}$ bar. When the temperature is raised by 100 degrees from room temperature, the hydrogen concentration in the Mg_2Ni layer changes from [H]/[Mg_2Ni]=3.76 to [H]/[Mg_2Ni]=0.05.

find benefit from the gas cell geometry.

In Fig. 4.14 preliminary experimental results are presented of a thermochromic gas cell device consisting of a sputtered 30 nm sputtered Mg_2Ni thin film capped by 50 nm Pd. The reflection is monitored through the transparent substrate After hydrogenation, the sample is subjected to a flow of 250 ml/m of 0.4 % H_2 and 1 % O_2 in Ar. The addition of oxygen enhances catalytic desorption of hydrogen at the Pd surface [23–25] and probably reduces the hydrogen partial pressure. Without the addition of oxygen, too high temperatures were needed to dehydrogenate the sample, causing deterioration of the sample which prevented rehydrogenation. As the temperature is raised inside the gas mixture environment, the reflection of the sample goes back to the reflecting state. Upon cooling, the sample absorbs hydrogen again up to the transparent state. The reversibility of the process indicates the possibility of a gasochromic Mg-Ni device.

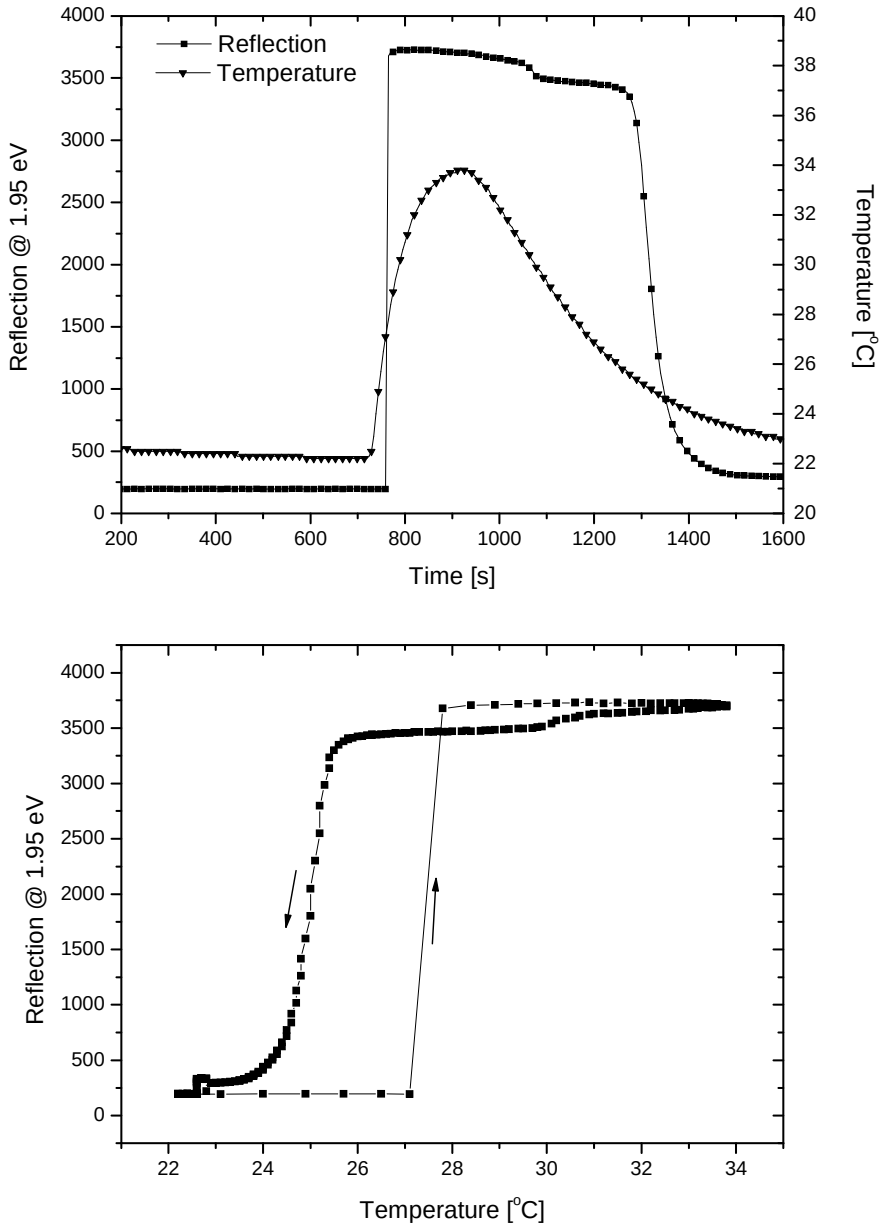

Figure 4.14: Experimentally measured thermochromic effect of a 30 nm thick Mg_2Ni thin covered with 50 nm Pd. The gas cell device is heated under a flow of 250 ml/min of 0.4 % H_2 and 1 % O_2 in Ar from room temperature to 35°C causing the reflection to increase back to the dehydrided state. Upon cooling the sample absorbs hydrogen again as can be seen from the drop in reflection.

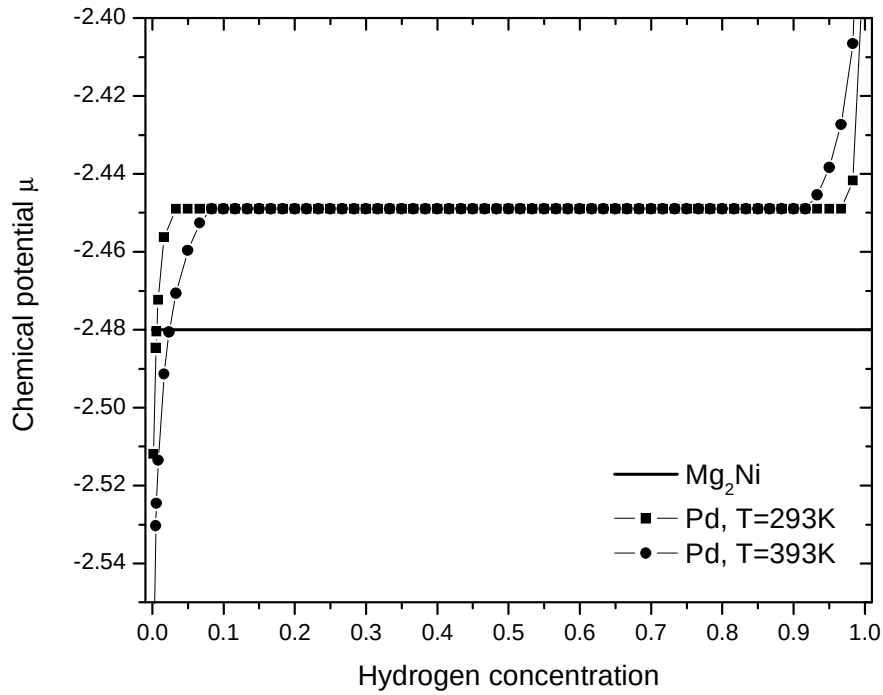

Figure 4.15: Chemical potentials of Mg-Ni and Pd as given by equations 4.28 and 4.29 at room temperature and elevated temperature. The change in hydrogen concentration is $\Delta x_{Pd} = \Delta x_{Mg-Ni}$=0.011. Note that this is only true if the amount of available H interstitial sites is the same for Pd and Mg-Ni. The concentration change upon a temperature change can be enhanced by increasing the amount of Pd as compared to Mg-Ni.

4.3.2 Mg_2Ni/Pd all-solid-state device

Since the plateau pressures of Pd and Mg_2Ni thin films are not too different and Mg_2Ni has a broad plateau at hydrogen pressures where the Pd is outside its plateau region, the Mg_2Ni-Pd bilayer seems a good candidate to test our all-solid-state thermochromic device.

To predict the thermochromic effect in the Mg_2Ni/Pd all-solid-state device, we use the equations derived in paragaph 4.2.2. For PdH_x we use a_{Pd}=-0.20 eV [18] and ε_{Pd}=-2.35 eV, obtained from a fit of PdH_x isotherms [26] in the required temperature and pressure region. Note that 1 eV corresponds to 96.49 kJ/mol H, giving ΔH_{Pd}=-21.2 kJ/mol H. The chemical potential $\mu_{H,Pd}$ is according to equation 4.14 given by:

$$\mu_{H,Pd} = kT \ln \frac{x_{Pd}}{1 - x_{Pd}} - 2.35 - 0.20 x_{Pd} \tag{4.28}$$

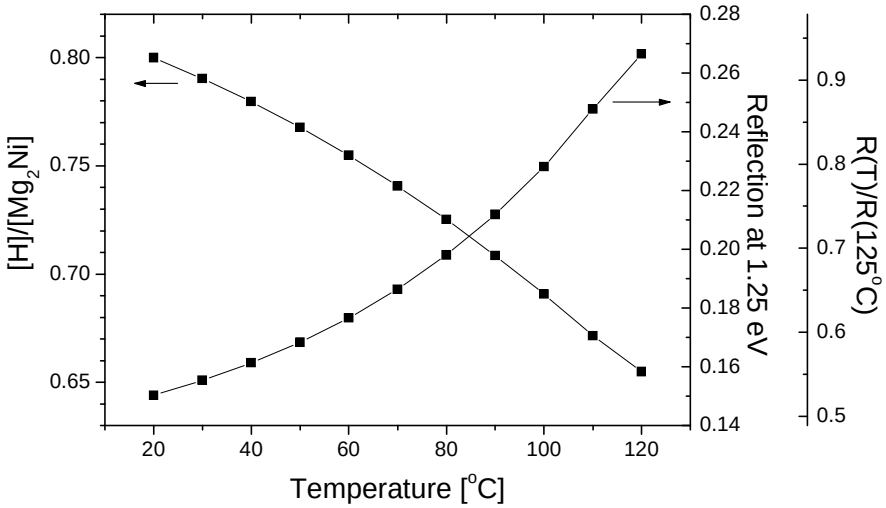

Figure 4.16: Calculated change in concentration in the Mg_2NiH_x layer of a 200 nm Mg_2Ni/3000 nm Pd bilayer as a function of temperature together with the accompanying change in normalized reflection at a photon energy of 1.25 eV as taken from [22]. Note that since the molar volume of Pd and Mg_2Ni is 8.56 and 31.2 cm^3, respectively, and the amount of relevant H interstitial sites is 0.6 and 4, the ratio of the H interstitial sites in this case is N_{Pd}/N_{Mg_2Ni}=8.2

whereas the chemical potential μ_{H,Mg_2Ni} is given by (see equation 4.15):

$$\mu_{H,Mg_2Ni} = -2.48\ eV \tag{4.29}$$

since we consider only the plateau region of Mg_2Ni. The chemical potentials of both layers at room temperature and elevated temperature are plotted in Figure 4.15.

Using these chemical potentials the distribution of the hydrogen over the two metal-hydride layers can now be calculated at various temperatures and thickness ratios. At room temperature (RT) we want the bilayer to be in the black state. Hence, for a 200 nm layer, the initial average hydrogen concentration is fixed to $Mg_2NiH_{0.8}$. Since we prepare the bilayer at room temperature, x_{Pd} is fixed, leaving N_{Pd} (i.e. the number of interstitial site in Pd) as a free parameter. Figure 4.16 shows the calculated change of hydrogen concentration in the Mg_2NiH_x layer of a 200 nm Mg_2Ni/3000 nm Pd bilayer as a function of temperature. In the same figure, we include the expected change in reflection at a photon energy of 1.25 eV taking experimental data from Lohstroh *et al.* [22]. Increasing the temperature from 20 °C to 120 °C results in a reflection R increasing from 15% to 27%. Since the metal-hydride bilayer device is non-transparent, this is accompanied by a change in absorption $A = 1 - R$ from 85% to 73% at 1.25 eV. In comparison, the reflection of a 100 nm thick VO_x layer increases from ≈30% to ≈36% (at 1.25 eV) by heating the sample from 20 °C to 80 °C [1].

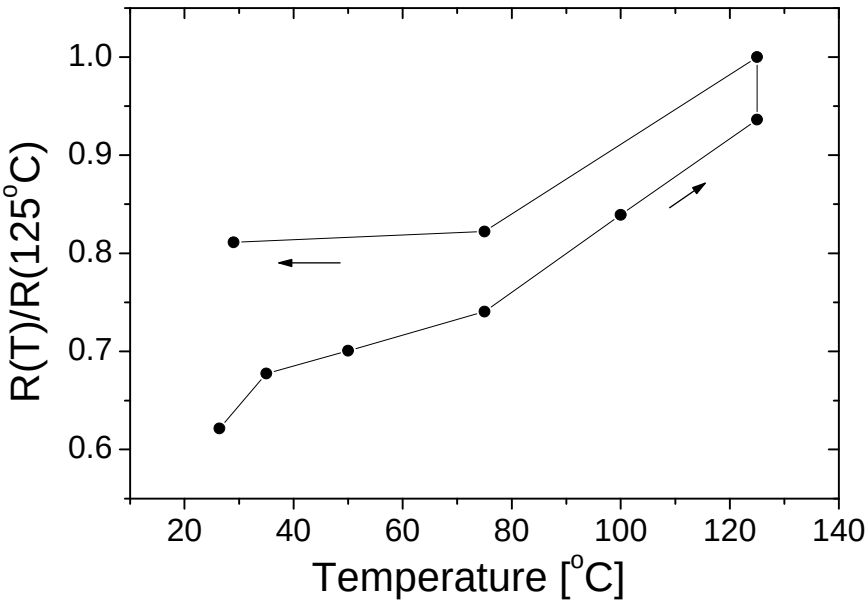

Figure 4.17: Average normalized reflection signal (channel green and blue) of the RGB camera at various temperatures through the substrate of an all-solid-state thermochromic device with Mg_2Ni (100 nm) as the switchable mirror, Pd (1500 nm) as the H reservoir layer and Cu as the H impermeable layer.

In Fig. 4.17 experimental results of a device consisting of a sputtered 100 nm Mg_2Ni/1500 nm Pd bilayer capped with 300 nm Cu are shown. The reflection was monitored in an optical microscope equipped with an RGB camera. The sample is viewed through the transparent substrate, hence we face the active switchable absorber layer. Before capping with Cu by pulsed laser deposition, the Mg_2Ni/Pd double layer is loaded with H approximately to the black state at RT. After deposition of the Cu, the sample still appears dark. In Fig. 4.17, we show the average signal (channel green and blue) of the RGB camera at different temperatures. As the temperature is raised, the reflection increases and the sample appears shiny metallic. Cooling down to RT the reflection decreases, although not completely back to the starting position. The experimental observation upon heating agrees well with the foregoing calculation. However, it should be noted that upon a second heating cycle, hardly any thermochromic effect was observed. Moreover, despite many attempts, the result shown in Figure 4.17 appeared irreproducible.

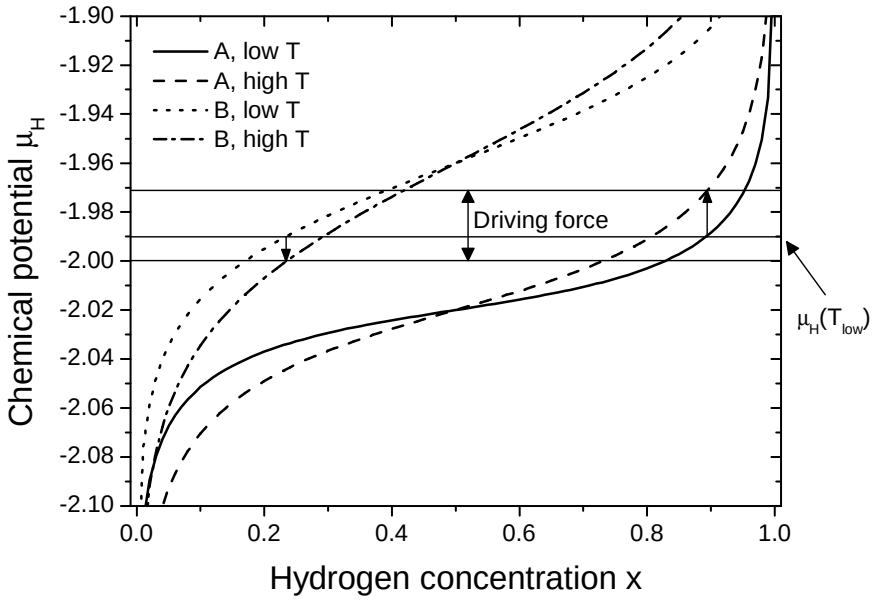

Figure 4.18: Schematic representation of a typical combination of chemical potentials of different materials. The initial driving force upon a temperature increase is indicated in the graph.

4.3.3 Other devices

Given the unreliability of the above mentioned device, several other material combinations have been explored. Combining $Mg_{1.5}Ni$ and $Mg_{3.5}Ni$ layers we hoped to make use of the small difference in enthalpy between these layers [27]. To remove possible kinetic barriers, we applied a thin layer of Ti between these layers. Alternatively, we substituted $V_{0.89}Cr_{0.19}$ as the reservoir layer as its isotherms do not exhibit a plateau in the applied temperature range. In another experiment we used Mg_5Ni as the switchable layer, since this material switches faster and has a better cycling stability as compared to Mg_2Ni. Finally, a combination of Y and Mg-doped Y was tried, since it has been argued [28] that the enthalpy of formation can be changed slightly by the addition of Mg. Therefore, this would result in a bilayer with only a small difference in the enthalpies of hydride formation, which is to be preferred as explained in the former paragraph.

Unfortunately, none of these material combinations changed their optical properties upon a temperature increase.

4.4 Discussion

The performance of various thermochromic devices have been disappointing so far. Apart from the exceptions described in the previous paragraph, no real thermochromic effects have been observed. Before going into the different possible causes for the absence of a thermochromic effect, we first analyze the conditions for the thermochromic effect in more detail. In paragraph 4.2 the demands for a large change in hydrogen concentration upon changing temperature have been analyzed. However, to actually obtain such a redistribution of hydrogen we additionally need a large driving force and a small activation barrier.

Let us go back to the chemical potentials as a function of temperature. In Figure 4.18 we replotted Figure 4.7, but now indicated the initial driving force for the hydrogen redistribution in the all-solid-state device. The driving force is large if one of the materials has a low hydrogen concentration ($x < 0.5$), while the other has a large hydrogen concentration ($x > 0.5$), since then the direction of change in chemical potential becomes opposite upon a temperature change. At low concentrations the materials get undersaturated while at high concentrations they get oversaturated upon a temperature increase. In the situation sketched in Figure 4.18, the chemical potential $\mu_{H,A}$ of material A becomes more negative, while $\mu_{H,B}$ gets less negative, resulting in a large driving force. We note, that at optimal conditions the initial driving force is in the order of a few kJ/mol H. This means that small changes in the thermodynamic properties could have a large influence on the observation of a thermochromic effect. Likewise, small activation barriers could totally block the redistribution of hydrogen.

For the working of a thermochromic device, not only the thermodynamics involved are important, but also the rate of change. The activation barrier influences directly the kinetics of the hydrogen redistribution and therefore relates to the rate of change of the optical appearance of the thermochromic device upon changing temperature. We now discuss various causes for the absence of a thermochromic effect. All are based on either a smaller change in hydrogen concentration as compared to our model, a low driving force or a high activation barrier.

4.4.1 The accuracy of the model and thermodynamic data

In paragraph 4.2 a model was presented to describe the redistribution of hydrogen upon changing temperature. Because of the difference between the predicted substantial change in hydrogen concentration and the absence of a thermochromic effect in most of the experimental cases, the question about the accuracy of the model and thermodynamic data used, arises naturally. The main simplification of the model of the all-solid-state thermochromic device is the representation of the chemical potential of hydrogen in the switchable mirror by a broad plateau. As soon as the hydrogen concentration drops below the plateau, the model overestimates the amount of transferred hydrogen. Furthermore, no hysteresis nor the rate of the hydrogen redistribution are taken into account. These are discussed in the

Absorption	Desorption	Temperature range	Reference
	-32.2	547-622	[29]
-31.0	-31.6	423-593	[30]
	-31.8	573-613	[31]
-26.6	-36.4	513-633	[32]
-30.7	-31.6	548-593	[33]
-29.6	-34.7	593	[34]
-29.5	-33.1	mean	
2.0	2.0	standard deviation	

Table 4.1: Enthalpy of hydride formation of Mg_2Ni during absorption and desorption according to various publications. The enthalpy is given in kJ/mol H and the temperature range is given in Kelvin.

next section.

The thermodynamical data used in the model turned out to be very critical. If the enthalpy of hydride formation used in our model differs slightly from the real enthalpy of our films, this may affect the amount of transferred hydrogen. A difference between the used and real enthalpy of formation is not unlikely, given the spread in the literature. For example, the literature data concerning the enthalpy of hydride formation of Mg_2Ni is presented in table 4.1. The standard deviation of the formation enthalpy measured during desorption is 2.0 kJ/mol H. Especially a difference in microstructure or stress state can cause such variances. A decrease in grain size results in a lowering of the critical temperature [35–38]; i.e. the width of the two-phase region depends on the grain size of the material. Therefore, if for example the Pd layer in our all-solid-state thermochromic device has smaller grains than the one of which the data was taken (ref [18]), the change in hydrogen solubility upon changing temperature is larger. Furthermore, a difference in molar volume of the hydride changes the ΔH [39]; i.e. an increased lattice distance results in a lowering of ΔH. Therefore, thermodynamic values obtained from bulk samples, from thin films deposited by a different deposition technique or at different deposition conditions than ours, or thermodynamic values obtained from samples of different composition, should be used with care. Moreover, even the stress induced by the other layers of the device can influence the thermodynamic properties of our switchable mirror or reservoir layer, resulting in a difference between the predicted and measured thermochromic effect. The enthalpy of formation used for our sputtered Mg-Ni film is determined electrochemically from a MBE-grown Mg-Ni film [22]. Although the data is obtained from a thin film, the deposition methods differed. Both the Pd and V-Cr data are taken from measurements performed on bulk samples.

4.4.2 Hysteresis

One of the largest problems of thermochromic devices might be the presence of a hysteresis; i.e. the difference between the absorption and desorption isotherms. The effect is usually quantified by the free energy difference: $\Delta G_{H_2}(hyst) = RT \ln\left(\frac{p_f}{p_d}\right)$ [40]. The volume increase upon hydrogen uptake causes plastic deformation of the material, thereby creating dislocations, which requires the excess energy. This increases the plateau pressure during hydrogen uptake, whereas during dehydrogenation the amount of dislocations stay unchanged and therefore a difference is observed between the absorption and desorption isotherms. The larger the volume change, the larger the hysteresis [41].

For switchable mirrors it has been observed that the hysteresis is caused by different stress states during hydrogenation and dehydrogenation [42]. These different stress states cause a difference in hydrogen concentration in one of the two phases, thereby changing the optical properties of this phase. The hysteresis is reduced by suppressing the phase transition by alloying [43] and by decreasing the grain size [44].

So far, no data of the hysteresis in our films, used for the thermochromic device, is available. If the hysteresis of Mg_2Ni would be larger than 4 kJ/mol H (≈0.04 eV), which is not unlikely (see Table 4.1), then the chemical potential μ_{H,Mg_2Ni} of hydrogen in Mg_2Ni in Figure 4.15 would drop to μ_{Mg_2Ni}=-2.52 eV and no thermochromic effect would be observable (see Figure 4.19). Note, that hysteresis is normally observed in the two-phase region and that it is therefore not expected to influence the behavior of Pd in this case.

4.4.3 Cycling stability

Cycling stability is essential for the proper functioning of all devices. Upon repeated hydrogen loading it becomes more and more difficult to pump hydrogen in or out of a layer. The kinetics in a gas cell device depends mainly on the quality of the catalytic cap layer [45], for which we use an 10-nm thin Pd layer. Surface contamination results in a significant deterioration of the kinetics. Furthermore, we have to prevent intermixing of the various layers which constitute the device. This creates a barrier, which reduces the kinetics. Several buffer layers have been used to prevent this problem [46]. A buffer layer can also help to prevent degradation by oxidation. Although the Pd-cap layer slows down the oxidation of the underlying layers, it does not completely prevent it. Moreover, the relaxation of stress by plastic deformation caused by changing hydrogen concentration reduces the cycling stability. Furthermore, the optical appearance between the metal and hydride state can change due to an increase in the hysteresis. An additional effect reducing the cycling stability of an all-solid-state thermochromic device can originate from hydrogen leakage through the cap layer. After a week an all-solid-state device, covered by 300 nm Cu and with the Mg-Ni film in the reflecting state turned out to have a non-expanded Pd lattice spacing observed by XRD-measurements. From this we concluded that no hydrogen

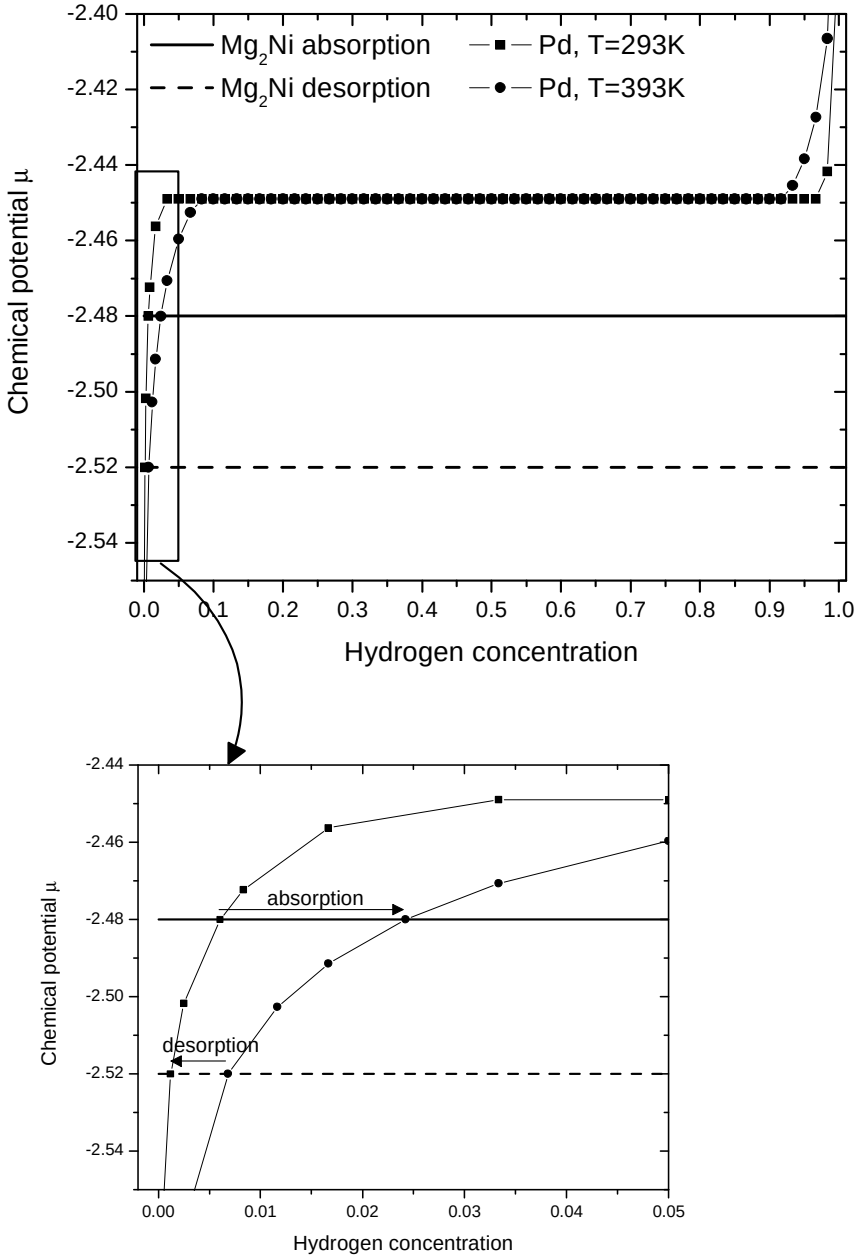

Figure 4.19: The influence of hysteresis of the chemical potential of hydrogen in the Mg-Ni film on the hydrogen redistribution. Figure 4.15 is replotted with a desorption chemical potential added assuming a hysteresis of 4 kJ/mol H. The change in hydrogen concentration is $\Delta x_{Pd} = \Delta x_{Mg-Ni}$=0.003 instead of $\Delta x_{Pd} = \Delta x_{Mg-Ni}$=0.011 in the hysteresis-free case as can be seen from the enlargement.

Layer	Material	Temperature range	D	Reference
Cap layer	Pd	273	1×10^{-7}	[47]
Switchable mirror	$Mg_2NiH_{0.3}$	423	3×10^{-8}	[48]
Switchable mirror	$V_{0.9}Cr_{0.1}$	293	1.5×10^{-5}	[49]

Table 4.2: Diffusion coefficient D in cm^2/s of H in several materials which could be used as catalytic cap layer, hydrogen reservoir layer or as a switchable mirror. They are all large enough, so that the diffusion is not the rate determining step for hydrogenation and dehydrogenation of thermochromic devices. The temperature range is given in Kelvin.

was left in the Pd and the Mg-Ni layer which points into the direction of hydrogen leaking through the Cu layer.

4.4.4 Kinetics

So far, we have discussed the thermodynamics of a thermochromic device. The model describes the change in hydrogen concentration as a function of temperature, but does not tell us anything about the rate at which the equilibrium state is reached, i.e. we have not dealt with the kinetics yet. For the use of a thermochromic device for solar collectors or smart windows the reaction time of such a device should be of the order of minutes.

The transfer of hydrogen to and from the switchable mirror involves several steps. To improve the kinetics of hydrogenation and dehydrogenation it is important to identify the rate-determining step. Since the steps involved in the hydrogenation and dehydrogenation of the switchable mirror are different for the gas cell and all-solid-state device, they are dealt with separately, starting with the latter one.

The redistribution of hydrogen in the all-solid state device takes place by (1) hydrogen diffusion within the reservoir layer towards the interface, (2) transfer of H across the interface and (3) diffusion of the hydrogen in the switchable mirror. Finally, nucleation and growth of the hydride occurs if the concentration of hydrogen is such, that the material is in the two-phase region. Since hydrogen diffusion in metals is fast, this is not considered to be the rate-determining step. The diffusion coefficient is approximately $10^{-8} cm^2/s$, which implies that even films of 1500 nm thick should be hydrogenated within 2 seconds. Table 4.2 gives the diffusion coefficients of several materials which can be used for hydrogen reservoir or as switchable mirror. Since the switching time of the thermochromic device is larger than a few seconds, crossing the interface or the nucleation and growth of the hydride phase apparently determines the rate. The activation barrier posed by the nucleation of either the metal or the hydride can be circumvented by choosing an initial hydrogen concentration such that the material is in the two phase region, where the metallic and hydride phases coexist. Then, the transfer of hydrogen at the interface between the reservoir layer and the switchable layer or the growth of the phase, i.e. the movement of the interface between the metal and hydride phase, determines the rate of

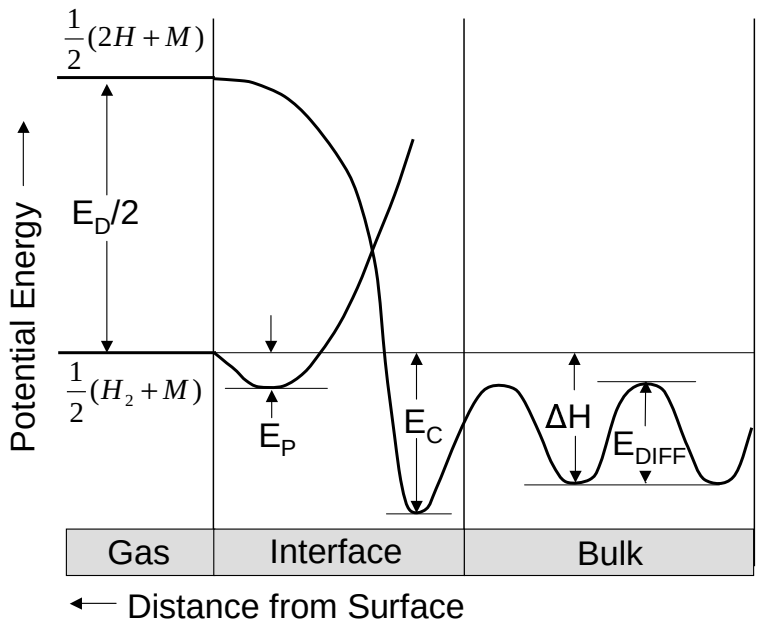

Figure 4.20: Potential energy of a hydrogen at the surface of a metal [41]. E_D, E_P and E_C represent the binding energy, physisorption and chemisorption, respectively. The hydrogenation process at the surface consists of the following steps: physisorption at the surface, dissociation of the hydrogen molecule into atoms, chemisorption, surface penetration and diffusion.

change of hydrogen concentration.

In the gas cell device, the processes at the surface between the gas and the solid are important. As described in reference [50] and shown in Figure 4.20, the hydrogenation process at the surface consists of several steps, namely physisorption at the surface, dissociation of the hydrogen molecule into atoms, chemisorption, surface penetration and diffusion. In order to have a catalytic effect the cap layer should react faster with the hydrogen than the switchable mirror and should form a less stable hydrogenated state, otherwise the hydrogen will not form a compound with the already bounded hydrogen.

The catalytic properties depend considerably on contaminations present at the surface. For Pd it has been observed that the presence of oxygen can improve the desorption rate [23]. We indeed found that for our thermochromic gas cell device the presence of oxygen is crucial.

4.5 Conclusions

We presented two different ways to realize a thermochromic device. Firstly, an open gas cell device consisting of a single switchable mirror layer in contact with a hydrogen atmosphere. Secondly, an all-solid-state device consisting of a metal-hydride bilayer, sealed by a cap layer impermeable to hydrogen. We derived for both cases expressions for the hydrogen concentration dependence on temperature using thermodynamics. A change in hydrogen concentration in turn induces a large change in the optical properties of the switchable mirrors.

The thermodynamic properties needed for a thermochromic device with a high optical contrast between low and high working temperatures turned out to be as follows. For a gas cell device we derived that the optically active layer needs to have a broad plateau pressure and that the hydrogen pressure should be just above the plateau. From a practical point of view, this amounts to a material with a low critical temperature T_c and a plateau pressure between 10^{-4} and 1 bar around room temperature, i.e. with an enthalpy of hydride formation ΔH between -30 kJ/mol H and -19 kJ/mol H.

For the all-solid-state device the isotherm of one of the layers should have a plateau. The hydrogen pressure applied to the device before it is sealed with the hydrogen impermeable cap layer should be the same as this plateau pressure. The other component of the bilayer should have a very similar ΔH and should be just above the critical temperature T_c. If hydrogen *desorption* from the switchable mirror layer upon temperature increase is desired, the reservoir metal-hydride layer should have a less negative formation enthalpy ΔH than the switchable mirror layer. In that case, the increase of the chemical potential of hydrogen with increasing temperature is smaller for the reservoir layer than for the switchable mirror layer resulting in hydrogen migration from the switchable mirror to the reservoir layer.

The calculated change in optical properties for a thermochromic gas cell device as well as a thermochromic all-solid-state system were compared with experimental results. Especially the results of the all-solid-state device have been disappointing so far. To develop a properly functioning device we conclude that it is important to minimize all possible activation barriers. Furthermore it seems necessary to develop a device in which none of the layers experiences hysteresis.

Bibliography

[1] P. Jin, K. Yoshimura, and S. Tanemura. Dependence of microstructure and thermochromism on substrate temperature for sputtered-deposited VO_2 epitaxial films. *J. Vac. Sci. Techn., A*, 15(3):1113–1117, 1997.

[2] J.N. Huiberts, R. Griessen, J.H. Rector, R.J. Wijngaarden, J.P. Dekker, D.G. de Groot, and N.J. Koeman. Yttrium and lanthanum hydride films with switchable optical properties. *Nature*, 380:231–234, 1996.

[3] P. van der Sluis, M. Ouwerkerk, and P.A. Duine. Optical switches based on magnesium lanthanide alloy hydrides. *Appl. Phys. Lett.*, 70(25):3356–3358, 1997.

[4] T.J. Richardson, J.L. Slack, R.D. Armitage, R. Kostecki, B. Farangis, and M.D. Rubin. Switchable mirrors based on nickel-magnesium films. *Appl. Phys. Lett.*, 78(20):3047–3049, 2001.

[5] K. Yoshimura, Y. Yamada, and M. Okada. Optical switching of Mg-rich Mg-Ni alloy thin films. *Appl. Phys. Lett.*, 81(25):4709–4711, December 2002.

[6] J. Isidorsson, I.A.M.E. Giebels, R. Griessen, and M. Di Vece. Tunable reflectance Mg-Ni-H films. *Appl. Phys. Lett.*, 80(13):2305–2307, April 2002.

[7] I.A.M.E. Giebels, S.J. van der Molen, R. Griessen, and M. Di Vece. Thermochromic effect in $YH_{3-\delta}$ and $Mg_{0.1}Y_{0.9}H_{2.9-\delta}$. *Appl. Phys. Lett.*, 80(8):1343–1345, 2002.

[8] Ronald Griessen and Andreas Züttel. *Science and Technology of Hydrogen in metals.* Amsterdam, 2005.

[9] L.D. Landau and E.M. Lifshitz. *Statistical Physics.* Pergamon Press, Oxford, 2nd revised and enlarged edition edition, 1969.

[10] Yuh Fukai. *The metal-hydrogen system.* Springer-Verlag, New York, 1993.

[11] G. Alefeld. Wasserstoff in Metallen als Beispiel für ein Gittergas mit Phasenumwandlungen. *Phys. Stat. Sol.*, 32:67–80, 1969.

[12] C.N. Yang and T.D. Lee. Statistical theory of equations of state and phase transitions. i. theory of condensation. *Phys. Rev.*, 87(3):410–419, 1952.

[13] T.D. Lee and C.N. Yang. Statistical theory of equations of state and phase transitions. ii. lattice gas and ising model. *Phys. Rev.*, 87(3):410–419, 1952.

[14] F.D. Manchester. *Phase Diagrams of Binary Hydrogen Alloys.* Materials Park : ASM International, 2000.

[15] W.L. Bragg and E.J. Williams. The effect of thermal agitation on atomic arrangement in alloys. *Proc. Roy. Soc. London A*, 145:699–730, 1934.

[16] R. Feenstra, R. Griessen, and D.G. de Groot. Hydrogen induced lattice expansion and effective H-H interaction in single phase PdH_c. *J. Phys. F: Met. Phys.*, 16:1933–1952, 1986.

[17] R.C. Brouwer and R. Griessen. Heat of solution and site energies of hydrogen in disordered transition-metal alloys. *Phys. Rev. B*, 40:1481–1494, July 1989.

[18] John R. Lacher. A theoretical formula for the solubility of hydrogen in palladium. *Proc. R. Soc. London A*, 161:525–545, 1937.

[19] J.R. Lacher. The statistics of the hydrogen-palladium system. *Cambridge Phil. Soc. Proc.*, 33:518–523, 1937.

[20] I.I. Diakonov, K.V. Ragnarsdottir, and B.R. Tagirov. Standard thermodynamic properties and heat capacity equations of rare earth hydroxides: Ii. Ce(iii)-, Pr-, Sm-, Eu(iii)-, Gd-, Tb-, Dy-, Ho-, Er-, Tm-, Yb-, and Y-hydroxides. comparison of thermochemical and solubility data. *Chem. Geol.*, 151:327–347, 1998.

[21] W. Lohstroh, R.J. Westerwaal, B. Noheda, S. Enache, I.A.M.E. Giebels, B. Dam, and R. Griessen. Self-organized layered hydrogenation in black Mg_2NiH_x switchable mirrors. *Phys. Rev. Lett.*, 93(19):197404, November 2004.

[22] W. Lohstroh, R.J. Westerwaal, J.L.M. van Mechelen, C. Chacon, E. Johansson, B. Dam, and R. Griessen. The structural and optical properties of $Mg_{2\pm y}NiH_x$ switchable mirrors upon hydrogen loading. *Phys. Rev. B*, 70:165411, 2004.

[23] L. Grasjo, G. Hultquist, K.L. Tan, and M. Seo. Surface reactions on palladium hydride in vacuum, air and water studied in situ with mass spectrometry. *Appl. Surf. Sci.*, 89:21–34, 1995.

[24] H.M. Dannetun, D. Söderberg, I. Lundström, and L.-G. Petersson. The H_2-O_2 reaction on palladium studied over a large pressure range: independence of the microscopic sticking coefficients on surface condition. *Surf. Sci.*, 152/153:559–568, 1985.

[25] L.-G. Petersson, H.M. Dannetun, and I. Lundström and. Water production on palladium in hydrogen-oxygen atmospheres. *Surf. Sci.*, 163:273–284, 1985.

[26] H. Frieske and E. Wicke. Magnetic susceptibility and equilibrium diagram of PdH_n. *Ber. Bunsen-Ges. Phys. Chem.*, 77:48, 1973.

[27] R. Gremaud, A. Borgschulte, W. lohstroh, H. Schreuders, A. Züttel, B. Dam, and R. Griessen. $Mg_yNi_{1-y}H_x$ thermodynamics and kinetics by optical hydrogenography. *to be submitted.*

[28] D.G. Nagengast, A.T.M. van Gogh, E.S. Kooij, B. Dam, and R. Griessen. Contrast enhancement of rare-earth switchable mirrors through microscopic shutter effect. *Appl. Phys. Lett.*, 75(14):2050–2052, 1999.

[29] J.J. Reilly and jr. R.H. Wiswall. The reaction of hydrogen with alloys of magnesium and nickel and the formation of Mg_2NiH_4. *Inorg. Chem.*, 7:2254–2256, 1968.

[30] K. Nomura, E. Akiba, and S. Ono. Kinetics of the reaction between Mg_2Ni and hydrogen. *Int. J. Hydrogen Energy*, 6(3):295–303, 1981.

[31] E. Akiba, K. Nomura, S. Ono, and Y. Mizuno. Pressure-composition isotherms of Mg-Ni-H_2 alloys. *J. Less-common Met.*, 83(3):L43–L46, 1982.

[32] S. Orimo, K. Ikeda, H. Fujii, Y. Fujikawa, Y. Kitano, and K. Yamamoto. Structural and hydriding properties of the Mg-Ni-H system with nano- and/or amorphous structures. *Acta Mater.*, 45(6):2271–2278, 1997.

[33] M.Y. Song and H.R. Park. Pressure-composition isotherms in the Mg_2Ni-H_2 system. *J. Alloys Compd.*, 270(3):164–167, 1998.

[34] G. Liang, S. Boily, J. Huot, A. Van Neste, and R. Schulz. Mechanical alloying and hydrogen absorption properties of the Mg-Ni system. *J. Alloys Compd.*, 267(3):302–306, 1998.

[35] R. Kirchheim, T. Mutschele, W. Kieninger, H. Gleiter, R. Birringer, and T.D. Koble. Hydrogen in amorphous and nanocrystalline metals. *Mater. Sci. Eng.*, 99:457–462, 1988.

[36] J.A. Eastman, L.J. Thompson, and B.J. Kestel. Narrowing of the palladium-hydrogen miscibility gap in nanocrystalline palladium. *Phys. Rev. B*, 48(1):84–92, 1993.

[37] R. Kirchheim, I. Kownacka, and S.M. Filipek. Hydrogen segregation at grain boundaries in nanocrystalline nickel. *Scr. Metall. Mater.*, 28:1229–1234, 1993.

[38] L. Zaluski, A. Zaluska, and J.O. Ström-Olsen. Nanocrystalline metal hydrides. *J. Alloys Compd.*, 70-79:2417–2431, 1997.

[39] Ronald Griessen and Thomas Riesterer. *Hydrogen in Intermetallic Compounds I*, volume 63 of *Topics in Applied Physics*, chapter 6. Springer-Verlag, Berlin, 1988.

[40] Louis Schlapbach. *Topics in Physics, Hydrogen in Intermetallic Compounds I, Electronic, Thermodynamic, and Crystallographic Properties, Preparation*, volume 63, chapter 3. Springer-Verlag Berlin Heidelberg, 1988.

[41] K. Tanaka and O. Yoshinari. *Encyclopedia of Materials: Science and Technology*, chapter Hydrogen-Metal Systems: Basic Properties (1), pages 3905–3913. Elsevier, 2001.

[42] A. Remhof, J.W.J. Kerssemakers, S.J. van der Molen, R. Griessen, and E.S. Kooij. Hysteresis in YH_x films observed with *in situ* measurements. *Phys. Rev. B*, 65:054110, 2002.

[43] A.T.M. van Gogh, D.G. Nagengast, E.S. Kooij, N.J. Koeman, and R. Griessen. Quenching of giant hysteresis effects in $La_{1-z}Y_zH_x$ switchable mirrors. *Phys. Rev. Lett.*, 85(10):2156–2159, 2000.

[44] A.C. Lokhorst, M.C.R. Heijna, J.H. Rector, I.A.M.E. Giebels, N.J. Koeman, and B. Dam. The properties of pulsed laser deposited YH_2 films for switchable devices. *J. Alloys Compd.*, 356-357:536–540, 2003.

[45] A. Borgschulte, R.J. Westerwaal, J.H. Rector, H. Schreuders, B. Dam, and R. Griessen. Engineering catalysts promoting hydrogen uptake. *submitted to Phys. Rev. B.*

[46] Anna-Maria Janner, Paul van der Sluis, and Virginie Mercier. Cycling durability of switchable mirrors. *Electrochim. Acta*, 46:2173–2178, 2001.

[47] H. Hasegawa and K. Nakajima. Effect of hydrogen on the mechanical properties of Pd. *J. Phys. F: Metal Phys.*, 9(6):1035–1046, 1979.

[48] J. Topler, H. Buchner, H. Saufferer, K. Knorr, and W. Prandl. Measurements of the diffusion of hydrogen atoms in magnesium and Mg_2Ni by neutron scattering. *J. Less-common Met.*, 88:397–404, 1982.

[49] David J. Pine and R.M. Cotts. Diffusion and electrotransport of hydrogen and deuterium in vanadium-titanium and vanadium-chromium alloys. *Phys. Rev. B*, 28(2):641–647, 1983.

[50] L. Schlapbach. *Hydrogen in intermetallic compounds II.* Springer Verlag, Berlin, 1992.

Summary

Switchable mirrors

This thesis deals with several types of switchable mirrors. Let me first explain the term switchable mirror. A mirror consists of a metal layer deposited onto a glass substrate. The nicely flat surface of the metal at the glass side reflects the incoming light, which allows to see one's own reflection. Switchable mirrors consist of a special type of metal, which has the ability to change from reflecting to transparent by absorbing hydrogen (H_2). The "switchable mirror layer" does not reflect light anymore after hydrogen absorption; the light passes through the layer and one sees objects behind the switchable mirror, i.e. it has become a window. By removing the hydrogen gas, the switchable mirror becomes reflecting again. Thus, a switchable mirror is a mirror which can transform into a window and back to a mirror by adding or removing hydrogen gas.

The switchable mirror effect was discovered by Huiberts *et al.* in 1995 at the Vrije Universiteit in Amsterdam. They showed that the materials yttrium (Y) and lanthanum (La) changed from reflecting to transparent upon hydrogen absorption. To protect these layers from oxidation and to facilitate hydrogen uptake, the layers were covered by a thin layer of palladium (Pd). Later, at Philips, a new type of switchable mirror was discovered: when adding magnesium (Mg) to yttrium (Y), lanthanum (La) or rare-earth (RE) materials, the films became color neutral. Without magnesium, e.g. yttrium is yellowish in transmission.

These Mg-rare-earth thin films exhibit a third optical state in between the reflecting and transparent state: the absorbing state. In this state the incoming light is absorbed and therefore the switchable mirror appears black. When shining light on a black surface, this surface becomes hot. Therefore this type of switchable mirror can be used to control the temperature of an object which has been covered by a switchable mirror coating. When the switchable mirror is in its black state, the object is heated by absorbed sunlight. By switching it to the reflecting state, heating stops. Therefore, these coatings can be used for temperature control of for example solar collectors.

Introduction

This thesis investigates the applicability of several types of switchable mirrors to be used as the active layer in thermochromic devices. Metal-hydride switchable mirrors are able to change their optical appearance reversibly and thus belong to the class of chromogenic materials. The change in transmission, reflection and absorption can be induced in many different ways, i.e. due to an applied gas pressure, voltage, chemical species, pressure, light or temperature. This opens up the possibility to implement these switchable thin films in devices usable for a wide range of applications, including smart windows and variable emittance surfaces for temperature stabilization. Thermochromic devices are the most simple ones of all chromogenic devices, consisting of the least amount of layers. Therefore, in this Ph.D project we have chosen for implementing switchable mirrors in these devices. The emphasis is on i) a thermochromic gas cell device in which the device consists of a switchable mirror layer on a transparent substrate inside a gas environment and on ii) a completely novel all-solid-state thermochromic device, which consists of a switchable mirror layer and a hydrogen storage layer deposited on a transparent substrate and covered by a hydrogen impermeable layer. We discuss both the optical as well as the structural properties of various types of switchable mirrors in relation to their implementation.

RE-hydrides prepared by Pulsed Laser Deposition

Rare-earth-metal hydrides are the archetypal switchable mirrors. They exhibit a high optical contrast. We use pulsed laser deposition (PLD) to deposit RE-switchable mirror layers as this deposition technique is a versatile method. This is for example demonstrated by the fact that, depending on the substrate temperature, the crystallinity of the film ranges from epitaxial ($T_{substrate}$ = 500°C) to nanocrystalline ($T_{substrate}$=room temperature). The optical change is between the reflecting dihydride and the transparent trihydride phase. In depositing the dihydride in situ, we avoid the large expansion which accompanies the phase transition from metallic to the dihydride state, thereby increasing the cycling stability when used in a device.

PLD facilitates the in-situ formation of yttrium dihydride (YH_2) films at low hydrogen background pressures. Without adding any reactive hydrogen, the dihydride is formed in situ due to hydrogen preferentially evolving from the metallic target which contains a small amount of hydrogen. Upon pulsed laser irradiation, the target acts as a pulsed source of both RE and hydrogen. The increased hydrogen content of the film as compared to the target is due to diffusion assisted preferential ablation of hydrogen. Due to this incongruent deposition process the hydrogen load on the deposition system is minimized, which is important in view of the fabrication of hydride/oxide stacks for all-solid-state switchable mirror devices.

The in-situ grown nanocrystalline dihydride films remain in the fcc-phase (face-centered cubic) upon hydrogen loading. As a result, we do not observe a hysteresis

in these films. Moreover, these films have a smooth surface morphology. Comparing the switching behavior to that of MBE-grown (molecular beam epitaxy), ex-situ hydrogenated RE films, PLD-grown RE films show a reduced optical and electrical contrast in switching, which is due to the additional formation of $RE(OH)_3$. Using a highly purified RE target the amount of oxygen is reduced, which improves the switching contrast. Surface flatness, the absence of hysteresis and a steep optical transition are important advantages if these materials are to be incorporated in all-solid-state chromogenic devices.

Mg-TM-hydrides

Sputtered third generation Mg-TM-H (transition metal TM=Co, Fe) films are investigated both optically and structurally to test their suitability for incorporation in a thermochromic device. The advantage of these switchable mirrors is that they are color neutral, which is essential for many applications. Just as important is the fact that they are more resistant against oxidation than metal hydrides containing the highly reactive rare-earth hydrides and are therefore considered to have an improved cycling stability. Mg-TM-H with TM=Ni films are known to exhibit a third, absorbing state at intermediate hydrogen concentration, which enables switching between reflection and absorption. That creates the opportunity for temperature control. In this thesis we investigated other Mg-TM-H (TM=Co, Fe) at different Mg-TM ratios in the reflecting and transparent state as well as at intermediate hydrogen concentrations.

We find that the reflection in the as-prepared state increases with increasing Mg-content, whereas the reflection in the fully hydrogenated state decreases. Therefore, the contrast between the metallic and the hydride state is largest for the case with the highest Mg-content. Moreover, the transmission increases and the transmission edge shifts to higher energies with increasing Mg-content. Comparing the transition metals we find in the TM=Fe case the highest reflection in the as-prepared state, while TM=Ni has the lowest.

Besides the metal and the hydride state, we investigate the intermediate optical properties during the hydrogen loading. The absorbing nature of Mg_yNiH_x is essentially an interference effect due to a self-organized double layering. The Mg_yNi-hydride layer nucleates at the substrate interface and grows on hydrogenation at the expense of the upper metallic Mg_yNi layer. To better understand our experimental findings of the Mg_yTMH_x films (TM=Co, Fe) we model different hydrogenation scenarios. The scenarios consist of i) homogeneous nucleation throughout the film ii) nucleation at the substrate-film interface resulting in the formation of a double layer system iii) a mixture of both homogeneously dispersed hydride with a transparent layer at the substrate-film interface.

We observe that in contrast to TM=Ni, which from the first hydrogen loading cycle shows a clear double layer formation upon hydrogen uptake, the hydrogenation behavior of TM=Co, Fe depends on the loading cycle. In subsequent cycles

we observe that the hydrogenation behavior evolves from a mainly homogeneous nucleation throughout the film to a more double-layer like behavior. This change in loading behavior is more pronounced for TM=Fe than for TM=Co and increases with Mg-content.

The influence of the Mg dispersion can be held responsible for the differences in the observed optical behavior. We argue that Mg-clusters form heterogeneous incoherent grain boundaries which act as nucleation sites for hydride formation, thereby competing with the substrate-film interface and promoting homogeneously dispersed nucleation at the expense of a double layer formation. Both x-ray diffraction measurements and SEM observations (scanning electron microscopy) confirm the relation between the Mg grain size and the homogeneous nucleation behavior. The difference between the various Mg-TM-systems in the amount of Mg-clusters can be understood when looking at the binary phase diagrams of the parent alloys. The existence of binary compounds, especially when having the same composition as the hydride, is thought to increase the mixing of the Mg and the TM and thereby reduce the size of the Mg-clusters. Hydrogenation itself is suggested to reduce the Mg grain size and improve the mixing of Mg and the transition metal.

Finally, the question remains which of the discussed systems is best suited for a switchable device. Although the largest contrast in optical properties between the metal and hydride state is observed in Mg_yFe with $y = 6$, this system changes continuously during hydrogen loading cycles. After a substantial amount of cycles, the system might become stable, however, training the material is too costly. The Mg-Ni system is much more stable. Therefore, we propose Mg_yNi with $y = 6$ as the most suitable candidate for the use as a switchable mirror in an all-solid-state device for the following three reasons: i) Mg_yNi with $y = 6$ is known to have a large contrast in reflection between the metallic and hydride state ii) it has a large and color neutral transmission spectrum and iii) it has no change in hydrogenation behavior on subsequent hydrogen loading cycles.

Thermochromic devices

In this thesis we present two different ways to realize a thermochromic device. Firstly, an open gas cell device consisting of a single switchable mirror layer in contact with a hydrogen atmosphere. Secondly, a novel all-solid-state device consisting of a metal-hydride bilayer, sealed by a cap layer impermeable to hydrogen. We derive for both cases expressions for the hydrogen concentration dependence on temperature using thermodynamics.

The thermodynamic properties needed for a thermochromic device with a high optical contrast between low and high working temperatures turn out to be as follows. For a gas cell device we derive that the optically active layer needs to have a broad plateau in the pressure-composition isotherm and that the applied hydrogen pressure should be just above the plateau. From a practical point of view, this amounts to a material with a low critical temperature T_c and a plateau pressure

between 10^{-4} and 1 bar around room temperature, i.e. with an enthalpy of hydride formation ΔH between -30 kJ/mol H and -19 kJ/mol H.

For the all-solid-state device the isotherm of one of the layers should have a plateau. The hydrogen pressure applied to the device before it is sealed with the hydrogen impermeable cap layer should be the same as this plateau pressure. The other component of the bilayer should have a very similar ΔH and should be just above the critical temperature T_c. If hydrogen *desorption* from the switchable mirror layer upon temperature increase is desired, the reservoir metal-hydride layer should have a less negative formation enthalpy ΔH than the switchable mirror layer. In that case, the increase of the chemical potential of hydrogen with increasing temperature is smaller for the reservoir layer than for the switchable mirror layer resulting in hydrogen migration from the switchable mirror to the reservoir layer.

The calculated change in optical properties for a thermochromic gas cell device as well as a thermochromic all-solid-state system are compared with experimental results. Especially the results of the all-solid-state device have been disappointing so far. To develop a properly functioning device we conclude that it is important to minimize all possible activation barriers. Furthermore it seems necessary to develop a device in which none of the layers experiences hysteresis.

Samenvatting

Schakelbare spiegels

In dit proefschrift worden verschillende types schakelbare spiegels besproken. Ik zal eerst de term schakelbare spiegel uitleggen. Een spiegel bestaat uit een dunne metaallaag op een glasplaat. Het mooie gladde oppervlak van het metaal aan de glaskant weerspiegelt het invallende licht waardoor je je eigen weerspiegeling ziet. Schakelbare spiegels bevatten een speciaal soort metaallaag, die kan veranderen van weerspiegeld naar doorzichtig wanneer het waterstofgas (H_2) opneemt. De "schakelbare spiegellaag" weerspiegelt niet meer na het opnemen van waterstof; het licht valt er doorheen en je kan nu de voorwerpen achter de schakelbare spiegel waarnemen, oftewel het is een ruit geworden. Door het waterstof te verwijderen wordt de schakelbare spiegel weer spiegelend. Kortom, een schakelbare spiegel is een spiegel die in een ruit kan veranderen en weer terug naar een spiegel door waterstof toe te voegen of te verwijderen.

Het schakelbare spiegeleffect werd in 1995 ontdekt door Huiberts *e.a.* van de Vrije Universiteit in Amsterdam. Zij toonden aan dat de materialen yttrium (Y) en lanthaan (La) van weerspiegelend in doorzichtig veranderen na opnamen van waterstof. De metaallagen werden bedekt door een dun laagje palladium (Pd) om ze te beschermen tegen oxidatie en om de opname van waterstof te vergemakkelijken. Later werd bij Philips een nieuw type schakelbare spiegel ontdekt: wanneer er magnesium (Mg) aan yttrium (Y), lanthaan (La) of zeldzame aarden wordt toegevoegd, worden de metaallagen kleurloos. Zonder magnesium is bijvoorbeeld yttrium met waterstof geel-doorzichtig.

Deze dunne magnesium-zeldzame-aardlagen hebben nog een derde optische toestand tussen de weerspiegelende en de doorzichtige toestand: een lichtabsorberende toestand. In deze toestand wordt het inkomende licht geabsorbeerd en daarom ziet de schakelbare spiegel er dan zwart uit. Wanneer licht op een zwart oppervlak schijnt, wordt dit oppervlak warm. Daarom is dit type schakelbare spiegel geschikt om de temperatuur van een voorwerp te regelen waarop een laag van dit materiaal is aangebracht. Wanneer de schakelbare spiegel in de zwarte toestand is, wordt het voorwerp verwarmd door het geabsorbeerde zonlicht. Door het te schakelen naar de weerspiegelende toestand stopt dit verwarmen. Daarom kunnen deze lagen gebruikt worden voor de temperatuurregeling voor bijvoorbeeld zonnecollectoren.

Introductie

In dit proefschrift wordt de toepasbaarheid van verschillende types schakelbare spiegels onderzocht, die toegepast kunnen worden als actieve laag in thermochrome systemen. Metaal-hydride schakelbare spiegels zijn in staat om hun optische toestand reversibel te veranderen en behoren daarom tot de groep van chromogene materialen. De verandering van doorzichtig, weerspiegelend en absorberend kan op verschillende manieren bewerkstelligd worden, te weten door een gasdruk, elektrische spanning, chemicaliën, druk, licht of temperatuur. Dit maakt de weg vrij naar het implementeren van deze lagen in een breed scala aan toepassingen, waaronder "smart windows" (licht- en warmteregulerende raamsystemen) en variabele warmteafgevende oppervlakken voor temperatuurstabilisatie. Thermochrome systemen zijn de meest eenvoudige van alle chromogene systemen vanwege het geringe aantal lagen waaruit ze zijn opgebouwd. Daarom hebben we voor dit promotieonderzoek gekozen voor het implementeren van schakelbare spiegels in dit type systeem. De nadruk ligt op i) een thermochroom gassysteem waarin het systeem bestaat uit een schakelbare spiegellaag in een gasomgeving en ii) een compleet nieuw, volledig op vaste stoffen gebaseerd systeem dat bestaat uit een schakelbare spiegellaag en een waterstofopslaglaag aangebracht op een doorzichtig substraat en bedekt met een waterstofondoordringbare laag. We behandelen zowel de optische als de structurele eigenschappen van verschillende types schakelbare spiegels met betrekking tot hun toepasbaarheid.

Zeldzame-aardhydrides vervaardigd met behulp van gepulseerde laserablatie

Zeldzame-aardhydrides (waterstofverbindingen) zijn de archetypes onder de schakelbare spiegels. Ze bezitten een groot optische contrast. We gebruiken gepulseerde laserablatie om schakelbare spiegels van zeldzame aarden te vervaardigen aangezien deze preparatietechniek een veelzijdige methode is. Dit blijkt bijvoorbeeld uit het feit dat afhankelijk van de substraattemperatuur, de kristalliniteit van de dunne lagen varieert van epitaxiaal (de lagen groeien volgens de kristaloriëntatie van het onderliggende substraat) ($T_{substraat} = 500°C$) tot nanokristallijn ($T_{substraat}$ =kamertemperatuur). De optische verandering vindt plaats tussen de spiegelende dihydride- en de transparante trihydridetoestand. Door de dihydride in situ te vervaardigen vermijden we de grote uitzetting die gepaard gaat met de fasetransformatie van de zuivere metallische toestand tot de dihydridetoestand, waardoor het systeem meer schakelcycli meegaat.

Gepulseerde laserablatie vergemakkelijkt het in-situ groeien van dunne yttriumdihydridelagen (YH_2) bij lage waterstofachtergronddrukken. Zonder de toevoeging van reactief waterstof wordt de dihydride in situ vervaardigd vanwege de aanwezigheid van waterstof dat preferentieel uit te ableren metaal komt, dat een kleine hoeveelheid waterstof bevat. Het metaal fungeert als een gepulseerde bron voor zowel zeldzame-aardmetaal als waterstof. De toegenome hoeveelheid waterstof in

vergelijking tot het te ableren metaal wordt veroorzaakt door diffusieondersteunde preferentiële ablatie van waterstof. Doordat het waterstof uit het metaal komt en er geen aparte waterstoftoevoeging aan het systeem nodig is, is de waterstofbelasting voor het preparatiesysteem minimaal, hetgeen belangrijk is voor de vervaardiging van hydride/oxidestapelingen van lagen voor de geïntegreerde schakelbare spiegelsystemen.

De in-situ gegroeide, dunne, nanokristallijne dihydridelagen blijven in de fcc-fase (kubisch vlakgecentreerd) gedurende waterstofabsorptie. Daardoor nemen we geen hysteresis waar in deze dunne lagen. Bovendien hebben deze dunne lagen een vlakke oppervlaktestructuur. Wanneer we het schakelgedrag vergelijken met dat van MBE-gegroeide (moleculaire bundelepitaxie), ex-situ waterstofbeladen, zeldzame-aardlagen, vertonen de met behulp van gepulseerde laserablatie gegroeide lagen een verminderd optisch en elektrisch contrast. Dit wordt veroorzaakt door de vorming van hydroxide. Door gebruik te maken van zeer pure zeldzame aarde als ablatiemetaal wordt de hoeveelheid zuurstof gereduceerd, wat het schakelcontrast vergroot. De vlakke oppervlaktestructuur, de afwezigheid van hysteresis en de scherpe optische overgang zijn belangrijke voordelen van deze materialen wanneer ze geïntegreerd worden in volledig uit vaste stof bestaande chromogene systemen.

Mg-TM-hydrides

Gesputterde, derde generatie lagen van magnesium-overgangsmetalen-hydriden, Mg-TM-H met (TM=Co, Fe), zijn zowel optisch als op structuur getest om hun toepasbaarheid voor implementatie in een thermochroomsysteem te bepalen. Het voordeel van deze schakelbare spiegels is dat ze kleurneutraal zijn, wat noodzakelijk is voor veel toepassingen. Even zo belangrijk is het feit dat ze beter bestand zijn tegen oxidatie dan metaalhydrides die de zeer reactieve zeldzame aarden bevatten, waardoor ze meer schakelcycli meegaan. Het is bekend dat Mg-TM-H-lagen met TM=Ni een derde, absorberende toestand vertonen bij tussenliggende waterstofconcentraties, waardoor het mogelijk wordt te schakelen tussen weerspiegelend en absorberend. Dit schept de mogelijkheid voor temperatuurcontrole. In dit proefschrift onderzoeken we andere Mg-TM-H-lagen (TM=Co, Fe) met verschillende Mg-TM verhoudingen in de weerspiegelende en doorzichtige toestand als wel bij tussenliggende waterstofconcentraties.

We zien dat de reflectie in de onbehandelde toestand toeneemt met toenemend Mg-gehalte, terwijl de reflectie in de hydridetoestand afneemt. Daardoor is het contrast tussen de metallische en hydridetoestand het grootst in het geval van de grootste Mg-concentratie. Bovendien neemt de transmissie toe en verschuift het punt waar de transmissie afvalt naar hogere energieën met toenemende Mg-concentratie. Wanneer we de overgangsmetalen onderling vergelijken, vinden we voor het overgangsmetaal ijzer (TM=Fe) de grootste reflectie in de onbehandelde toestand, terwijl nikkel (TM=Ni) de laagste reflectie heeft.

Naast de metallische en de hydridetoestand bekijken we de tussenliggende op-

tische eigenschappen gedurende waterstoftoevoer. Het absorberende vermogen van Mg_yNiH_x wordt voornamelijk veroorzaakt door een interferentie-effect wat teweeggebracht wordt door een spontaan ontstane dubbellaag. De Mg_yNi-hydride laag ontstaat op het grensvlak met het substraat en groeit tijdens de waterstoftoename ten koste van de bovenliggende metallische Mg_yNi laag. Om onze experimentele bevindingen van de Mg_yTMH_x-lagen (TM=Co, Fe) beter te kunnen begrijpen, hebben we een aantal waterstofopnamescenario's gemodelleerd. De scenario's bestaan uit i) homogene vorming van hydridekiemen door de gehele laag ii) het ontstaan van een hydridelaag op het grensvlak met het substraat, wat resulteert in de vorming van een dubbellaagsysteem iii) een mengeling van zowel homogene kiemvorming als het ontstaan van een doorzichtige laag op het grensvlak met het substraat.

We zien dat, in tegenstelling tot nikkelhoudende hydrides (TM=Ni), welke vanaf de eerste belading met waterstof duidelijk een dubbellaagsysteem laten zien, de waterstofbelading van TM=Co, Fe afhangt van het aantal doorlopen waterstofbeladingen. In opeenvolgende waterstofbeladingscycli zien we dat het schakelgedrag verandert van een voornamelijk homogene kiemvorming naar meer dubbellaagsysteemgedrag. Deze verandering in waterstofbelading is duidelijker voor TM=Fe dan voor TM=Co en neemt toe met de Mg-concentratie.

De mate waarin Mg verspreid is in het materiaal kan gezien worden als de verantwoordelijke factor voor de verschillen tussen het vertoonde optische gedrag. We beargumenteren dat clusters magnesium heterogene, incoherente korrelgrenzen vormen waar hydridekiemvorming start. Dit proces concurreert met de hydridevorming op het grensvlak met het substraat. Het resultaat is dat homogene kiemvorming bevorderd wordt ten koste van het dubbellaagsysteem. Zowel röntgendiffractie als SEM-metingen (scanning-elektronenmicroscopie) bevestigen de relatie tussen de Mg-korrelgrootte en het homogene hydridekiemvormingsgedrag. Het verschil tussen de verschillende Mg-TM-systemen in het aantal Mg-clusters kan begrepen worden op grond van de binaire fasediagrammen van de oorspronkelijke legeringen. Het bestaan van een binaire verbinding wordt verondersteld de menging van het magnesium (Mg) en het overgangsmetaal (TM) te vergroten en daardoor de Mg-clustergrootte te verkleinen. Dit gaat in het bijzonder op als het om dezelfde samenstelling gaat als bij het hydride. De waterstofopname zelf is waarschijnlijk de oorzaak van het verkleinen van de Mg-korrelgrootte en het verbeteren van de menging van het magnesium en het overgangsmetaal.

Tenslotte blijft de vraag over welke van de besproken materialen het meest geschikt is voor een schakelend systeem. Alhoewel het grootste contrast in optische eigenschappen tussen de metallische en de hydridetoestand gevonden wordt voor Mg_yFe met $y = 6$, verandert dit systeem voortdurend bij opeenvolgende waterstofbeladingen. Na een aanzienlijk aantal waterstofbeladingscycli zou het systeem stabiel kunnen worden. Het trainen van het materiaal is echter te kostbaar. Het Mg-Ni systeem is veel stabieler. Daarom raden we Mg_yNi met $y = 6$ aan als meest geschikte kandidaat voor het gebruik van schakelbare spiegels in volledig uit vaste stof bestaande systemen vanwege de volgende redenen i) Mg_yNi met $y = 6$ heeft een groot contrast in reflectie tussen de metallische en de hydridetoestand ii) het heeft

een groot en kleurneutraal transmissiespectrum en iii) de manier van waterstofbelading verandert niet in opeenvolgende beladingscycli.

Thermochrome systemen

In dit proefschrift introduceren we twee verschillende manieren om een thermochroomsysteem te realiseren. Ten eerste een gassysteem dat bestaat uit een enkele schakelbare spiegellaag dat in contact is met een waterstofomgeving. Ten tweede een nieuw, volledig op vaste stoffen gebaseerd systeem dat bestaat uit een schakelbare spiegellaag en een waterstofopslaglaag bedekt met een ondoordringbare laag voor waterstof. We leiden voor beide gevallen uitdrukkingen voor de temperatuurafhankelijkheid van de waterstofconcentratie af gebruik makend van thermodynamica.

De thermodynamische eigenschappen die nodig zijn voor een thermochroomsysteem met een groot optisch contrast tussen de lage en hoge werktemperaturen zijn als volgt. Voor een gassysteem hebben we afgeleid dat de optisch actieve laag een breed plateau nodig heeft in de druk-compositie-isotherm en dat de gebruikte waterstofdruk net boven deze plateaudruk moet liggen. Vanuit praktisch oogpunt komt dit neer op een lage kritische temperatuur T_c en een plateaudruk tussen 10^{-4} and 1 bar rond kamertemperatuur, oftewel met een hydridevormingsenthalpie ΔH tussen -30 kJ/mol H en -19 kJ/mol H.

Voor het volledig op vaste stoffen gebaseerde systeem zou de isotherm van een van de dunne lagen een plateau moeten hebben. De waterstofdruk die wordt aangelegd vlak voordat het systeem wordt afgesloten met een waterstofondoordringbare laag moet even hoog zijn als deze plateaudruk. De waterstofopslaglaag zou ongeveer dezelfde ΔH moeten hebben als de optisch actieve laag en zou net boven de kritische temperatuur T_c moeten zitten. Wanneer waterstof*desorptie* verlangd wordt van de schakelbare spiegellaag bij een temperatuurstijging, dan moet de waterstofopslaglaag een minder negatieve vormingsenthalpie ΔH hebben dan de schakelbare spiegel. In dat geval is de toename van de chemische potentiaal van het waterstof met toenemende temperatuur kleiner voor de waterstofopslaglaag dan voor de schakelbare spiegellaag wat resulteert in waterstofmigratie van de schakelbare spiegel naar de opslaglaag.

De berekende verandering in optische eigenschappen van een thermochroom gassysteem als ook van een volledig op vaste stoffen gebaseerd systeem zijn vergeleken met de experimenten. Vooral de resultaten van het laatstgenoemde systeem zijn tot nu toe teleurstellend. Om een goed functionerend systeem te ontwikkelen concluderen we dat het belangrijk is om alle mogelijke activeringsbarrières te verlagen. Bovendien lijkt het noodzakelijk om een systeem te ontwikkelen waarbij geen van de dunne lagen hysteresis vertoont.

List of publications

- A.C. Lokhorst, M.C.R. Heijna, J.H. Rector, I.A.M.E. Giebels, N.J. Koeman, B. Dam: The properties of pulsed laser deposited YH_2 films for switchable devices, Journal of Alloys and Compounds, 356-357 (2003) 536-540
- B. Dam, A.C. Lokhorst, A. Remhof, M.C.R. Heijna, J.H. Rector, D. Borsa, J.W.J. Kerssemakers: In situ preparation of YH_2 thin films by PLD for switchable devices, Journal of Alloys and Compounds, 356-357 (2003) 526-529
- A.C. Lokhorst, B. Dam, I.A.M.E. Giebels, M.S. Welling, W. Lohstroh, R. Griessen: Thermochromic metal-hydride bilayer devices, Journal of Alloys and Compounds, 404-406 (2005) 465-468
- W. Lohstroh, R.J. Westerwaal, A.C. Lokhorst, J.L.M. van Mechelen, B. Dam, R. Griessen: Double layer formation in Mg-TM switchable mirrors (TM: Ni, Co, Fe), Journal of Alloys and Compounds, 404-406 (2005) 490-493
- R.J. Westerwaal, A.C. Lokhorst, M. Slaman, W. Lohstroh, A. Borgschulte, B. Kooi, G. ten Brink, K.G. Tschersich, H.P. Fleischhauer, B. Dam, R. Griessen: Optical properties and thin film microstructure of MgH_2, Mg_2CoH_5 and Mg_2FeH_6 hydrides in-situ grown by activated reactive evaporation *in preparation*
- A.C. Lokhorst, W. Lohstroh, R.J. Westerwaal, B. Dam, R. Griessen: Hydrogenation induced changes in the nucleation of Mg-TM based complex metal hydrides, *in preparation*
- J.H. Rector, A.C. Lokhorst, B. Dam: Oxygen-free RE-hydride thin films grown by reactive pulsed laser deposition, *in preparation*

Curriculum Vitae

Annemarie van Geest-Lokhorst werd geboren op 22 februari 1976 te Amersfoort. In 1994 voltooide zij het VWO aan de 'Christelijke Scholengemeenschap Zandvliet' in Den Haag. Van 1994 tot 2000 studeerde zij Materiaalkunde aan de Technische Universiteit in Delft. In het vierde jaar kreeg zij een beurs van de universiteit om de functie te vervullen van commissaris onderwijs bij de 'Materiaalkundige studievereniging Het Gezelschap Tubalkaïn'. Haar stage verichtte zij bij de groep van prof. Steve M. Yalisove aan de University of Michigan, waar zij voor het eerst in aanraking kwam met het sputteren van dunne metaallagen. Onder begeleiding van prof.dr. B.J. Thijsse (TU Delft) en dr. F. Roozeboom (Philips) deed zij haar afstudeeronderzoek bij Philips Natuurkundig Laboratorium in Eindhoven op MOS-condensatoren in macroporeus silicium. Van 2001 tot 2006 deed zij promotieonderzoek in de groep van prof.dr. R. Griessen aan de Vrije Universiteit in Amsterdam onder begeleiding van dr. B. Dam. Gedurende haar promotieonderzoek nam zij deel aan verschillende cursussen en conferenties in binnen- en buitenland (IJsland, Mallorca, Frankrijk, Polen, VS). Daarnaast gaf ze werkcollege aan studenten van de studierichting medische natuurwetenschappen. Haar promotieonderzoek resulteerde in dit proefschrift.

Annemarie van Geest-Lokhorst was born in Amersfoort, The Netherlands, on February 22nd 1976. In 1994 she finished high school at the 'Christelijke Scholengemeenschap Zandvliet' in The Hague. From 1994 till 2000 she studied Materials Science and Engineering at the University of Technology in Delft. In her fourth year she received a scholarship for becoming a member of the board (Secretary for Educational Issues) of the student association 'Materiaalkundige studievereniging Het Gezelschap Tubalkaïn'. During her internship in the group of prof. Steve M. Yalisove at the University of Michigan she had her first experience with sputtering of thin films. Her final research project was carried out at Philips Research in Eindhoven under supervision of prof.dr. B.J. Thijsse (TU Delft) en dr. F. Roozeboom (Philips) on MOS-capacitors in macroporous silicon. From 2001 to 2006 she performed her Ph.D. research in the group of prof.dr. R. Griessen at the Vrije Universiteit in Amsterdam under supervision of dr. B. Dam. During her Ph.D she attended several courses and conferences, both in The Netherlands and abroad (Iceland, Mallorca, France, Poland, USA). Furthermore she gave tutorials to undergraduate students in medical natural science. Her Ph.D. research resulted in this thesis.

Dankwoord

Vanaf deze plek wil ik de vele mensen die bijgedragen hebben aan de totstandkoming van dit proefschrift bedanken. Ten eerste Ronald Griessen, mijn promotor, voor het geven van de mogelijkheid om in zijn groep te promoveren. Verder wil ik hem bedanken voor de betrokkenheid bij met name het laatste hoofdstuk. Natuurlijk dank ik Bernard Dam voor de begeleiding en discussies tijdens mijn promotie. Wiebke Lohstroh ben ik erkentelijk voor de motiverende begeleiding en het geven van ruimte op tijden dat ik dat nodig had.

Technische ondersteuning tijdens de vele metingen was onmisbaar. Nico Koeman bedank ik voor zijn grondige aanpak en uitleg, Kier Heeck voor zijn enthousiasme, Herman Schreuders voor de samples en zijn gezelschap 's morgens vroeg, Martin Slaman voor onze discussies en metingen en natuurlijk Jan Rector, die voor het belangrijkste deel de technische ondersteuning gaf, bedank ik voor alle hulp en zeker ook voor zijn steun in moeilijke tijden. De mensen van de mechanische en elektronische werkplaats hebben mij ook vaak en snel terzijde gestaan.

Ook veel collega's hebben in de loop van de tijd geholpen, enerzijds met uitleg en discussies, anderzijds door de sfeer te veraangenamen: Marco Welling (computerhulp en klankbord), Ingrid Giebels (optische metingen en discussies), Ruud Westerwaal (discussies en HF-etsen), Arndt Remhof (XRD-uitleg en stante pede hulp), Maurits Heijna (inwerken in PLD), Beatriz Noheda (vraagbaak), Andreas Borgschulte (levendige kamergenoot), Dana Borsa (discussies), Robin Gremaud (thermodynamische data), Marc Huisman (leuke inbreng tijdens koffiepauzes), Sonia May (vraagbaak Engelse taal), Wouter Hamer (laatste Latex loodjes), Karen Vermeulen, Stănică Enache, Christof Aegerter, Kinga Lőrincz, Diana Gheorghe, Mariella Menghini, Mathieu Pasturel, Philip Mauron, Andrea Baldi, Davide Iannuzzi, Dook van Mechelen, Sven de Man en Chase Broedersz.

Tenslotte waardeer ik alle steun van het thuisfront: mijn vader, tot twee jaar terug mijn moeder (in dankbare herinnering), mijn zus Pauline en natuurlijk mijn man Sander. Verder dank ik alle vrienden en familie voor hun interesse de afgelopen jaren.